NORTHWESTERN UNIVERSITY

Improved Transparent Conducting Oxides Through Modulation-Doped ZnO/ZnMgO Thin Films

A DISSERTATION

SUBMITTED TO THE GRADUATE SCHOOL
IN PARTIAL FULFILLMENT OF THE REQUIREMENTS

for the degree

DOCTOR OF PHILOSOPHY

Field of Materials Science and Engineering

By

David J. Cohen

EVANSTON, ILLINOIS

December 2008

ABSTRACT

Improved Transparent Conducting Oxides Through
Modulation Doped ZnO/ZnMgO Thin Films

David John Cohen

ZnO is a member of the unique class of materials known as transparent conducting oxides (TCOs). TCOs are currently used for many applications including flat panel displays, solar cells, and energy efficient windows. Of particular interest is the possibility of developing materials that have high electron mobilities, such that conductivities may be increased without loosing transparency in the visible spectrum. Modulation doping was chosen as a possible technique to achieve this outcome.

ZnMgO:Al films were grown and characterized as a potential barrier layer in a modulation doped structure. High quality films, rocking curve FWHM ~1- 2^{o}, were grown on c-plane sapphire substrates. The ability of Mg to increase the band gap of ZnO up to a value of 3.76 eV was confirmed. Aluminum was used as a donor in ZnMgO, and maximum carrier concentration levels of ~1 x 10^{20} cm^{-3} were achieved. The wide band gap semiconductor ZnMgO:Al was determined to be a suitable choice as a barrier layer in a modulation doped structure.

A one dimensional Schrodinger/Poisson simulation program was used to investigate the influence of the parameters in a modulation doped ZnO/ZnMgO:Al structure on the film properties. The optimum electrical properties were achieved when the active ZnO layer and barrier ZnMgO:Al layer were both in the range of 2-5 nm. The

optimum thickness for the ZnMgO spacer layer was calculated to be 1.5 nm. Mobilities as high as 145 cm^2/Vs were predicted for the optimum structures, compared to ~30 cm^2/Vs in monolithic ZnO films. The maximum sheet electron density that could be transferred from the doped to the undoped layers was predicted to be ~10^{13} cm^{-2}.

Multilayer structures were grown and characterized. Following the trends predicted from the multilayer simulations, a five period multilayer with ZnO and ZnMgO:Al layers of 5 nm had a mobility of ~33 cm^2/Vs and a resistivity of 1.44 x 10^{-3} Ω cm, compared to a multilayer with 20 nm thick layers which had a mobility of ~23 cm^2/Vs and a resistivity of 2.45 x 10^{-3} Ω cm. The experimental results were in reasonable agreement with the predictions of the above simulation.

Acknowledgements

I would first and foremost like to acknowledge Professor Scott Barnett. Without your guidance, thoughtful insights, and never-ending patience, this dissertation would have never been possible. You truly allowed me experience and enjoy the journey, without solely being focused on the destination. Thank you.

I would also like to thank my friends and family for making it possible for my experience in Evanston to actually be fun, and one I will always look back upon fondly.

To my parents: Your never-ending support means the world to me.

I would like to dedicate this dissertation to the memory of my grandmother, Edith Cole.

I would also like to acknowledge the contribution to my graduate school experience made by Moshe:

"Goin' where the wind don't blow so strange,
Maybe off on some high cold mountain chain.
Lost one round but the price wasn't anything,
A knife in the back and more of the same."

-Grateful Dead

"For I have always lived violently, drunk hugely, eaten too much or not at all, slept around the clock or missed two nights of sleeping, worked too hard and too long in glory, or slobbed for a time in utter laziness. I've lifted, pulled, chopped, climbed, made love with joy and taken my hangovers as a consequence, not as a punishment. I did not want to surrender fierceness for a small gain in yardage…And in my own life I am not willing to trade quality for quantity."

-John Steinbeck

"Knowledge Is Good"

-Emil Faber

Table of Contents

List of Figures

List of Tables

Chapter 1

Introduction and Background

ZnO is a member of the unique class of materials known as transparent conducting oxides (TCOs). Along with the oxides of indium, cadmium, and tin often times in various combinations, these materials posses the typically mutually exclusive properties of high transparency in the visible spectrum and moderate electrical conductivity. TCOs are currently used for many applications including flat panel displays, solar cells, energy efficient windows, and touch screens. However, improved performance is necessary to achieve higher efficiency in current products and to help develop transparent electronics. Of particular interest is the possibility of developing materials that have high electron mobilities, such that conductivities may be increased without losing transparency in the visible spectrum. In this thesis, modulation doping was chosen as a possible technique to achieve this outcome. Modulation doping is a technique used to physically separate conduction electrons from their ionized donors. This is accomplished by placing the donor atoms in a wider band gap material on either side of a smaller band gap, intrinsic material. The conduction electrons transfer across the interface in order to occupy lower energy levels in the smaller band gap material. The electrons are free to conduct with a reduced influence form the ionized donors and thus ionized impurity scattering is minimized. This technique has been successfully used in III-V semiconductor systems such as GaAs/AlGaAs, but has not been used for oxides.

Since ionized impurity scattering limits the conductivity of TCOs at high carrier concentrations, modulation doping was chosen as a potential method to improve TCO performance. A ZnO/ZnMgO system was used to grow modulation doped, TCO films. A combined experimental and modeling approach was taken.

ZnMgO:Al films were grown by reactive magnetron sputter deposition and characterized as a potential donor layer in a modulation doped structure. High quality films, rocking curve FWHM ~1- 2^{o}, were grown on c-plane sapphire substrates using reactive magnetron sputtering. The ability of Mg to increase the band gap of ZnO up to a value of 3.76 eV was confirmed, and it was discovered that Mg increases the electron effective mass of the films. Aluminum was used as a donor in ZnMgO, and maximum carrier concentration levels of ~1 x 10^{20} cm^{-3} were achieved. A reducing anneal was used to maximize the doping efficiency of the Al in the ZnMgO. The wide band gap semiconductor ZnMgO:Al was determined to be a suitable choice as a donor layer in a modulation doped structure.

A one dimensional Schrodinger/Poisson simulation program was used to investigate the influence of the parameters in a modulation doped ZnO/ZnMgO:Al structure on the film properties. The optimum electrical properties were achieved when the active ZnO layer and barrier ZnMgO:Al layer were both in the range of 2-5 nm. The optimum thickness for the ZnMgO spacer layer was calculated to be 1.5 nm. Mobilities as high as 145 cm^2/Vs were predicted for the optimum structures, compared to ~30 cm^2/Vs in monolithic ZnO films with comparable doping level. Based on the simulations a maximum sheet electron density that could be transferred from the doped to the

undoped layers was predicted to be ~10^{13} cm^{-2}. These predictions were in good agreement with recent experimental values reported for modulation doped structures.

Multilayer structures were grown and characterized using time-of-flight secondary ion mass spectrometry (ToF-SIMS), x-ray diffraction (XRD), and transmission electron microscopy (TEM). The ability to confine the Mg and Al to individual layers was confirmed. Following the trends predicted from the multilayer simulations, the best electrical properties were achieved for films with thin layers of ZnO and ZnMgO:Al. A five period multilayer with ZnO and ZnMgO:Al layers of 5 nm had a mobility of ~33 cm^2/Vs and a resistivity of 1.44 x 10^{-3} Ω cm, compared to a multilayer with 20 nm thick layers which has a mobility of ~23 cm^2/Vs and a resistivity of 2.45 x 10^{-3} Ω cm. These experimentally observed mobilities were found to be consistent with the above model; the measured mobilities were relatively low because of the high doping levels in the ZnMgO:Al layers, which effectively prevented transfer of a significant fraction of electrons into the pure ZnO layers. These results show that modulation doping can be used to achieve enhanced mobilities in oxide semiconductors such as ZnO. However, because of limitations on the density of electrons that can be transferred between layers, the method is not expected to be useful for making improved TCO's.

The following sections provide a literature background in the areas relevant to this work: Transparent Conducting Oxides, Zinc Oxide, Modulation Doping, and Transparent Electronics.

1.1. Transparent Conducting Oxides

Ever since Badeker[1] discovered that he could render a thin Cadmium film transparent while maintaining reasonable conductivity simply by oxidizing the metal to produce CdO, the field of transparent conducting oxides (TCOs) has flourished. The first widespread use was as transparent electrical heaters for aircraft windshield de-icing during World War II.[2] Since then, the applications and possibilities for TCOs has continued to increase. TCOs have attracted considerable attention in recent years; in August of 2000 the MRS Bulletin devoted an issue to the topic.[3-9] The traditional TCOs are the oxides of indium, tin, cadmium, and zinc, as well as multi-cation combinations of these. However, new materials are being developed continually that meet the qualifications as a TCO. The National Renewable Energy Laboratory has devoted resources to studying this class of materials.[3,9] Also, the Materials Research Society has also established an international workshop on zinc oxide, one of the materials that possesses transparency and conductivity simultaneously.

The ability of TCOs to transmit electromagnetic radiation in the visible spectrum, while at the same time maintaining the ability to conduct electrons makes them attractive for a variety of applications. Among the possible applications are front contacts for flat panel displays,[3] solar cells,[10,11] touch screens,[8] and low-emissivity windows.[8] Owing to their wide band gap, TCOs such as zinc oxide are being developed for ultra-violet light emitting diodes and lasers.[12] The "holy grail" for TCO researchers is the development of all transparent electronics[13-15] with properties that are comparable to classic

semiconductors. The essential goal in much of TCO research is to improve the conductivity without adversely influencing the transparency.

1.1.1. The Physics of TCOs

The unique properties possessed by TCOs have generally been explained by the combination of a large fundamental band gap (E_g=3.1-3.6 eV)[16,17] and an inherent non-stoichiometry, or the ability to be doped in order to produce free electrons.[16] More recently, Freeman et al. have identified three fundamental conditions to produce transparent and conductive materials:[7] (1) a highly dispersed single *s* band at the bottom of the conduction band, (2) separation of this band from the valence band by a fundamental band gap large enough to exclude interband transitions in the visible range, and (3) band properties such that the plasma frequency is below the visible range.

The highly dispersed *s* band has two important consequences on the properties of TCO materials. First, the more highly dispersed the *s* band is the greater the Burstein-Moss[18] shift will be, this leads to a greater increase in the band gap as the free electron concentration increases. Second, the dispersion, or curvature, of the E vs. k relationship dictates the effective mass, m^*, of the conduction electrons according to the relationship in equation 1-1:[19]

$$m^* = \hbar^2 \left(\frac{\delta^2 E}{\delta k^2} \right)^{-1} \qquad \text{(Equation 1-1)}$$

Where $\hbar$ is Plank's constant divided by 2π, E is the electron energy, and k is the wave number. More highly dispersed bands have higher curvature in the E vs. k relationship, and therefore the free electrons have a smaller effective mass.

The effective mass of the electrons, which describes how electrons confined within a material behave in response to an electric field, also plays a crucial role in defining the property know as the electron mobility, μ:[19]

$$\mu = \frac{e\tau}{m^*} \qquad \text{(Equation 1-2)}$$

Where e is the charge of an electron, and τ is the electron relaxation time. The relaxation time, or time between collisions, is determined by the various scattering mechanisms at play in the material. The cumulative effect of all of the scattering mechanisms on the mobility adds in a parallel fashion. Some of the important scattering mechanisms that limit mobility in TCOs are lattice scattering (due to phonons) limited mobility (μ_L), ionized impurity scattering (resulting from ionized donors) limited mobility (μ_I), and grain boundary scattering limited mobility (μ_G). Therefore the total mobility can be expressed as:[20]

$$\mu = \left(\frac{1}{\mu_L} + \frac{1}{\mu_I} + \frac{1}{\mu_G} .... \right)^{-1} \qquad \text{(Equation 1-3)}$$

The fundamental material property that is defined based on the ability of electrons to migrate through a substance is the conductivity, σ:[19]

$$\sigma = \mu N e \qquad \text{(Equation 1-4)}$$

Where N is the free carrier concentration. In order to obtain a material that has a high electrical conductivity, it is necessary to produce a large number of free electrons, use a material that allows electrons to respond quickly to an electric field (small effective mass), and to increase the relaxation time by reducing scattering events. Unfortunately, these concepts are not independent of one another. For example, increasing the free electron concentration by heavily donor doping a material will also decrease the mobility as a result of increased ionized impurity scattering. The freedom to choose low effective mass materials is limited to those materials that possess both optical transparency and electrical conductivity. Therefore, it becomes necessary to implement strategies that will decrease the dominant scattering times without significantly lowering the carrier concentration.

When considering any strategy to improve the conductivity of a TCO, it is also necessary to understand the associated effect on the optical properties of the material. Coutts et al.[9] have performed simulations using Maxwell's equations and the free electron approximation of the Drude theory.[21] In order to model the behavior of the electrons in response to electromagnetic radiation in the visible and near infrared part of the spectrum the equations for a Lorentz oscillator was used. The simulation results are shown in figure 1-1. Figure 1-1(a) shows the effect of increasing the free carrier concentration on the position and magnitude of the plasma absorption while all other variables are held constant. Clearly, at high free carrier concentrations the optical

(a)

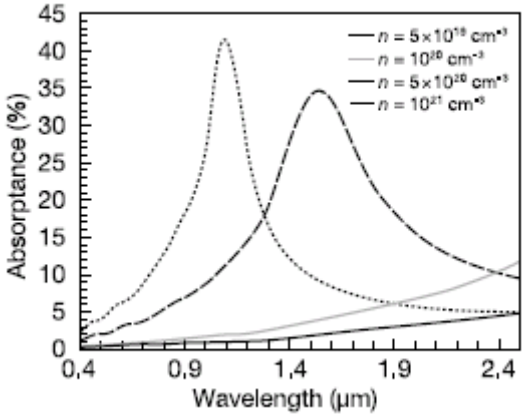

(b)

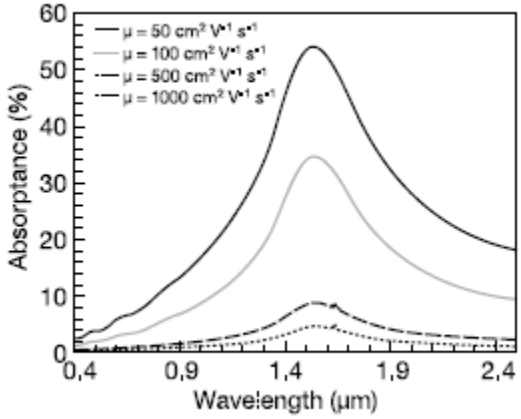

Figure 1-1(a) The effect of carrier concentration on the free-carrier absorption, from Coutts et al.[9] (b) The effect of mobility on the free-carrier absorption, from Coutts et al.[9]

transmission begins to become compromised. Figure 1-1(b) shows the results of the simulation when mobility is allowed to vary while all other variables are held constant. The plasma absorption not only remains at the same wavelength, but it also decreases in magnitude as the mobility increases. The simulations from Coutts suggest that in order to improve the electrical conductivity of a TCO without compromising the optical transmission one must focus on strategies that will increase the mobility.

1.1.2. Applications of TCOs

The largest application of a TCO material is as a coating for architectural glass to produce energy efficient windows. Tin oxide is the material of choice for this application owing to it's low emissivity of 0.16.[3] These low emissivity windows use TCOs in a passive role, whereas the next generation of energy efficient windows will use TCOs as a transparent electrode to control electrochromic switching.[22] "Smart", elecrochromic windows offer an exciting possibility to dramatically improve the energy efficiency of the world's office buildings and homes.

The TCO application that has been growing steadily is its use as a transparent electrode for flat panel displays and touch screen devices. Historically, Tin doped Indium oxide (ITO) has been the material of choice for these applications; however, with the demands of larger screens and faster switching better TCO properties will be needed.[3,12,23] No matter what technology is invented to improve the picture quality of flat panel displays, it appears that a transparent front electrode will be necessary to control the individual pixels.

Along with energy efficient windows, another place where TCOs can be used to help combat the global energy crisis is as a front contact in photovoltaic cells. The role of the TCO on the overall efficiency of the solar cell is an area of ongoing research.[24-26] In this application, TCOs compete with narrow metallic fingers[20] as an alternative way to transfer the created charge carriers to the external load. Zinc Oxide, Tin Oxide, and Indium Oxide all doped with various elements have been used as front contacts for solar cells. The choice in any particular situation is dependent on issues of material compatibility, stability, and application requirements.[27]

The possibility of band gap engineering[28,29] along with the development of p-type[5,30,31] TCOs have made the possibility of all-transparent semiconductor devices[13] a reality. Zinc Oxide, the material system focused on in this study, is also being investigated (as an alternative to GaN) for it's short wavelength emission characteristics.[12,32,33]

1.2. Zinc Oxide

Of the binary oxides (In_2O_3, CdO, SnO_2, Ga_2O_3, ZnO) that exhibit transparent conducting behavior, ZnO offers a desirable combination of relative abundance of raw material, low cost, and low toxicity. ZnO also has an exciton binding energy of 60 meV[34] which makes it an interesting material for optoelectronic applications such as blue/UV light emitting diodes and laser diodes.[35] Recent progress leading to the ability to grow single crystal substrates,[34] and the large number of research projects focusing of the

development of p-type ZnO[36] seem to put ZnO in a position to be a valuable material system for many years to come.

1.2.1. Crystal Structure and Band Structure

Under normal conditions, ZnO crystallizes in the hexagonal wurtzite structure with lattice constants a = 3.24angstom, and c = 5.19angstrom.[16] The atoms are tetrahedrally coordinated with point group 6 mm, and space group $P6_3mc$ producing polarity along the c-axis.[35] When deposited on amorphous substrates ZnO grows preferentially in the (002) orientation,[37] with its c-axis perpendicular to the substrate.

ZnO is a direct band gap semiconductor[34] with the top of the valence band being formed by O^{2-} 2p levels, and the bottom of the conduction band being formed by Zn^{2+} 4s levels.[35] The electronic band structure of ZnO has been considered theoretically by many different methods including empirical pseudopotential,[38] self-consistent field approach using an oxygen nonlocal ionic pseudopotential,[39] semiemperical sp^3 tight-binding,[40] linear muffin-tin orbital using the atomic sphere approximation(LMTO-ASA),[41,42] all electron Green function-screened coulomb interaction approximation (GW) using the local-density approximation (LDA) and LMTO,[43] LDA using nonlocal pseudopotentials and atomic self-interaction corrections,[44] and density functional theory (DFT) using the generalized gradient approximation with empirical self-interaction corrections.[45] The

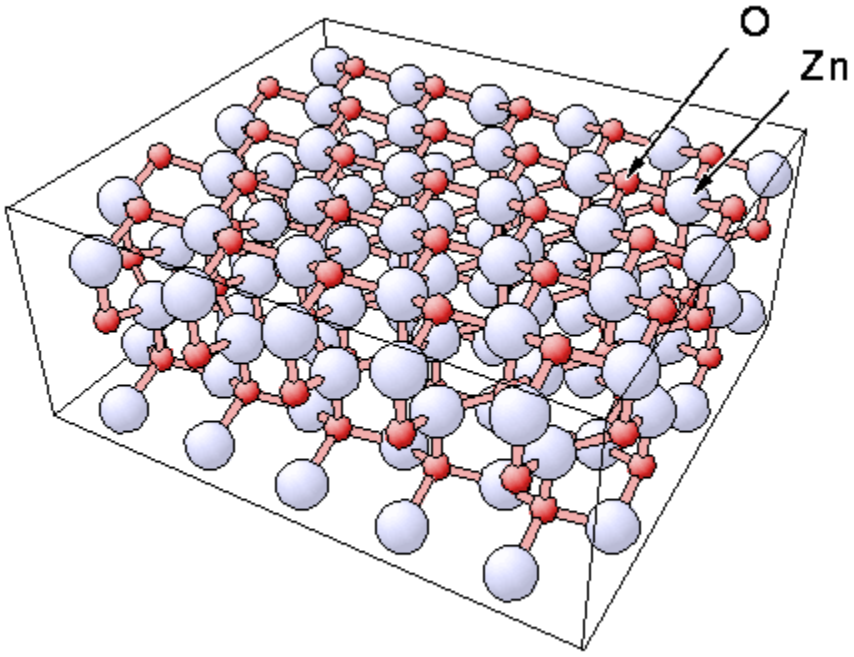

Figure 1-2 Hexagonal wurtzite structure of ZnO.

From: http://w3.rz-berlin.mpg.de/~hermann/hermann/BalsacPictures/ZnO.gif

most recent calculations, performed by Erhart et al.,[45] produce the energy band diagram shown in figure 1-3. The shaded band represents the calculated band gap, which is significantly less than the experimental value; this is standard for ZnO band calculations and has yet to be rectified. The conduction band in the diagram has been rigidly shifted to correspond with the experimental value of the band gap, ~3.4 eV.

1.2.2. Growth of Polycrystalline and Epitaxial Thin Films

ZnO thin films have been grown by a variety of deposition techniques, on various substrates. Direct current reactive magnetron sputtering,[46] radio frequency magnetron sputtering,[47,48] pulsed laser deposition (PLD),[49,50] metalorganic vapor phase epitaxy,[51] spray pyrolysis,[52] and molecular beam epitaxy (MBE)[53,54] have all been used to deposit ZnO. Materials such as glass,[55] (100) silicon,[47] SiC,[53] r-plane, a-plane, and c-plane sapphire (Al_2O_3),[56,57] and bulk ZnO[58] have been the substrates used for the deposition of ZnO based thin films. Films grown on glass substrates are polycrystalline with predominant (002) fiber texture.[59] Whereas single crystal substrates produce epitaxial films with varying degrees of crystal perfection determined by the lattice mismatch between the ZnO film and the substrate.

The most frequently used substrate for the deposition of epitaxial ZnO thin films is c-plane sapphire ((0001) Al_2O_3). The space group for sapphire is R-3c, and it has a rhombohedral hexagonal crystal structure. The lattice constants for sapphire (Al_2O_3)

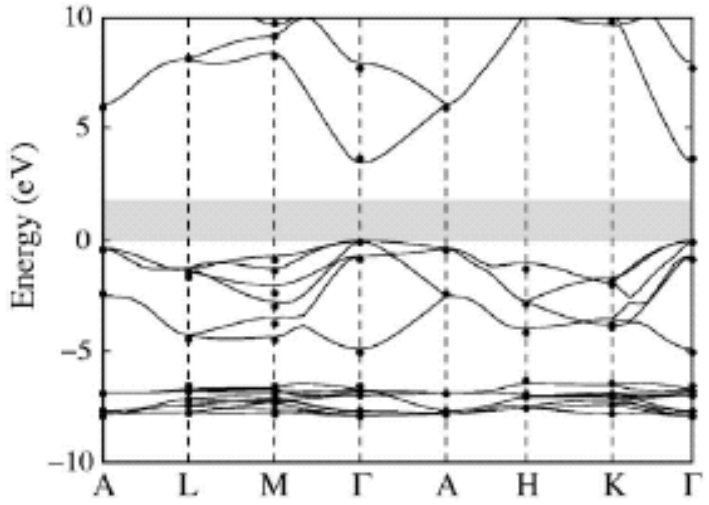

Figure 1-3 Electronic band structure of ZnO calculated with density functional theory (DFT) using the generalized gradient approximation with empirical self-interaction corrections, from Erhart et al.[45]

are, a = 4.758angstrom, c = 12.991angstrom. The thermal expansion coefficient along the a-axis is 7.5 x 10^{-6} /K, and along the c-axis it is 8.5 x 10^{-6} /K. For comparison, the ZnO lattice constants are: a = 3.24angstrom, and c = 5.19angstrom, and the thermal expansion coefficients for ZnO are 2.9 x 10^{-6} /K along the a-axis, and 4.75 x 10^{-6} /K along the c-axis.[60] If ZnO were to grow epitaxially on c-plane sapphire by lattice matching the unrelaxed misfit strain ($\varepsilon_c = a_{ZnO} / a_{Al_2O_3} - 1$) would be ~32%. Lattice matching epitaxy (LME) typically occurs only for systems where $\varepsilon_c \leq 8\%$, and this strain is eventually relaxed by the formation of dislocations after the critical thickness is reached.[61] Narayan et al.[60,61] have proposed a different type of epitaxy know as domain matching epitaxy (DME) that accounts for epitaxial growth in systems with $\varepsilon_c \geq 8\%$. For ZnO deposited on c-plane sapphire, this involves a 30^o rotation of the ZnO basal plane such that the $(2\bar{1}\bar{1}0)$ planes of ZnO (d = 3.2536 $\mathring{A}$) are aligned with the $1/2\,(30\bar{3}0)$ plane of sapphire (d = 2.7512 $\mathring{A}$). This rotation reduces the misfit strain to ~18%, which falls to 15.44% when thermal expansion was taken into consideration for the growth temperature (790^{o}C by PLD). The rotation matches zinc atoms in the growing film with the oxygen sublattice of the substrate. The DME is accomplished by 5 or 6 ZnO $(2\bar{1}\bar{1}0)$ planes matching with 6 or 7 Al_2O_3 $(30\bar{3}0)$ planes, the extra Al_2O_3 planes terminate at the interface as misfit dislocations, see figure 1-4. Dislocations within the first few monolayers of growth accommodate the majority of the strain, after which the film grows mostly strain free. This was confirmed

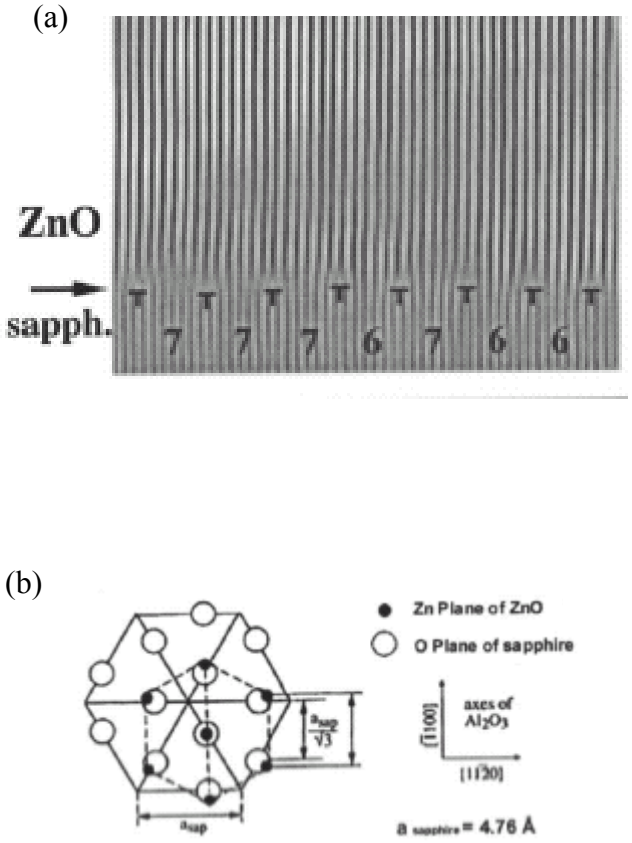

Figure 1-4 (a) Fourier-filtered TEM image of ZnO film deposited on c-plane sapphire showing the DME of 5 of 6 $(2\bar{1}\bar{1}0)$ planes of ZnO with 6 of 7 $(30\bar{3}0)$ planes of sapphire. (b) Diagram of the 30° basal plane rotation which allows ZnO to grow epitaxially on c-plane sapphire by DME, from Narayan et al.[61]

using in-situ XRD measurements and TEM results. The other predominant defects found in the films were threading dislocations in the basal plane with $1/3\langle 11\bar{2}0\rangle$ Burgers vectors, stacking faults with a density of 10^5 cm^{-1}, and inversion domains with oxygen terminated polarity; however, the films had very good overall crystal quality with a rocking curve width of 0.16^o.[60]

Gerthsen et al.[51] used metalorganic vapor phase epitaxy to grow ZnO on (0001) Al_2O_3 substrates with a 2 μm thick GaN buffer layer, and used TEM to study the defect structure. They found a high density of stacking faults that were terminated by Frank partial dislocations with Burgers vectors $1/6\ \langle 2\bar{2}03\rangle$. They attributed the stacking faults to the accumulations of vacancies (oxygen) or interstitials (zinc atoms) that would lead to a missing or extra (0002) plane in the films. The local nonstoichiometry was discussed in terms of its possible effect on the electrical properties of intrinsic ZnO films.

Vigue et al.[62] and Kang et al.[63] used plasma-enhanced and electron cyclotron resonance-assisted MBE respectively to deposit ZnO on (0001) sapphire. Vigue et al. found that 2D and 3D growth modes were possible depending on the deposition conditions and the use of buffer layers. Although they found a trade off between high crystal quality (3D growth) and smooth surface morphology (2D growth), they didn't find a correlation between the growth mode and the optical or electrical properties of the films. Kang et al. grew high quality films with rocking curve FWHM values of 0.52^o, and reported the same 30^o rotation of the ZnO basal plane relative to the Al_2O3 lattice that was reported by Narayan et al.[61]

Ohkubo et al.[64] used laser MBE to grow ZnO on (0001) sapphire substrates. They grew films on as-polished substrates, and on atomically flat substrates produced by annealing. The as-polished substrates produced ZnO films with the basal plane rotated 30^{o} relative to the sapphire substrate. The atomically flat substrates produced both 30^{o} rotated films and films that were lattice matched to the substrate depending on the growth conditions. The authors explain the transition in terms of kinetic (low temperature) and thermodynamic (high temperature) factors, with the growth temperature being the crucial variable. The thermodynamically more stable configuration was found to be the oxygen terminated, 30^{o} rotated films. The authors also observed a polarity inversion that corresponded to basal plane alignment. Films that were rotated 30^{o} were oxygen terminated, and the lattice matched films were zinc terminated. The best crystal quality (ω FWHM = 14.4 arcsec) was achieved for rotated, oxygen terminated films grown at 835^{o}C.

Park et al.[65] grew epitaxial ZnO films on (0001) sapphire by radio-frequency magnetron sputtering and used real time synchrotron x-ray scattering to investigate the nature of the crystal growth. They found highly strained two-dimensional (2-D) growth for the first 4.5 nm, followed by a 2-D/3-D mixed mode of growth up to 18 nm, after which the film grew in a 3-D columnar growth mode. The authors attribute the growth mode transitions as a means to relieve strain caused by the large lattice mismatch between the film and substrate.

As mentioned previously, ZnO based films have also been grown on orientations of sapphire other than c-plane. Igasaki et al.[57] used radio frequency magnetron sputtering

to deposit ZnO:Al on $(11\bar{2}0)$ plane sapphire. They discovered that the films grew with a (0001) orientation with varying degrees of internal stress. Yamauchi et al.[56] grew ZnO on both c-plane and r-plane sapphire using plasma assisted MBE and noted that epitaxial growth could be achieved on the r-plane sapphire at lower temperatures. They also describe fundamental difference in the growth modes and film morphology depending on the substrate that was used. Srikant et al.[66] grew ZnO:Al films on c-plane, r-plane, and a-plane sapphire and reported the effects of the substrate orientation on the electrical properties.

ZnO has also been deposited on substrates other than sapphire. Puchert et al.[47] deposited ZnO on SiO_2/Si (100) using radio frequency magnetron sputtering. They reported that the films grew with a (0001) orientation with small grains (~10 nm) and high biaxial compressive stress (~6 Gpa). The researchers were able to increase the grain size and reduce the compressive stress by using a post deposition anneal. Jou et al.[67] deposited ZnO on Si and GaAs substrates using radio frequency magnetron sputtering. The authors noted increased compressive stress in the films grown on Si and attributed their findings to a higher degree of crystallinity leading to a peening effect. Nakamura et al.[68] successfully deposited epitaxial (0001) ZnO films on the (111) plane of cubic $(LaAlO_3)_{0.3}(Sr_{0.5}Ta_{0.5}O_3)_{0.7}$ using pulsed laser ablation. They attributed their success to the fact that both crystal planes share the C_6 symmetry. Bellingeri et al.[69] were able to achieve room temperature mobilities as high as 70 cm^2/Vs by depositing ZnO on (110)

$SrTiO_3$ using pulsed laser ablation and a low temperature ZnO buffer layer. Low temperature mobilities reached as high as 400 cm^2/Vs at 10 K.

1.2.3. Sputter Deposition of Thin Films

The work of Park et al.[65] is of particular interest since they use sputtering to deposit their films, which is the same deposition method used to grow the films in this thesis. Sputtering offers unique challenges and benefits when compared to other physical and chemical vapor deposition techniques. The defining characteristic of sputtering is the interaction of the growing film with the energetic plasma. The interaction of the film surface with ions and neutrals from the plasma is crucial in determining the crystal structure of the film.[2] Figure 1-5 shows the multitude of interactions that are possible between a film surface and the ions, neutrals, and electrons present during the sputtering process. The effect of energetic particle bombardment has been incorporated into a Structure Zone Model (SZM) for the growth of sputtered films. The classic SZM was proposed by Thornton[70,71] and is shown in figure 1-6. This work was done on sputtered metallic films 20-250 μm thick, and the relevant growth parameters considered were the substrate temperature and the pressure. The different morphological zones are governed by the dominant atomic processes at the given growth temperatures. At low temperatures (Zone 1), adatom mobility is low and shawdowing effects produce a porous, columnar structure. At intermediate temperatures (Zone 2), surface diffusion is active and films become denser. At high temperatures (Zone 3), lattice and grain boundary diffusion is dominant, and equiaxed recrystallized grains are seen.[2] Mirica et al.[48,72] proposed a

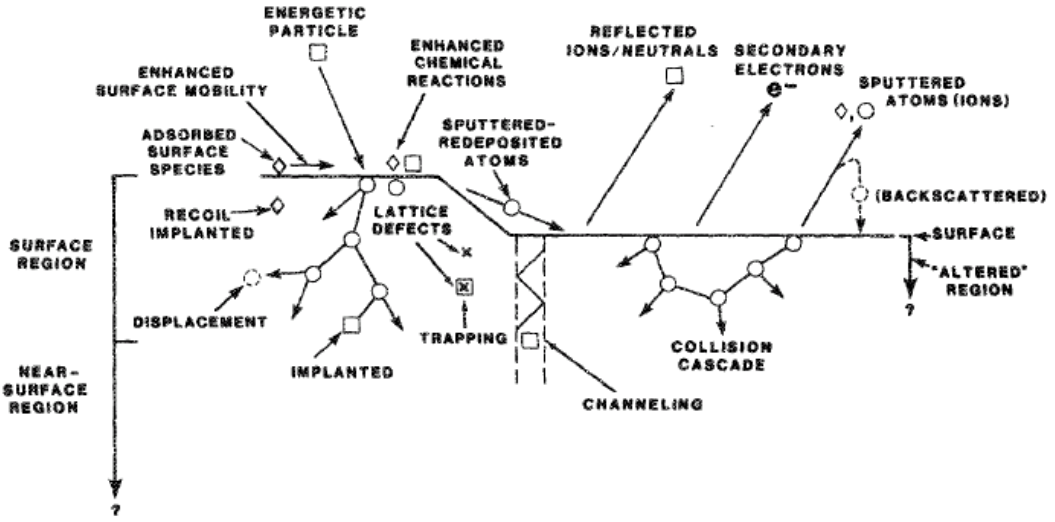

Figure 1-5 Schematic representation of the possible interactions between the film surface and the ions, neutrals, and electrons in the sputtering plasma, from Mattox.[73]

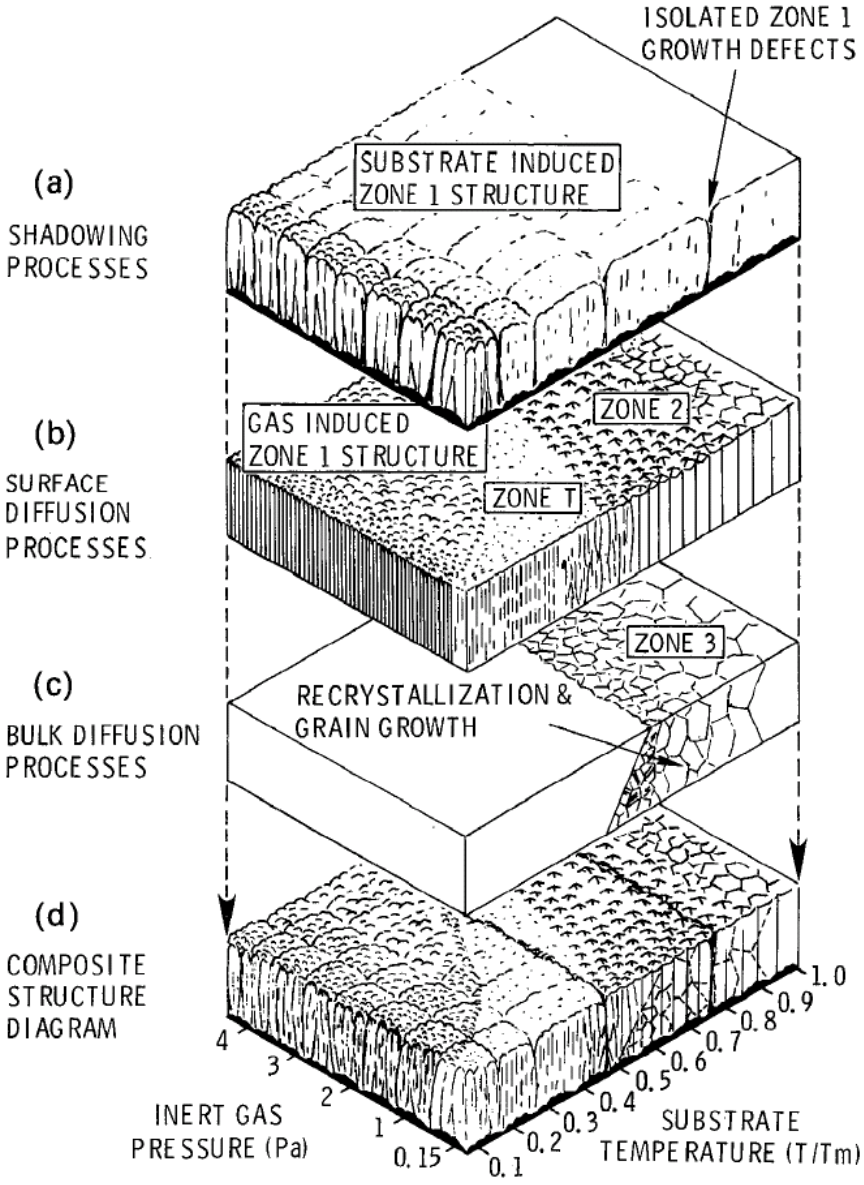

Figure 1-6 Structure Zone Model for sputtered metallic films, from Thornton.[70]

modified SZM specifically for reactively sputtered ZnO films. The major difference seen was a downward shift of the homologous temperatures ($T_S/T_{M,}$ the range studied was 0.13 to 0.43) where the transitions from one zone to the next occurred. They found no Zone 3 structure, and they distinguished between two Zone 2 structures, one with a faceted surface, and one with a pitted surface. The authors discovered a high density of stacking faults for films grown at low T_S, and a predominance of dislocations for films grown at high T_S. The modified SZM is explained by the competing effects of adatom mobility, incoming flux, and the rates of crystal nucleation and growth.[72]

In summary, the range of crystal quality of ZnO films varies considerably based on the growth technique, growth conditions, and substrate selection. However, the epitaxial relationship between ZnO films and c-plane sapphire substrates is well understood, and the morphological evolution of reactively sputtered ZnO films has been modeled.

1.2.4. Electrical Properties

The range of electrical properties for zinc oxide thin films has been extensively investigated. Intrinsic ZnO films[74] and films extrinsically doped with aluminum,[75] indium,[76] gallium,[77] fluorine,[78] and various other elements[6] have been grown and characterized in order to establish the range of possible electrical properties in this material system. Table 1-1 shows the electrical properties achieved for various dopants in ZnO films. Similar to the other transparent conducting oxides, ZnO strongly favors n-type doping and it has proven very difficult to produce satisfactory p-type ZnO (the status of p-type doping will be discussed later in this chapter).

Table 1-1 The electrical properties achieved for various extrinsic dopants in ZnO thin films, from Minami.[6]

Dopant	Doping Content (at.%)	Resistivity (10^{-4} Ω cm)	Carrier Concentration (10^{20} cm^{-3})
Al	1.6–3.2	1.3	15.0
Ga	1.7–6.1	1.2	14.5
B	4.6	2.0	5.4
Y	2.2	7.9	5.8
In	1.2	8.1	3.9
Sc	2.5	3.1	6.7
Si	8.0	4.8	8.8
Ge	1.6	7.4	8.8
Ti	2.0	5.6	6.2
Zr	5.4	5.2	5.5
Hf	4.1	5.5	3.5
F	0.5	4.0	5.0

The relationship between carrier concentration and hall mobility for ZnO films is shown in figure 1-7. The plot shows a maximum at ~ 2 x 10^{20} cm^{-3} that was modeled by assuming that there are two competing scattering mechanisms which are dominant in ZnO. At low carrier concentrations grain-boundary scattering dominates; at high carrier concentrations, free electron screening reduces the grain boundary barrier height, and ionized impurity scattering dominates. Minami was able to more accurately model the ionized impurity scattering by modifying the Brooks-Herring-Dingle theory[79] in order to take into account degeneracy and the non-parabolicity of the conduction band.

Ellmer[80] has also investigated the electrical properties of ZnO and found that the Brooks-Herring-Dingle theory needed to be modified to take into account degeneracy and non-parabolicity in order to fit the experimental data at high carrier concentrations. Ellmer also suggested that impurity clustering, the formation of secondary phases, and the charge state of the donor may play a significant role in determining the electrical properties of ZnO.

Srikant et al.[81] proposed using the abrupt junction approximation to model the grain boundary scattering at low carrier concentrations for epitaxial ZnO films. Their experimental results suggest that the transition between grain boundary controlled scattering and ionized impurity controlled scattering occurs at ~ 2.5 x 10^{19} cm^{-3}. The derived equation for the grain boundary barrier height (Φ_B) is:

$$\Phi_B = \frac{eN_S^2}{2\varepsilon\varepsilon_0 n} - \frac{kT}{e} \qquad \text{Equation 1-5}$$

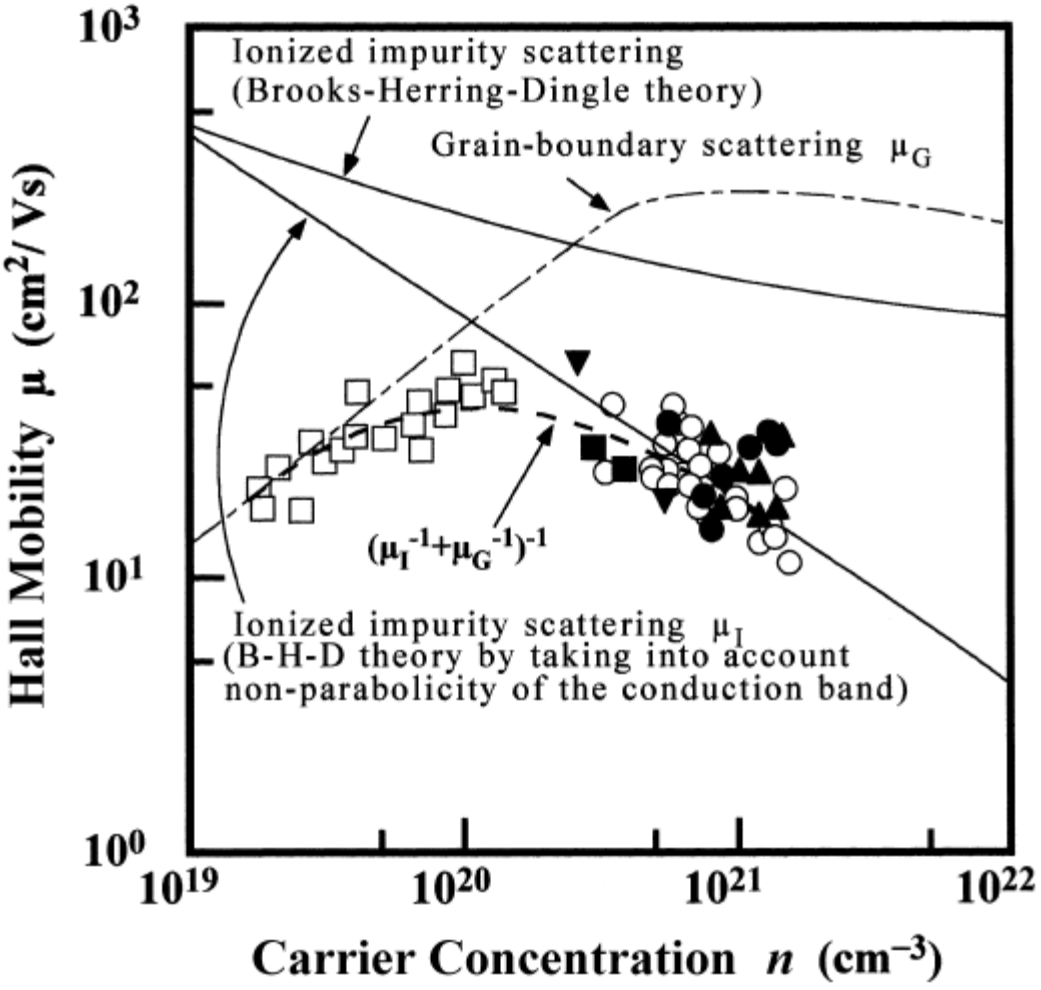

Figure 1-7 Relationship between carrier concentration and mobility in ZnO films, from Minami.[6]

Where N_S is the density of traps at the grain boundary, ε is the dielectric constant of the grains, and n is the carrier concentration. The mobility is then given as an exponentially decaying function of the barrier height. The fundamental relationship derived from the equations is that an increase in the number of carriers will reduce the barrier height and therefore increase the mobility.

Other studies have considered the effect of crystallographic orientation,[66,82] neutral impurity scattering,[82] and lattice vibration (phonon) scattering,[83,84] on the electrical properties of ZnO thin films. The mechanisms controlling the electrical properties in ZnO have been further investigated using temperature dependent Hall effect measurements.[35,85,86] As shown in figure 1-8, ionized impurity scattering is dominant at low temperatures, and phonon scattering is dominant at high temperatures.

The role of point defects in the strong n-type conductivity of intrinsic ZnO has long been a matter of debate. The initial explanation was that oxygen vacancies (V_O) and zinc interstitials (Zn_I) act as donors and were responsible for the free electrons inevitably present in intrinsic ZnO.[57,87] However, recent theoretical work suggests that these native defects are either not shallow donors or have a very high formation energy.[45,88] Based on first-principles density functional theory calculations, Van de Walle[89,90] proposed that hydrogen interstitials (H_I) should act as a shallow donor in ZnO. Experimental results[91-93] followed that supported the concept that hydrogen acted as a shallow donor in ZnO. Further theoretical investigations and experiments have suggested that H_I is not stable at room temperature and therefore does not serve to explain intrinsic conductivity in ZnO.[94]

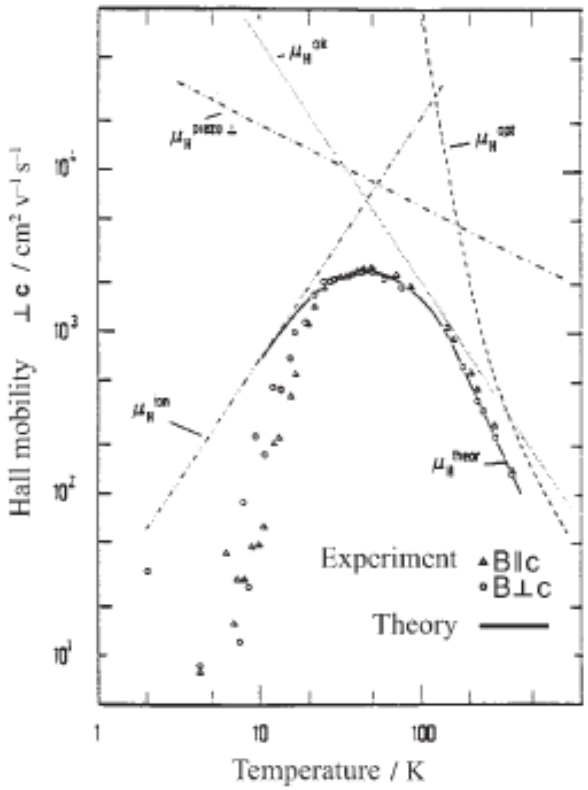

Figure 1-8 Temperature dependent Hall effect mobility for ZnO, from Klingshirn,[35] adapted from Wagner.[85]

One current explanation for intrinsic conductivity in ZnO is that free electrons result from hydrogen on an oxygen site (H_O), various hydrogen complexes, or complexes involving zinc interstitials.[36]

Perhaps the largest current area of research into the electrical properties of ZnO is the search for p-type material with high hole concentrations. This technological hurdle must be overcome in order to fabricate high quality p-n junctions and the plethora of semiconductor devices based on them. One of the first reports of p-type ZnO thin films was made by Minegishi et al.[95] where they achieved a hole concentration of 1.5 x 10^{16} cm^{-3} by using nitrogen as the acceptor. Other groups have since reported achieving p-type ZnO by doping with nitrogen,[96] arsenic,[97] sodium,[98] and aluminum/nitrogen codoping.[99] Hole concentrations on the order of 10^{17} cm^{-3} have been achieved.[100]

1.2.5. Optical Properties

Zinc oxide is one of a small number of materials that can be doped to conduct electricity (with a resistivity of $\sim 1 \times 10^{-4}\ \Omega - cm$) while remaining transparent in the visible region of the electromagnetic spectrum. The coexistence of these properties, which in most materials are mutually exclusive, is a result of a wide band gap (3.3 ev[101]) and the ability to be degenerately doped with shallow donors. The pursuit of high conductivities cannot be undertaken without considering the associated effect on the optical properties. This is because a high free carrier concentration, which can lead to high conductivities, is precisely the characteristic that causes materials to reflect visible electromagnetic radiation.

The effect of aluminum concentration (which is an electron donor in ZnO) on the optical transmission and reflection is shown in figure 1-9. The progression of plots demonstrates that as the free carrier concentration increases the plasma frequency moves to lower wavelengths (the free carrier concentrations are given on the figure). The implication is that the carrier concentration can only be increased so high in ZnO films before the plasma edge moves into the visible region. The other significant effect increasing the free carrier concentration has on the optical properties of ZnO is to shift the fundamental absorption edge to higher energies, the well-known Burstein-Moss effect.[102] For the samples in figure 1-9 the corresponding band gap energies (E_g) are: Sample A = 3.4 eV, Sample B = 3.55 eV, Sample C = 3.79 eV, and Sample D = 3.9 eV. Obviously the interplay of electrical and optical properties must always be considered when designing materials in the ZnO system.

ZnO has also been heavily researched for U-V light emitting applications owing to its large exciton binding energy of 60 meV,[103] and for surface acoustic wave applications owing to its low optical loss.[104]

1.2.6. ZnMgO

Another technique used to increase the band gap of ZnO is to alloy it with magnesium. Owing to the difference in the electronic configuration of Zn and Mg the addition of Mg to ZnO results in a distortion of the band structure and an associated

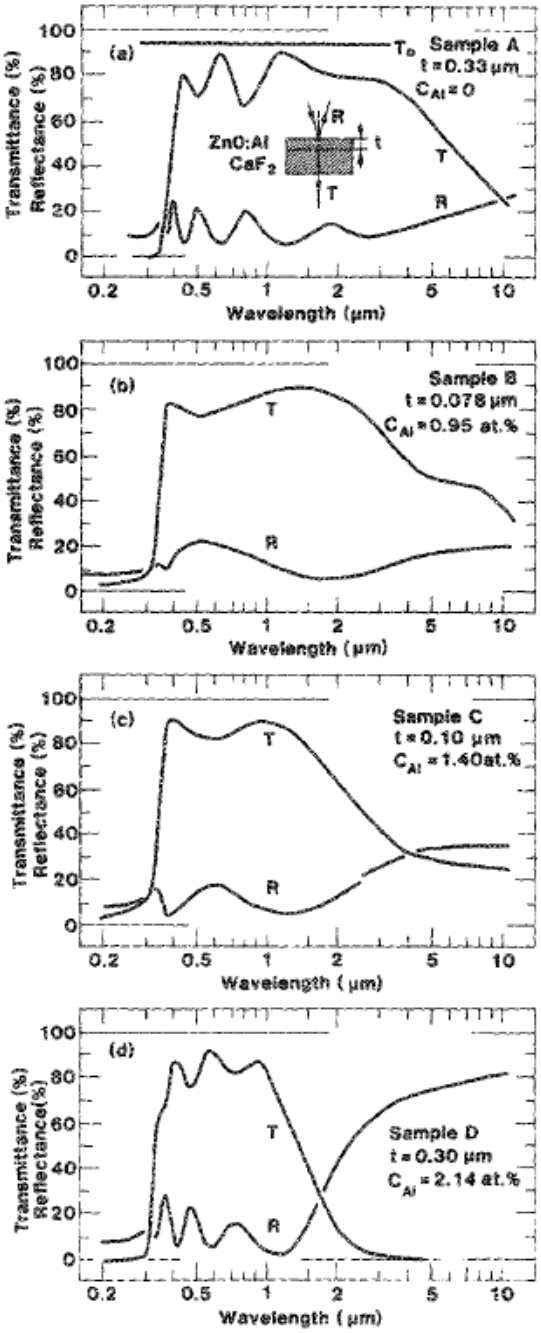

$n_e = 9.5 \times 10^{19}$ cm^{-3}

$n_e = 1.8 \times 10^{20}$ cm^{-3}

$n_e = 2.6 \times 10^{20}$ cm^{-3}

$n_e = 4.5 \times 10^{20}$ cm^{-3}

Figure 1-9 The effect of aluminum content on the optical properties of ZnO films, from Jin et al.[105]

increase in the band gap. Figure 1-10 shows the effect of Mg content of the band gap of ZnO, and the eventual change over to the cubic MgO phase.[106] The end points of thegraph represent hexagonal ZnO (E_g = 3.3 eV) and cubic MgO (E_g = 7.8 eV). The first report of band gap widening in ZnO using Mg was made by Ohtomo et al.[28] in which they used PLD to achieve a band gap of 3.99 eV for a Mg content of 33% while maintaining a metastable wurtzite phase. The authors note that the thermodynamic solubility limit of MgO in ZnO is less than 4 mol%. These results were confirmed by various groups using a variety of deposition techniques.[11,107] Subsequently, annealing techniques were developed to render RF magnetron deposited ZnMgO films n-type conductive.[108] Koike et al. have used aluminum doping of MBE deposited ZnMgO films to achieve a resistivity of 8 x 10^{-4} $\Omega - cm$ in a 20% Mg sample.[109] They observed a Burstein-Moss shift of the optical band gap, and were able to grow hexagonal wurtzite structure films up to a Mg content of 40%. Chen et at. used gallium doping of PLD deposited films along with a post deposition vacuum anneal to achieve a resistivity of 4.74 x 10^{-4} $\Omega - cm$ in a 10% Mg film which had a band gap of 3.9 eV.[110] There have also been reports of successful p-type doping of ZnMgO using lithium. Qui et al. used PLD to produce a p-type $Zn_{0.85}Mg_{0.15}O$:Li film that had a hole concentration of 1.25 x 10^{18} cm^{-3}, a hall mobility of 0.1 cm^2/Vs, and a resistivity of ~ 50 $\Omega - cm$.[111] The authors observed that increasing the Mg content increased the band gap and also increased the acceptor binding energy, thus decreasing the hole concentration at high Mg levels.

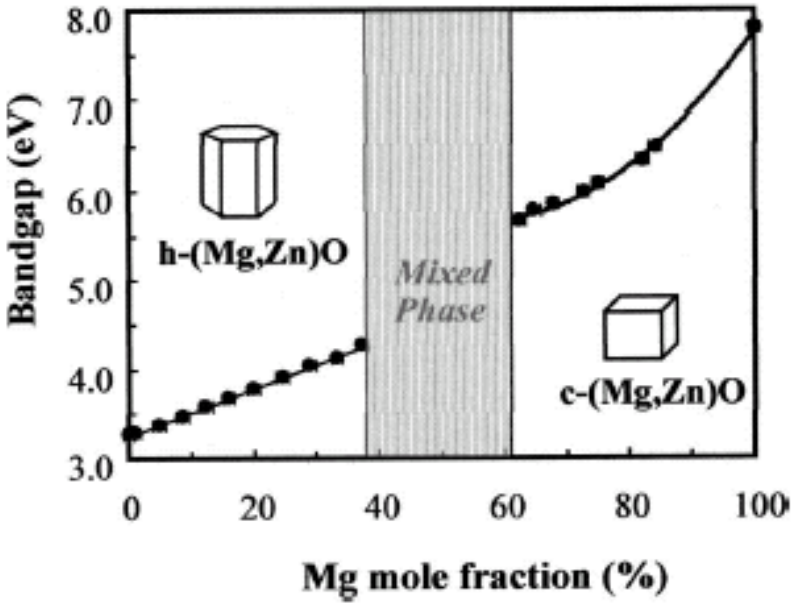

Figure 1-10 The effect of Mg content on the band gap on ZnO showing the transition from hexagonal ZnO to cubic MgO, from Takeuchi et al.[106]

1.3 Modulation Doping

The technique of modulation doping was first successfully demonstrated by Dingle et al.[112] in 1978. Since that time modulation doped structures have become ubiquitous in semiconductor devices throughout the electronics and telecommunications industries. The concept of modulation doping addresses a fundamental problem in doping semiconductor materials in order to generate free carriers; namely, the issue of carrier mobility being limited by ionized impurity scattering. When doping a semiconductor with donors or acceptors, a point of diminishing return is reached when the influence of scattering from the ionized dopants outweighs the benefits of additional charge carriers. Modulation doping is designed to overcome this problem by physically separating the free carriers from the ionized donors using a multilayer structure, as shown in figure 1-11. The key features in the structure are: a heterostructure between two materials with a conduction band (n-type doping) discontinuity, donor atoms incorporated into the larger band gap material (left side of figure 1-11), and an undoped spacer layer at the interface. As a result of the lower energy levels present in the smaller band gap material (right side of figure 1-11), the free electrons generated from the ionized donors transfer across the interface into the undoped material. The electrons are confined in the potential well at the interface where they are free to conduct as a two-dimensional electron gas (2DEG) without experiencing the effect of scattering from the ionized donors resulting from coulombic interaction.[113] Successful modulation doping increases the mobility of charge carriers by increasing the time between scattering events.

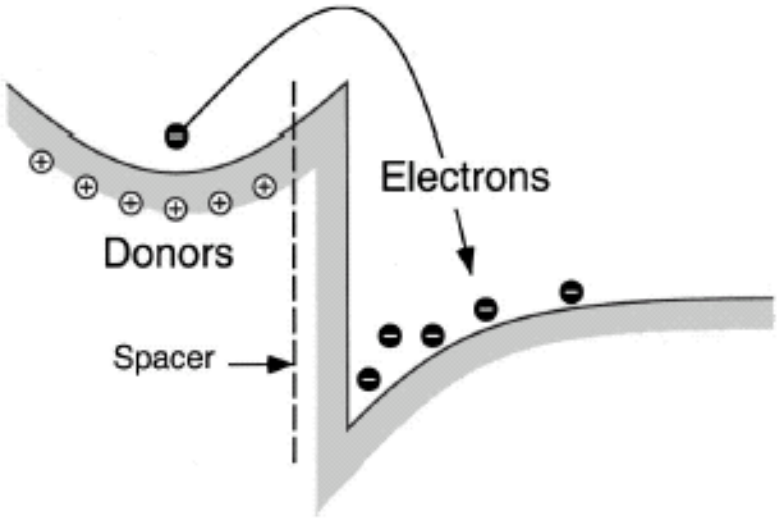

Figure 1-11 Schematic representation of a modulation doped structure, from Kroemer.[114]

Gossard and Pinczuk[115] outlined four essential factors necessary to produce semiconductor structures that will induce charge transfer and therefore realize the benefits of modulation doping: (1) absence of scattering centers in the undoped, smaller band gap conducting material, (2) smooth and pure interfaces at the heterojunctions, (3) minimization of traps and compensating centers in the wide band gap material, and (4) separation of the dopant atoms for the channel region by an undoped spacer layer.

1.3.1. Modulation Doped Material Systems

GaAs/AlGaAs was the first system to be modulation doped,[112] and it is the most heavily researched and technologically relevant. Modulation doped GaAs/AlGaAs structures are used to make high electron mobility field effect transistors (known as HEMFETS or MODFETS) for optoelectronic applications.[116] The aluminum serves the same role as Mg in ZnO, in that it increases the band gap compared to intrinsic GaAs. The AlGaAs layers are typically donor doped with Si to generate the free electrons.[117] The effect of spacer layer thickness,[118] electron density,[119] and quantum well width,[120] on the electrical properties have all been investigated. Other systems have also been modulation doped to achieve improved electrical properties, including: Si/SiGe,[121] InP/InGaAs,[122] ZnTe/CdMnSe,[123] and AlGaN/GaN.[124]

1.3.2. ZnO/ZnMgO Multilayers

In order to achieve improved properties in TCOs it has been suggested that the technique of modulation doping should be applied to a TCO material system.[125,126] Rauf[127] reported a modulation doping effect in tin doped indium oxide (ITO); however, the modulation in the films was lateral as opposed to vertical and the results were never reproduced.

As mentioned previously, adding Mg to ZnO increases the band gap, which makes the ZnO/ZnMgO system very interesting for modulation doping. Theoretical simulations predict that the band offset between ZnO and ZnMgO is Type I with the difference in band gap being evenly distributed between the conduction and valence bands.[128] Experimental results using photoluminescence suggest that up to 90% of the bandgap offset can be attributed to the conduction band discontinuity.[129] It has also been shown that ZnMgO can be donor doped with aluminum[109,130] and gallium.[110] Simulations have also been performed to predict electron transfer in multilayer ZnO/ZnMgO structures.[131] ZnO/ZnMgO superlattices have been grown primarily in an attempt to produce stimulated emission from excitons in the UV range.[132-134] Reports of the confirmed formation of a 2DEG and high mobilities in ZnO/ZnMgO systems have been made.[109,135,136] In these studies the films were grown by molecular beam epitaxy (MBE), and room temperature mobilities as high as 250 cm^2/Vs were reported. The sheet carrier concentration values in the 2DEG were on the order of $\sim 1 \times 10^{13}$ cm^{-2}, and carrier confinement was confirmed using capacitance voltage measurements and temperature dependent Hall meausurements. The effect of the magnesium content in the ZnMgO on

the room temperature mobility of the 2DEG in a single ZnO/ZnMgO heterojunction film is shown in figure 1-12. The increase in mobility is attributed to better electron confinement at the interface with increasing conduction band offset. The sheet carrier concentration in the 2DEG was relatively constant showing little dependence on the magnesium content. The ability to produce a high mobility 2DEG at ZnO/ZnMgO is the first step in producing high quality transparent transistors for transparent electronics.

1.4 Transparent Electronics

The majority of TCO applications are either as optical coatings (architectural glass) or as transparent electrodes (flat panel displays and solar cells). Presently, a good deal of the excitement in the field of TCOs centers around the development and optimization of all-transparent, active electronic devices.[13,137] As one example of transparent electronics, p-n junctions have been successfully demonstrated in ZnO based materials,[138,139] and transparent transistors have been fabricated using ZnO as a channel layer.[140-142] Furthermore, recent progress has been made into depositing transparent transistors on flexible substrates for the next generation of optical displays.[143]

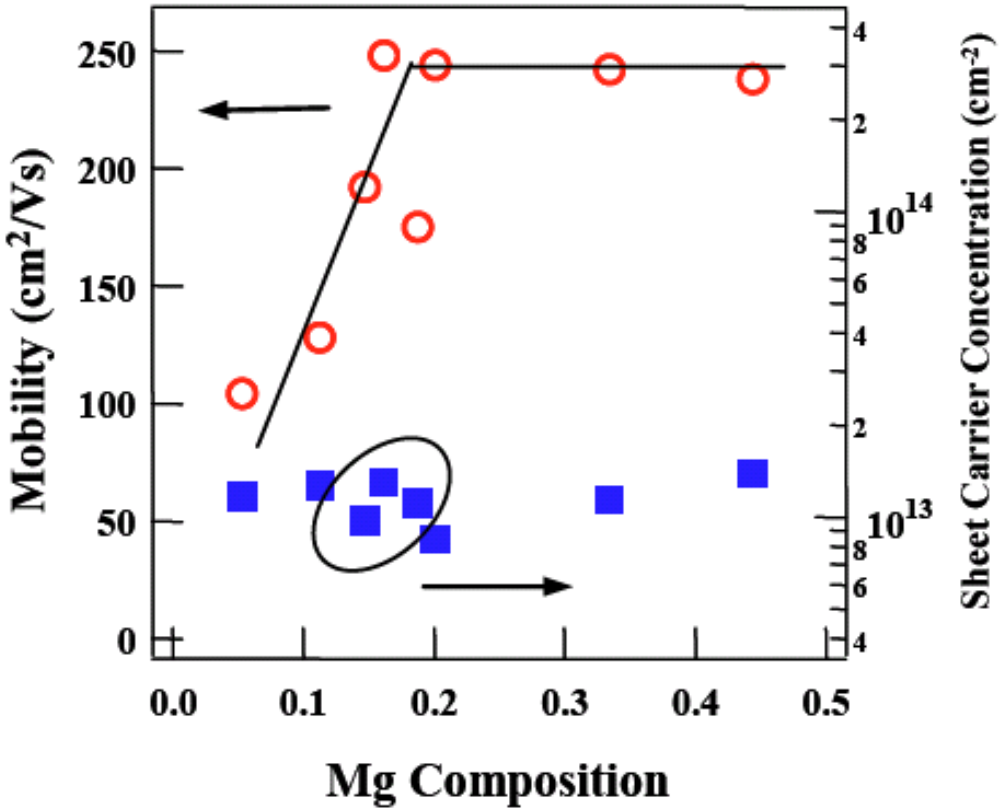

Figure 1-12 Electron mobility as a function of Mg composition for a single heterostructure ZnO/ZnMgO thin film, from Tampo et al.[136]

Chapter 2

Experimental Techniques

2.1. Thin Film Growth and Processing

2.1.1. DC Reactive Magnetron Sputtering

Monolithic ZnO, ZnMgO, and multilayer films were grown using direct current reactive magnetron sputtering in a custom built vacuum chamber.[1] The 16.5-inch bottom flange (outer diameter) was designed to incorporate 3 sputter sources, mounted at 35^{o} from the substrate surface normal in an up-facing geometry (see figure 2-1). The chamber was pumped to a base pressure of $\approx 1 \times 10^{-7}$ Torr (Granville-Phillips 307 vacuum gauge controller) using a Leybold Turbovac 360 water-cooled turbo pump. A Welch Duo-Seal 1376 mechanical pump, converted for use with Fomblin oil, was used as a backing pump. The chamber contained a load lock system that was pumped by Alcatel 5080 tubo pump, and backed by a Welch Duo-Seal 1397 mechanical pump.

The target to substrate distance was ≈12 cm, and was controlled by a Vacuum Generators Limited x-y-z manipulator. The double side polished (0001) sapphire and glass substrates were ultrasonically cleaned for 10 minutes each in acetone then methanol and blown dry with nitrogen before being placed in the load-lock. The substrates were clamped to a silicon wafer that was resistively heated using Sorensen DCR 600-.75B, and 80-6B power supplies; the temperature had previously been calibrated with a thermocouple attached to the sapphire. The substrates were heated in vacuum at 600^{o}C

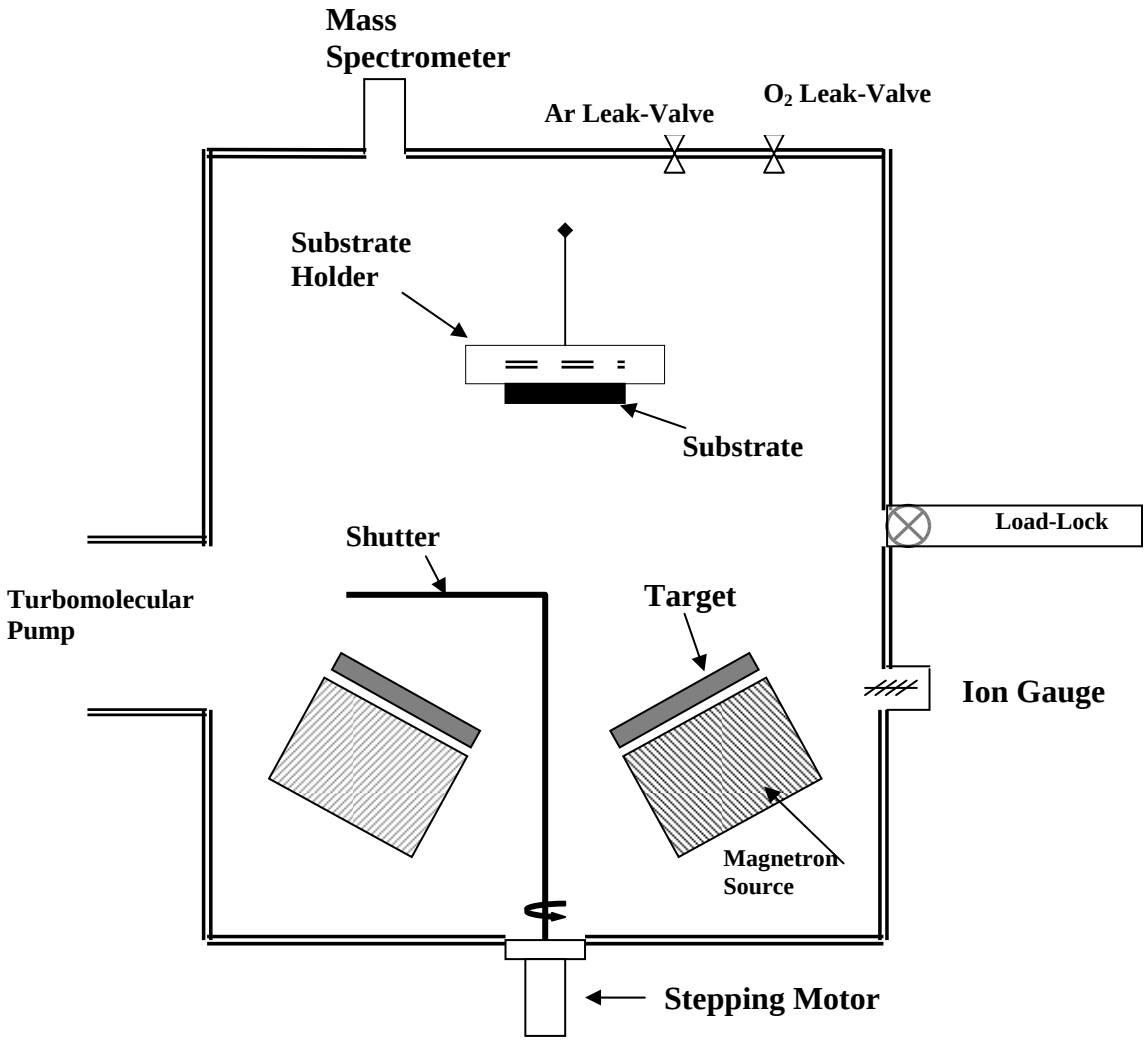

Figure 2-1 Schematic diagram of the direct current reactive magnetron sputtering chamber.

for 30 minutes in order to remove any residual air contamination, and then allowed to cool to the growth temperature. Films were grown at substrate temperatures ranging from $T_s = 175^oC$ to $T_s = 500^oC$.

Reactive and working gas pressures (typically 4.4-5.0 grade purity) were adjusted using MKS 1179-A mass flow controllers. The mass flow controllers had a maximum flow of 50 sccm, and were calibrated for the specific gas being used. The partial pressures of individual gasses were typically in the milli-Torr range. The targets exhibited hysteresis typical of reactive sputtering as seen in figure 2-2. Gas partial pressures were detected using an Inficon L100 mass spectrometer.

Three AJA International A320-U-A magnetron sputtering sources were used in the balanced high rate configuration. A computer controlled shutter was used to obtain growth from the various sources. The sources accommodated 5 cm diameter targets of zinc, aluminum, and various zinc/magnesium alloys. The targets, produced by ACI Alloys, were typically 4-5 N's pure. Advanced Energy MDX-1K, and MDX 500 power supplies were used to generate direct current power up to 150 W. An Advanced Energy Sparc-le 20 unit was used to suppress arcing during reactive sputtering. The targets were pre-sputtered in pure argon for 15 minutes to remove surface contamination, and then oxygen was introduced and the target voltage was allowed to stabilize for an additional 15 minutes. The shutter was then removed to commence growth.

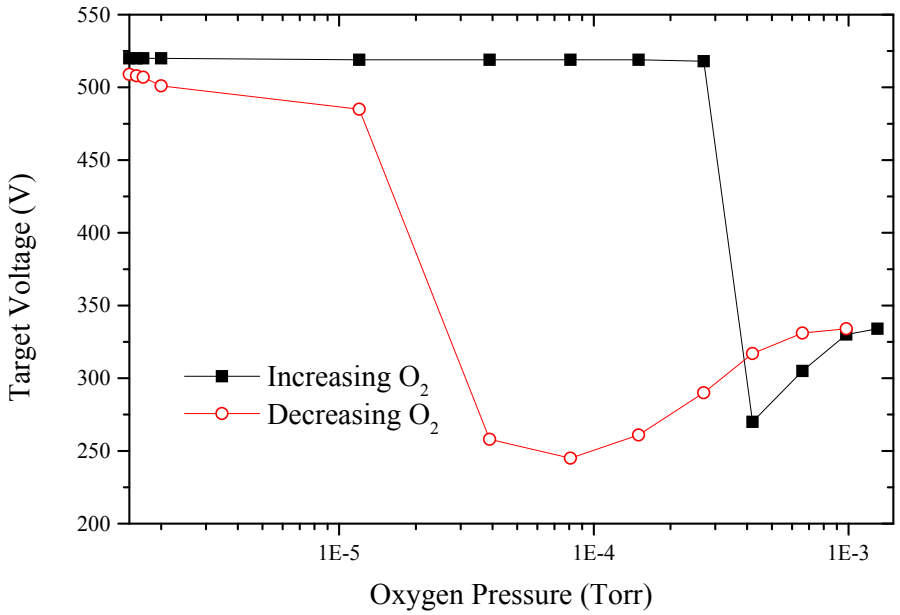

Figure 2-2 Target hysteresis for a ZnMgAl target (15 at% Mg, 2 at% Al). The target power was 50 watts, and the Argon pressure was 5 mTorr.

2.1.2 Thermal Annealing

Post deposition processing was accomplished by means of ex-situ thermal annealing. A Barnstead International, Thermolyne 79300 tube furnace was used to achieve temperatures up to 1000^{o}C. An alumina tube (~2 inch diameter) was fitted with end caps so that different gasses could flow over the samples during the annealing process. The flow rates of hydrogen, argon, and oxygen (typically 4.4-5.0 grade purity) were controlled by mass flow controllers (MKS 1179-A). The typical anneal time was 4 hours with an argon flow rate of 70 sccm and a hydrogen flow rate of 30 sccm.

2.2. Thin Film Characterization

2.2.1. Profilometry

Film thickness was determined using a Tencor P-10 surface profiler. A step was created during growth by masking part of the substrate with the clamp that held the substrate to the silicon block. Scans were taken at several locations along the step edge and an average thickness was calculated. Scans were typically 1000 μm long and performed at a rate of 20μm/sec. For certain films this thickness was confirmed by comparing them to values obtained from spectrophotometer data and scanning electron microscope images. Some films with thickness greater than 300 nm were also analyzed using a Metricon prism coupler.

2.2.2 Hall Effect Measurements

Room temperature electrical data was gathered using a BioRad HL5500 Hall effect measurement system that produced a magnetic field of 0.32 Tesla. The measurements were taken using the Van der Pauw geometry in order to determine resistivity, carrier concentration, and mobility (figure 2-3). A zero magnetic field voltage measurement was made to calculate the sheet resistance (R_S), and a Hall effect voltage (V_H) was measured and used to calculate a sheet carrier density (n_S). The two values were then used to calculate the mobility (μ) of electrons in the sample using equation 2-1, where q is the charge on an electron:

$$\mu = \frac{1}{qn_S R_S} \qquad \text{Equation 2-1}$$

Small Indium (Alfa Aesar 6N's pure) contacts (~2mm diameter) were placed at each corner of the approximately square samples using a soldering iron. The indium was used in order to improve the contact between the sample and the metallic probes. Temperature dependent Hall effect measurements were taken using a Janis Research cryostat that was capable of operating with a liquid nitrogen reservoir (temperatures down to ~77.7 K) or a continuous flow of liquid helium (temperatures down to ~4.4 K). A Walker Scientific electromagnet was used to supply an electric field of 0.25 Tesla to the temperature dependent system.

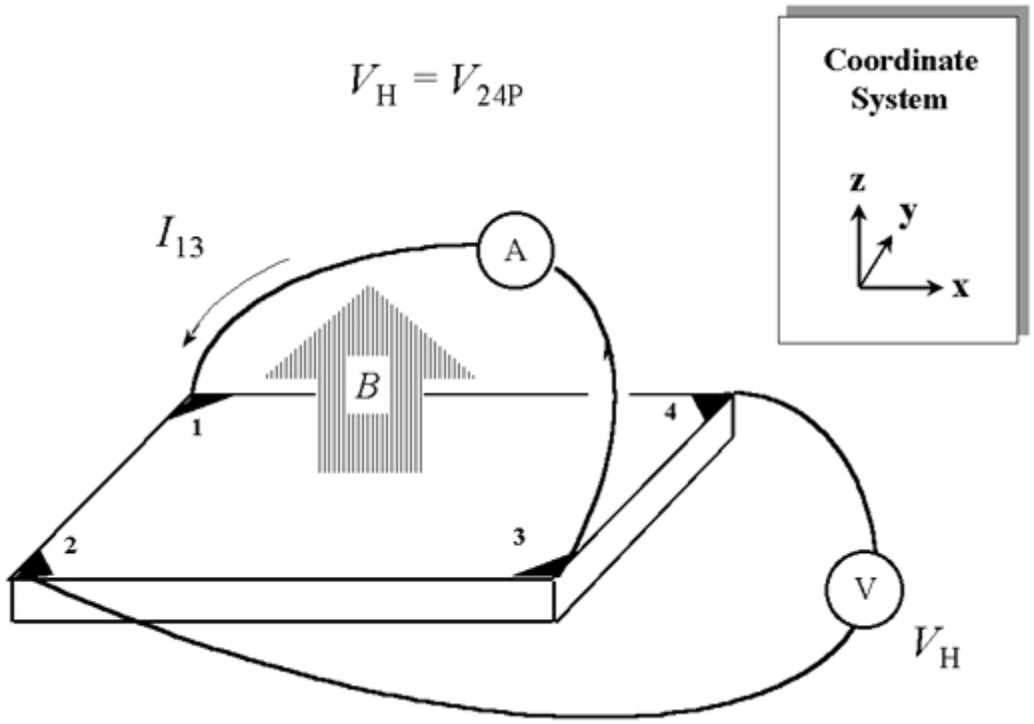

Figure 2-3 Van der Pauw geometry used for Hall effect measurements.

From: http://www.eeel.nist.gov/812/effe.htm#vand

2.2.3. UV-VIS-NIR Spectrophotometry

Optical transmission scans of the samples were performed using a dual beam Cary 500 Scan UV-VIS-NIR spectrophotometer. The effect of the substrate was subtracted from the film scans by using the dual beam geometry, where one beam goes through the sample and one beam goes through a blank substrate. Scans were performed with electromagnetic radiation covering wavelengths from 3000 nm down to 200 nm with a measurement taken for each integer value of the wavelength. The optical transmission scans were used to determine the optical band gap of the films by plotting the square of the optical absorption coefficient as a function of photon energy and then using the extrapolation method.[2] The extrapolation method is based on the following relationships:

$$\%T = e^{-\alpha t} \qquad \text{Equation 2-2}$$

$$\alpha = (h\nu - E_g)^{1/2} \qquad \text{Equation 2-3}$$

Where %T is the transmission measured with the Cary 500, α is the optical absorption coefficient, and t is the film thickness. Equation 2-2 assumes that most of the electromagnetic radiation is transmitted or absorbed close to the optical band gap, that very little is reflected, and that the band gap is direct. This is a reasonable assumption based on transmissions of ~95% in the visible part of the electromagnetic spectrum. In Equation 2-3; h is Plank's constant, ν is the frequency of the incident photons, and E_g is the optical band gap. Equation 2-3 assumes a direct band gap transition, which is the band structure for ZnO. Spectrophotometry data was also used to calculate film thickness by analyzing the interference fringes in the visible and near infrared wavelengths.[3] The

near infrared regions of the scans were used to compare the plasma wavelength to free carrier concentration.

2.2.4. X-ray Diffraction (XRD)

X-ray diffraction was performed to investigate film crystal quality, residual stress, and the epitaxial relationship. A Rigaku Ru200 12 kW copper point source x-ray generator was used to take $\theta - 2\theta$, rocking curve (omega scans), and phi scans of the thin film samples. The omega scans were taken around the (0002) peak at ~34.4^{o}, and the phi scans were taken of the $\{1\,\bar{1}\,01\}$ set of planes. The beam was focused on a vertical plane at the sample using a graphite monochrometer. A four circle Huber diffractometer (model D8211) was used to manipulate the sample relative to the beam using Spec software. The diffracted beam was detected using a high count rate Cyber-Star detector with an XIA calibrate attenuator filter box.

Low angle reflectivity scans were done to investigate the nature of multilayer samples. Layer thickness and interface quality was estimated by modeling the reflectivity data with a kinematical approximation and Parratt's recursive method.[4] A Rigaku ATX-G advanced thin film/in-plane diffraction system was used with an 18 kW copper line focus generator to make the reflectivity measurements. A Ge (111) asymmetric cut crystal was used to compress the incident beam in the horizontal plane.

2.2.5. Atomic Force Microscopy (AFM)

A Digital Instruments Scanning Probe Microscope was used in contact mode to image the surface of the films and to calculate a root mean square roughness. The microscope used a silicon nitride cantilever that reflected a laser onto a photodiode in order to measure changes in the height. Typical scan size was 5μm x 5μm and typical scan parameters were: a scan rate of ~0.5-2 Hertz, a scan velocity of 15.8 μm/s, and 256-512 samples per line.

2.2.6. Time-of-Flight Secondary Ion Mass Spectrometry (ToF-SIMS)

ToF-SIMS was performed using a Physical Electronics PHI THRIFT III system. A Ga^+ pulsed ion beam (5000 eV) was used to sputter surface atoms and clusters from the sample, after which they were analyzed in a mass spectrometer. A 100 μm x 100 μm area was sputtered away prior to analysis in order to remove any surface contamination and then a 25 μm x 25 μm region within the sputtered area was analzed using the ToF-SIMS. Elemental analysis was conducted and concentrations were determined by comparison to known standard samples. Depth profiling was conducted on the multilayer samples to determine layer thickness and interface integrity, and on monolithic samples to determine concentration profiles resulting from thermal annealing. The area that was sputtered away each cycle for depth profiling was 100 μm x 100 μm, and the analysis area was a 25 μm x 25 μm square within the sputtered region.

2.2.7. X-ray Photoelectron Spectroscopy (XPS)

Elemental and chemical analysis of the samples was performed using XPS, a 300 Watt x-ray source was focused on the samples in order to liberate core electrons that were then collected by an energy analyzer. The binding energy of the core electron is calculated by taking the difference of the energy of the incident x-ray and the kinetic energy of the emitted electron. An ion beam was used to sputter clean the surface of the samples prior to analysis, and an electron gun was used to suppress charging of the more insulating samples during analysis. XPS was also used to estimate the valence band offset between ZnO and ZnMgO:Al according to the equation:[5-7]

(Equation 2-4)

$$\Delta E_V = (E_{valance}^{ZnO} - E_{Zn2p}^{ZnO}) - (E_{valance}^{ZnMgO:Al} - E_{Mg2p}^{ZnMgO:Al}) + (E_{Zn2p}^{interface} - E_{Mg2p}^{interface})$$

Where the energies positions where determined for monolithic ZnO and ZnMgO:Al films, and the interface energies were determined from a bilayer film.

2.2.8. Electron Microscopy (SEM and TEM)

Scanning electron microscopy (SEM) was performed using a Hitachi S-4500 field emission microscope. Samples were cleaved to produce a clean cross-section and were used to obtain film thickness and grain morphology. Some samples were also observed in plan-view to analyze surface quality. Samples were coated in carbon or gold in order to reduce charging during electron exposure.

A multilayer sample was made electron transparent in cross-section so that it could be viewed using transmission electron microscopy (TEM). The sample was

analyzed using a JEOL JEM-2100F FAST TEM, and information was gathered about the interface quality, concentration profiles, and crystal structure. Pradyumna Prabhumirashi, working under professor Vinayak Dravid, performed the TEM work on the multilayer sample.

Chapter 3

Thin Film Growth and Characterization

3.1 Introduction

Experiments were conducted to determine the relationship between growth parameters and film properties. The goal was to explore the range of film properties that were achievable, and also to find the optimum conditions to grow epitaxial ZnO and ZnO:Al in our modified sputtering chamber.[1] Once the effects of the growth parameters on film properties were understood using zinc and zinc/aluminum targets, the results could be applied to the zinc/magnesium alloys. The growth parameters that were varied were substrate temperature (T_S), sputtering power, and oxygen/argon partial pressure during growth. The films were characterized using x-ray diffraction (XRD), atomic force microscopy (AFM), scanning electron microscopy (SEM), optical transmission, and Hall effect measurements.

3.2 ZnO Growth and Characterization

A typical set of x-ray diffraction peaks are shown in figure 3-1. The film was deposited on an unheated double-side polished c-plane sapphire (0001) substrate at an oxygen partial pressure of 1.5 mTorr, a total pressure of 3 mTorr, and a sputtering power of 50 W. Figure 3-1(a) shows the $\theta - 2\theta$ scan, the peak of the scan is shifted from the value of 34.4^{o} for annealed zinc oxide powder (JCPDS 80-0075). The shift to a lower peak angle is indicative of residual compressive stress in the film, which is to be expected

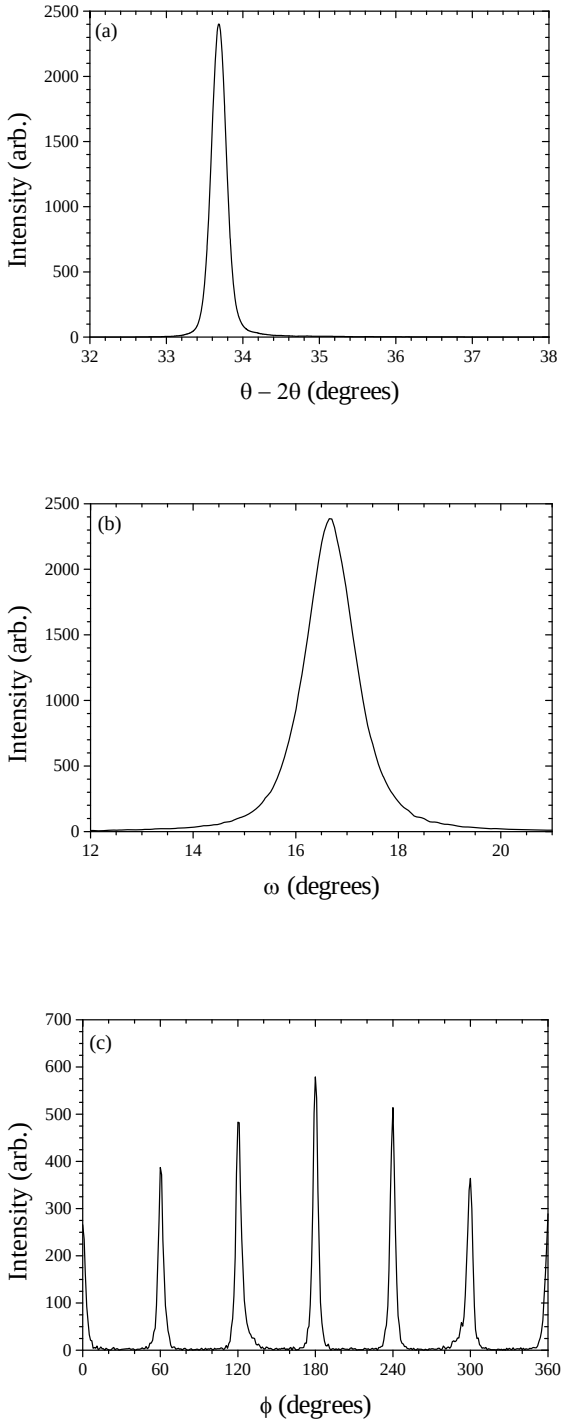

Figure 3-1 Typical x-ray diffraction θ–2θ (a), ω (002) (b), and ϕ $\{1\bar{1}01\}$ (c) scans for ZnO films reactively sputtered on unheated sapphire substrates.

for ZnO films grown by magnetron sputtering with no intentional heating.[2,3] The film stress (σ_{film}) was calculated using the elastic constants (C_{ij}) for bulk single crystal zinc oxide according to:[4]

$$\sigma_{film} = \left(\frac{2C_{13}^2 - C_{33}(C_{11} + C_{12})}{C_{13}} \right) \times \varepsilon_{film} \qquad \text{Equation 3-1}$$

Where ε_{film} is the film strain that can be determined from the $\theta - 2\theta$ peak position, since this peak is an indication of the atomic plane spacing (d_{0002}). Taking this into account, equation 3-1 reduced to $\sigma_{film} = -456(\Delta d_{0002} / d_{0002})$ GPa. For comparison, a ZnO sample grown at 300°C, 50 W, an oxygen pressure of 1 mT, and a total pressure of 5 mT had a $\theta - 2\theta$ peak position of 33.98° as grown; however, after an air anneal at 800°C for 2 hours, the $\theta - 2\theta$ peak position shifted to 34.44°C. The $\theta - 2\theta$ was also used to estimate the coherence length (grain size), D, using the Scherrer formula:[5]

$$D = \frac{0.94\lambda}{B\cos\theta} \qquad \text{Equation 3-2}$$

Where λ is the x-ray wavelength, B is the FWHM of the $\theta - 2\theta$ peak, and θ is the position of the $\theta - 2\theta$. The full-width at half-max (FWHM) of the rocking curve (ω) scan and the phi (ϕ) scan were used as indicators of the overall crystal quality of the films. The six-fold symmetry in the phi scan is a result of the epitaxial relationship between the ZnO film and single crystal c-plane sapphire substrate. The epitaxial relationship for this material system is known to be $(0001)ZnO \| (0001)Al_2O_3$ and $[\bar{1}2\bar{1}0]ZnO \| [\bar{1}100]Al_2O_3$,[6] and the phi scans are consistent with this orientation. Films

grown on Corning 7059 glass substrates show no peaks in the phi scans as expected when there is no driving force for in-plane alignment.

The effect of substrate temperature on the overall film crystal quality determined by measuring the FWHM of the omega and phi scans is shown in figure 3-2. In general, the crystal quality improved with increased substrate temperature up to 500^{o}C. Above 500 ^{o}C the growth rate significantly decreased, and it was difficult to deposit films at temperatures above 600 ^{o}C. For comparison, films grown on unheated Corning 7059 glass substrates had FWHM of the rocking curve peaks ranging from 2-6^{o}.[2] The improved crystal quality with increased T_S is explained by the surface adatoms being able to reach low-energy equilibrium positions prior to being incorporated into the growing film. Higher substrate temperatures increase adatom lifetime by imparting energy to the surface atoms, thus allowing them to avoid being trapped at non-lattice site positions. The 500^{o}C data point in figure 3-2(a) shows substantial improvement in crystal quality and can be explained by a combination of high T_S and lower growth rates as a result of adatom desorption at these high temperatures. A lower growth rate also allows surface atoms to bond at a lattice site before being incorporated into the film.

The effect of T_S on the root-mean-square (RMS) surface roughness is shown in figure 3-3. Unlike the XRD data, the AFM data shows a pronounced minimum between 200-300^{o}C. Being that we are interested in using these films as part of a multilayer structure, minimizing surface roughness is a key consideration in the effort to produce high quality layer interfaces. The trend in surface morphology can be understood in

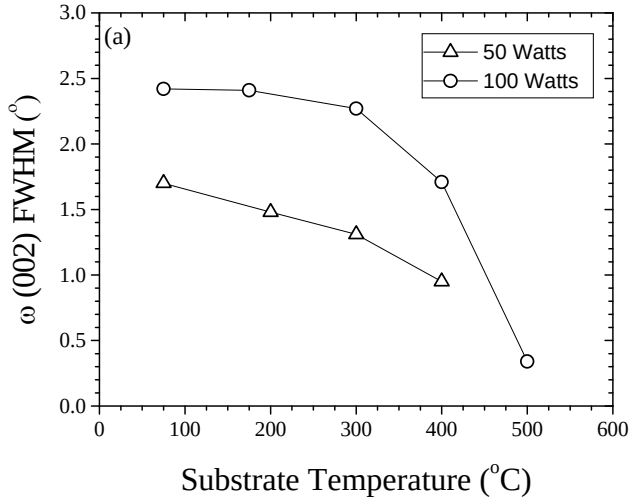

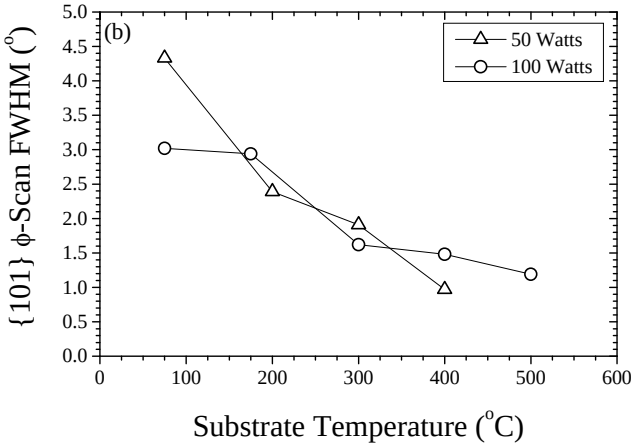

Figure 3-2 Substrate temperature dependence of the (0002) rocking curve FWHM (a) and $\{1\bar{1}01\}$ ϕ-scan FWHM (b) for ZnO films deposited at 50 and 100 Watts in 6 mTorr with 25%O_2.

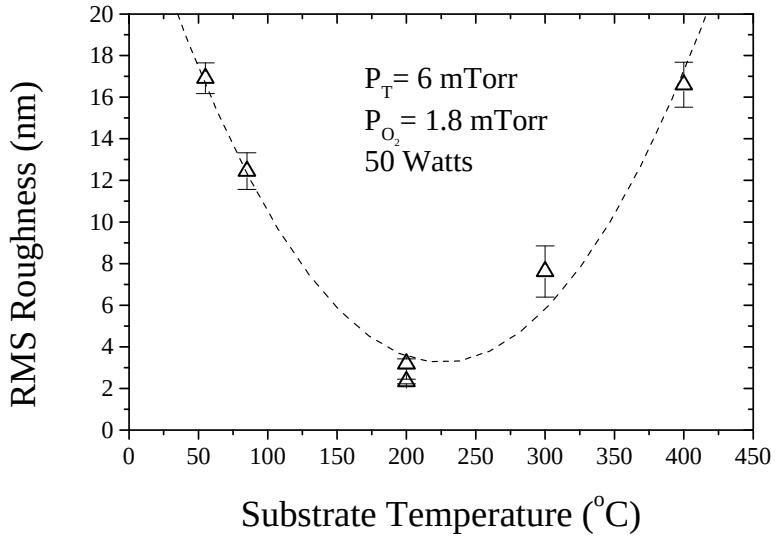

Figure 3-3 Effect of substrate temperature on surface roughness for ZnO films deposited at 50 Watts in 6 mTorr with 30% O_2.

terms of a structure zone model[7,8] for sputtered thin films. In this model the substrate temperature is a main factor in determining the dominant processes occurring during growth (shadowing, surface diffusion, bulk diffusion), and thus dictating the structure of the growing film. Our results are consistent with a porous columnar structure at low temperatures (Zone 1), a featureless structure at moderate temperature (Zone T), and a dense columnar structure at higher temperatures (Zone 2).[9] The evolution of film morphology with substrate temperature is highlighted in figure 3-4. The SEM images show a distinct progression, from porous to dense films as T_S increases, that is consistent with the structure zone model. The surface morphologies from the SEM and AFM images qualitatively agree with the RMS data, with the smoothest films being between 200-300^{o}C. The AFM images also indicate an increase in the coherence length (grain size) as T_S increases from 200-400^{o}C. This is consistent with the XRD data that showed improved crystal quality with increased T_S, where the FWHM of the $\theta - 2\theta$ peak is inversely proportional to the coherence length through the Scherrer equation.

The effect of sputtering power on the ZnO crystal quality is shown in figure 3-5. Figure 3-5(a) shows that both the rocking curve and phi scan FWHM values increased as the sputtering power was increased, with the best crystal quality being achieved at a target power of 50 W. At target powers above 100 W the crystal quality substantially degraded indicating that the Zn flux was too large for surface adatoms to find equilibrium lattice positions and bond with oxygen before being incorporated into the growing film. The effect of sputtering power on coherence length is shown in figure 3-5(b) for films

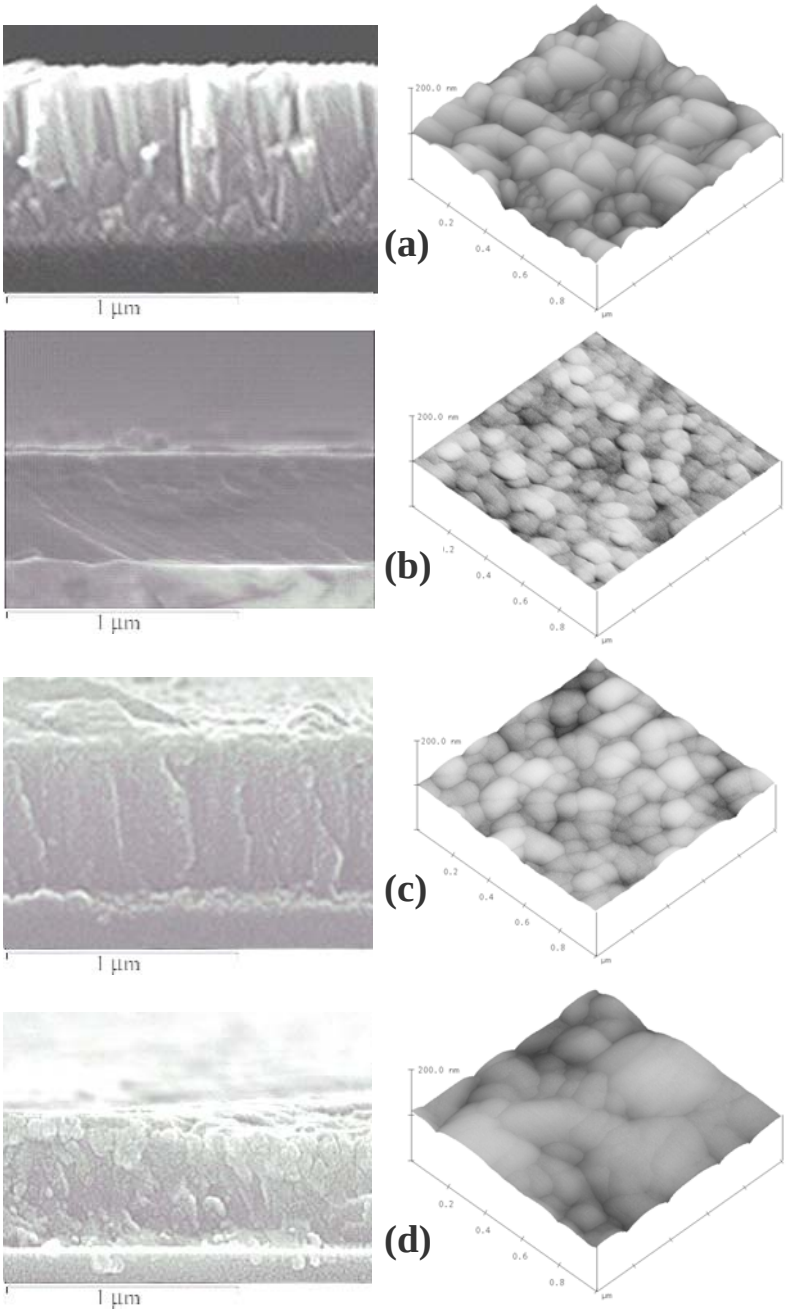

Figure 3-4 Substrate temperature dependence of fracture cross-sectional and surface morphologies as measured by SEM and AFM, respectively. (a) 80^{o}C, (b) 200°C, (c) 300°C, (d) 400°C.

grown to 500 nm and 1000 nm. In both cases the coherence length decreased as the sputtering power increased. The larger grains at lower sputtering power is consistent with the overall superior crystal quality seen in figure 3-5(a), and the mechanism leading to the larger grains can also be explained by increased adatom lifetime as a result of the lower Zn flux. For the given conditions, unheated substrate and ~25% O_2, the optimum sputtering power is 50 W.

To investigate the effect of oxygen content during growth on the film quality, a series of films were grown on unheated substrates with a sputtering power of 50 W. The oxygen partial pressure was adjusted to modify the oxygen:zinc flux ratio as shown in figure 3-6. XRD was used to characterize the overall crystal perfection and the coherence length of the films. Both the omega and phi FWHM plots showed a minimum at an oxygen content that corresponded to ~25% of the sputtering gas pressure (1.5 mTorr oxygen for the films in figure 3-6), indicating that films grown under these conditions had the best overall crystal quality. The coherence length (figure 3-6(c)) showed a maximum at ~25% oxygen indicating that the films with the highest crystal perfection also had the largest grain sizes. Growth conditions with an excess of oxygen or an oxygen deficiency led to films with poor crystal quality and a smaller coherence length. When the growth atmosphere contains an excess of oxygen the Zn adatom surface diffusion is limited because of a relatively quick reaction with oxygen to form ZnO. At high oxygen pressures this reaction is likely to occur prior to Zn atoms being able to diffuse to an equilibrium lattice site position. When oxygen deficiency becomes too large

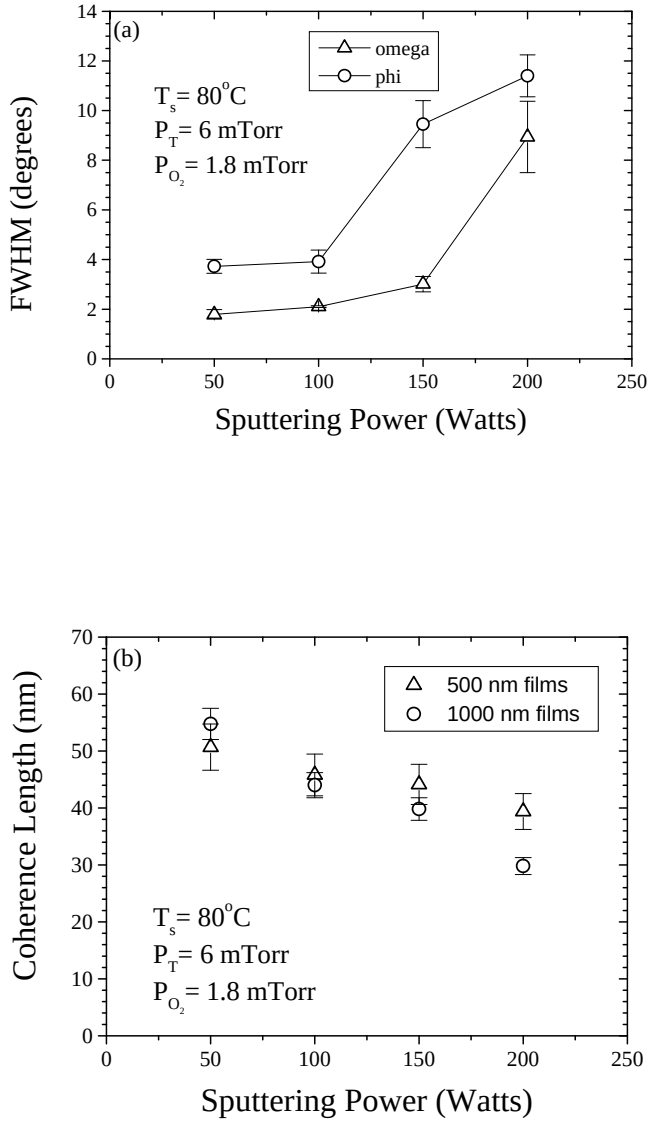

Figure 3-5 Sputtering power dependence of x-ray diffraction rocking curve (ω_{002}) and ϕ-scan ($\phi_{1\text{-}101}$) peak widths (a) and coherence length (b) for ZnO films grown in 6 mTorr with 30% O_2 on unheated sapphire substrates.

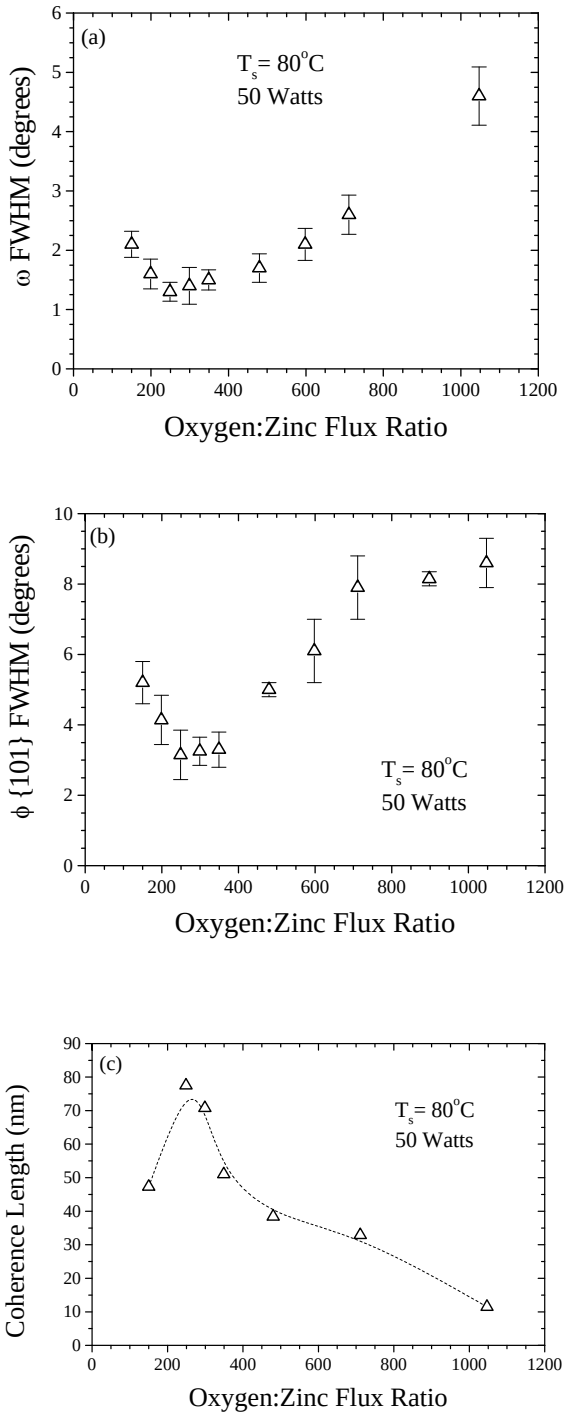

Figure 3-6 Oxygen:zinc flux ratio dependence of (002) x-ray rocking curve (a), $\{1\bar{1}01\}$ ϕ-scan (b) peak widths (FWHM), and coherence length (c) for ZnO films deposited on unheated sapphire substrates.

there is not enough oxygen present in the growth atmosphere to react with Zn adatoms that have reached lattice site positions. Under these conditions, the crystal perfection will also suffer as a result of the non-stoichiometric films.

By controlling the growth conditions it was possible to achieve epitaxial films over a broad range of growth parameters. The results of the investigation into ZnO growth indicated that it was possible to optimize the growth parameters in order to maximize crystal perfection, surface morphology, and coherence length. For our custom built sputtering chamber the results suggested that optimized films could be grown at T_S~200-300^{o}C, a target power of 50 W, and an oxygen content of ~25%.

3.3 ZnO:Al Growth and Characterization

To investigate the range of electrical and optical properties that were achievable in zinc oxide based films using our sputtering chamber a series of ZnO:Al films were grown at various oxygen partial pressures. The oxygen atmosphere during growth is an important parameter determining whether aluminum atoms are able to occupy substitutional sites and become active donors. Oxygen deficiency is also linked to conductivity in pure ZnO, as it has been suggested that oxygen vacancies themselves act as a shallow donor in ZnO.[10] The oxygen partial pressure during growth may also affect the ability of hydrogen to act as a shallow donor in ZnO, which offers an additional or alternative explanation.[11-13] Therefore, oxygen content during growth was used as a means to produce a series of films with varying carrier concentrations. The films in this study were sputtered from a zinc target doped with 2 weight percent aluminum; the

oxygen partial pressure was varied from 7 x 10^{-4} Torr to 1.3 x 10^{-3} Torr, the argon partial pressure was 4 x 10^{-3} Torr, T_S = 250^{o}C, and the substrate power was 50 W.

The oxygen content had a dramatic influence on the optical transmission spectra as shown in figure 3-7. The plot shows data for the films deposited with 0.7 mTorr (n=3.53x10^{20} cm^{-3}), and 1.1 mTorr (n=3.43x10^{18} cm^{-3}) oxygen. The oxygen partial pressure during growth clearly had a significant effect on the carrier concentration; a 57% increase in the partial pressure produced a two orders of magnitude decrease in the carrier concentration. A likely cause for the dramatic effect of oxygen partial pressure on the carrier concentration in ZnO:Al is an increase in donor activation energy for the aluminum atoms as the oxygen content in the film increases.

Two main features are evident in figure 3-7; first there is a shift of the fundamental absorption edge in the wavelength range 350-400 nm, and second there is dramatic difference in the free carrier absorption and reflection above a wavelength of 1500 nm in the near infrared region. The shift of the band gap to higher energies (a blue shift of ΔE_g^{BM}) is explained by the Burstein-Moss effect,[14] where free electrons occupy the bottom of the conduction band and therefore those levels are no longer available to except electrons promoted from the valance band (see figure 3-8). By this mechanism the energy necessary to promote an electron from the valence to the conduction band is increased and the transmission window is widened.

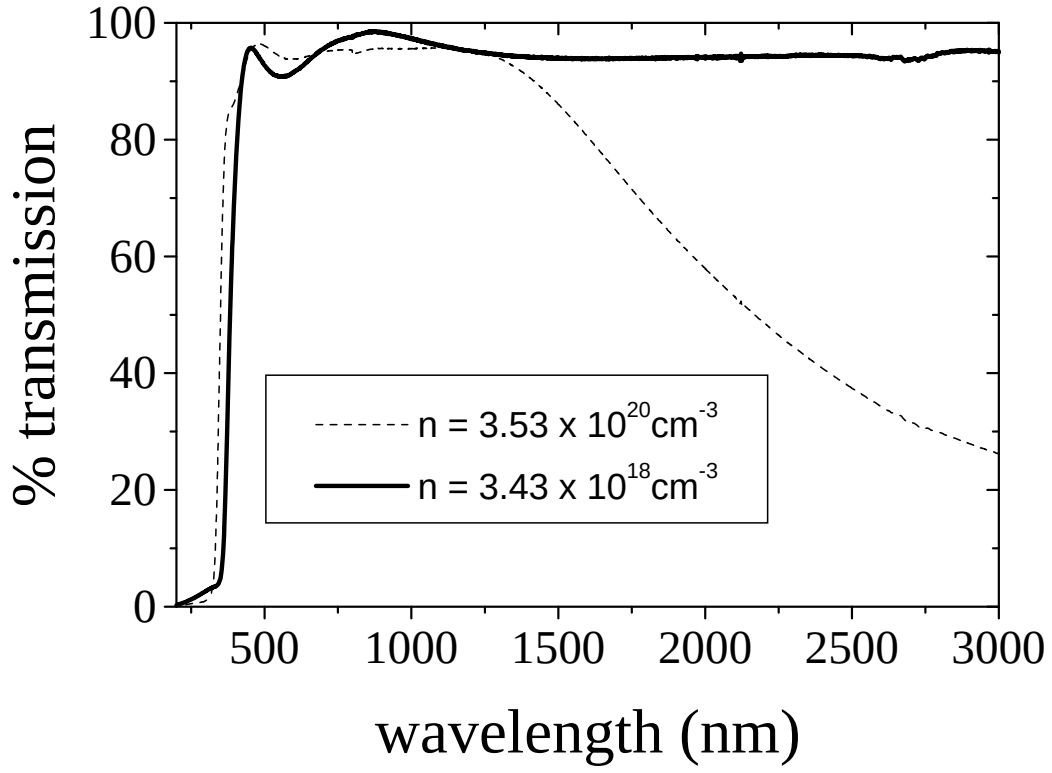

Figure 3-7 Optical transmission spectra of ZnO:Al films grown at 0.7 mTorr ($n=3.53x10^{20}$ cm^{-3}), and 1.1 mTorr ($n=3.43x10^{18}$ cm^{-3}) oxygen.

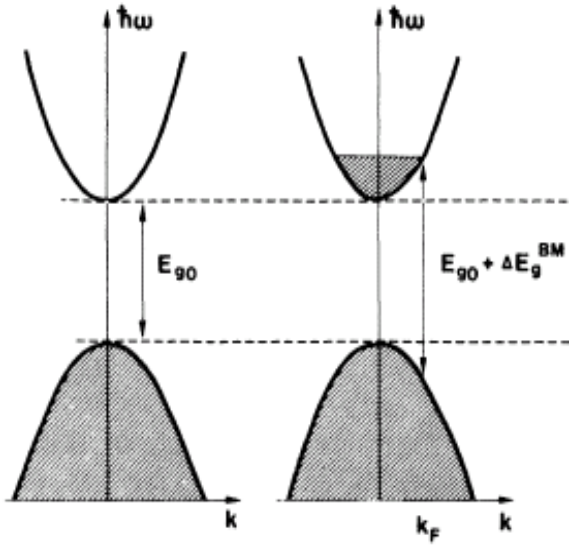

Figure 3-8 Schematic diagram of the Burstein-Moss effect.[10] The fundamental band gap (E_{g0}) is increased by an amount ΔE_g^{BM} as a result of conduction band filling by the free electron gas.

The increase of the band gap as a result of the Burstein-Moss shift is given by:[10]

$$\Delta E_g^{BM} = \frac{\hbar^2 k_F^2}{2}\left(\frac{1}{m_e}+\frac{1}{m_h}\right) \qquad \text{Equation 3-3}$$

Where k_F is the Fermi wave vector, m_e is the electron effective mass, and m_h is the hole effective mass. The difference in the higher wavelength (>1400 nm) behavior can be explained by a combination of free carrier absorption and reflection. The results in figure 3-7 agree with the theoretical results reported by Coutts et. al., who predicted minimal reflectance and absorptance at 2400 nm for a carrier concentration of 5 x 10^{18} cm^{-3}, and ~80% reflectance at 2400 nm for a carrier concentration of 5 x 10^{20} cm^{-3}. In a degenerate semiconductor the conduction electrons can be roughly modeled as a free electron gas. This free elecron model (Drude theory) leads to a quantity known as the plasma frequency (f_p), which is the frequency of incident electromagnetic radiation for which the free electron gas perfectly resonates. As a result, there is an absorption band around this frequency for which the electron gas absorbs the incident electromagnetic radiation. The plasma frequency is given by:[15]

$$f_p = \frac{1}{2\pi}\left(\frac{ne^2}{\varepsilon_0 m}\right)^{1/2} \qquad \text{Equation 3-4}$$

Where n is the electron density, e is the charge on an electron, ε_0 is the permittivity of vacuum, and m is the mass of an electron. Obviously this model does not take into account the fact that the electrons are confined within a crystal, and treats them simply as a free electron gas. Nonetheless, if the carrier concentrations found using Hall effect

measurements are used in equation 3-4, and the plasma frequency is converted to a threshold wavelength using $\lambda = c / f_p$ the results agree quite well with the transmission data in figure 3-7. A carrier concentration of 3.53 x 10^{20} cm^{-3} gives a threshold wavelength of ~1780 nm, clearly in the region where the transmission is compromised. For a carrier concentration of 3.43 x 10^{18} cm^{-3} the threshold wavelength is calculated to be 18,053 nm, which is consistent with the strong transmission seen in this study up to 3000nm. Above the threshold wavelength, the electron gas is out of phase with the incident electric field and electromagnetic radiation is reflected. Below the threshold wavelength the electron gas lags behind the electric field and electromagnetic radiation is transmitted up until the band gap wavelength is reached.

As mentioned previously, the measured optical band gap increases with carrier concentration as a result of the Burstein-Moss effect. Equation 3-3 was used to model this effect with the quantity in parentheses being equal to the inverse of the reduced effective mass ($1/m_r^*$). Since the Fermi wave vector is given by $k_F = (3\pi^2 n)^{1/3}$, assuming parabolic energy bands and a spherical Fermi surface,[16] it was possible to calculate the reduced effective mass (m_r^*), and fundamental band gap (E_{g0}) by plotting the optical band gap versus the carrier concentration raised to the 2/3rds power based on the equation:

$$E_g - E_C = \frac{\hbar^2 (3\pi^2 n)^{\frac{2}{3}}}{2m_r^*} \qquad \text{Equation 3-5}$$

The plot is shown in figure 3-9. The slope of the graph allowed the determination of m_r^*, and the y-intercept gave E_{g0}. This analysis gave a room temperature, fundamental band gap, E_{g0} = 3.28 eV which compares to reported values of 3.38 eV for stoichiometric ZnO.[10] The reduced effective mass calculated from this analysis was $0.61m_e$, which does not agree very well with the published data for ZnO that yields a reduced effective mass of 0.21 m_e.[17] An explanation for the discrepancy is offered in the work of Sernelius[10,18] and Hamberg,[19] where they explain the need to account for electron-electron, electron-impurity, and the polar nature of ZnO when investigating the effect of free carriers on the band gap of a semiconductor. These many body interactions can distort the band structure of the material around the center of the Brillouin zone, and therefore influence the energy necessary for band-to-band transitions to occur. However, Coutts[16] suggests that at carrier concentrations < $3x10^{20}$ cm^{-3} that electron-electron interactions should be minimal. With this in mind, the data were used less as a means to calculate absolute values of the reduced effective mass and more as a way to investigate the effect on the reduced effective mass of doping ZnO with impurities such as magnesium.

Perhaps the most dramatic effect the oxygen content during growth had on the ZnO:Al films was in determining the electrical properties. Figure 3-10 shows the influence oxygen content had on resistivity, carrier concentration, and mobility. The resistivity changed over four orders of magnitude with lower oxygen contents giving lower resistivities. This trend can be understood by looking at the changes in the carrier concentration and the mobility, both of which increase with decreasing oxygen content.

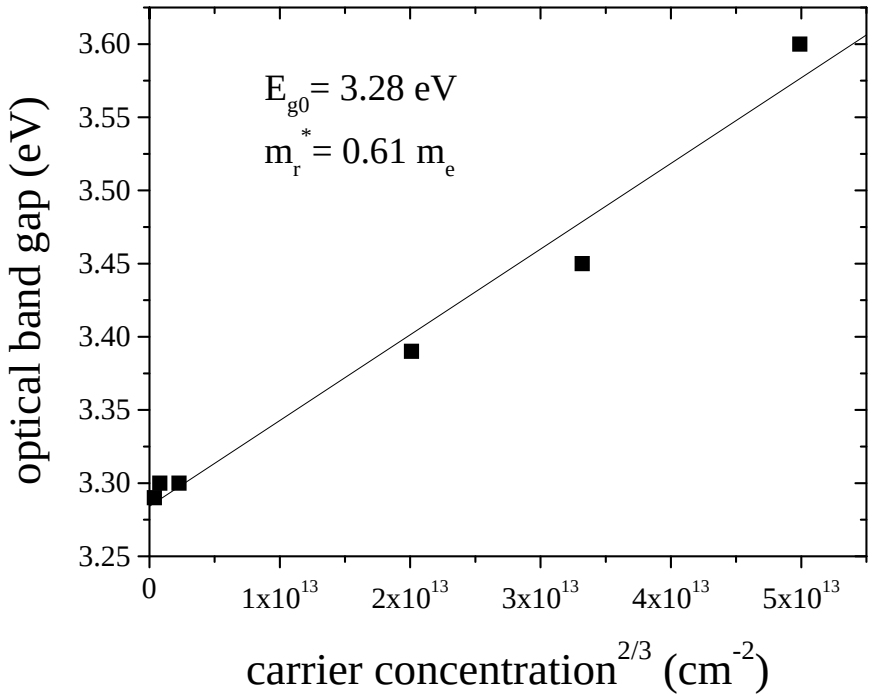

Figure 3-9 Plot demonstrating the Burstein-Moss effect for ZnO:Al (2 wt%) films grown at various oxygen partial pressures. The reduced effective mass (m_r^*) is determined from the slope, and the fundamental band gap (E_{g0}) is found from the y-intercept.

The increasing carrier concentration with lower oxygen can be explained by growth conditions that allow a large percentage of aluminum atoms to reach zinc substitutional positions where they can act as donors. At higher oxygen partial pressures it is likely that many of the aluminum atoms are oxidized to form aluminates or incorporated into the film at positions where they cannot donate their extra electron. The defect chemistry for aluminum in ZnO was summarized by Ryoken et. al.[20] with the following reactions:

$$
\begin{aligned}
&Al_2O_3 \rightarrow 2Al_{Zn}^{\bullet} + 2O_O + 2e^{'} + \frac{1}{2}O_2 \\
&Al_2O_3 \rightarrow 2Al_{Zn}^{\bullet} + 2O_O + O_i^{''} \\
&Al_2O_3 \rightarrow 2Al_{Zn}^{\bullet} + 3O_O + V_{Zn}^{''} \\
&2Al_{Zn}^{\bullet} + 2O_O + 2e^{'} + \frac{1}{2}O_2 \rightarrow Al_2O_3
\end{aligned}
\qquad \text{Equation 3-6}
$$

The first reaction explains how aluminum acts as a donor in ZnO, the second and third reactions represents possible compensation reactions that serve to decrease the carrier concentration, and the last reaction corresponds to the formation of an aluminum oxide phase. It is thought that the first reaction is dominant under low oxygen partial pressures and that the third reaction is dominant for growths at high oxygen partial pressures. A transition from the first reaction to the third reaction as the oxygen partial pressure is raised helps explain the experimental results shown in figure 3-10.

The fact that the changes in the mobility and the carrier concentration are directly proportional indicates that these films have not reached the regime where ionized impurity scattering is dominant. The relationship in these films can be explained using a grain boundary scattering analysis. In the grain boundary scattering regime increased free carriers serve to reduce the potential barrier at the grain boundary through screening,

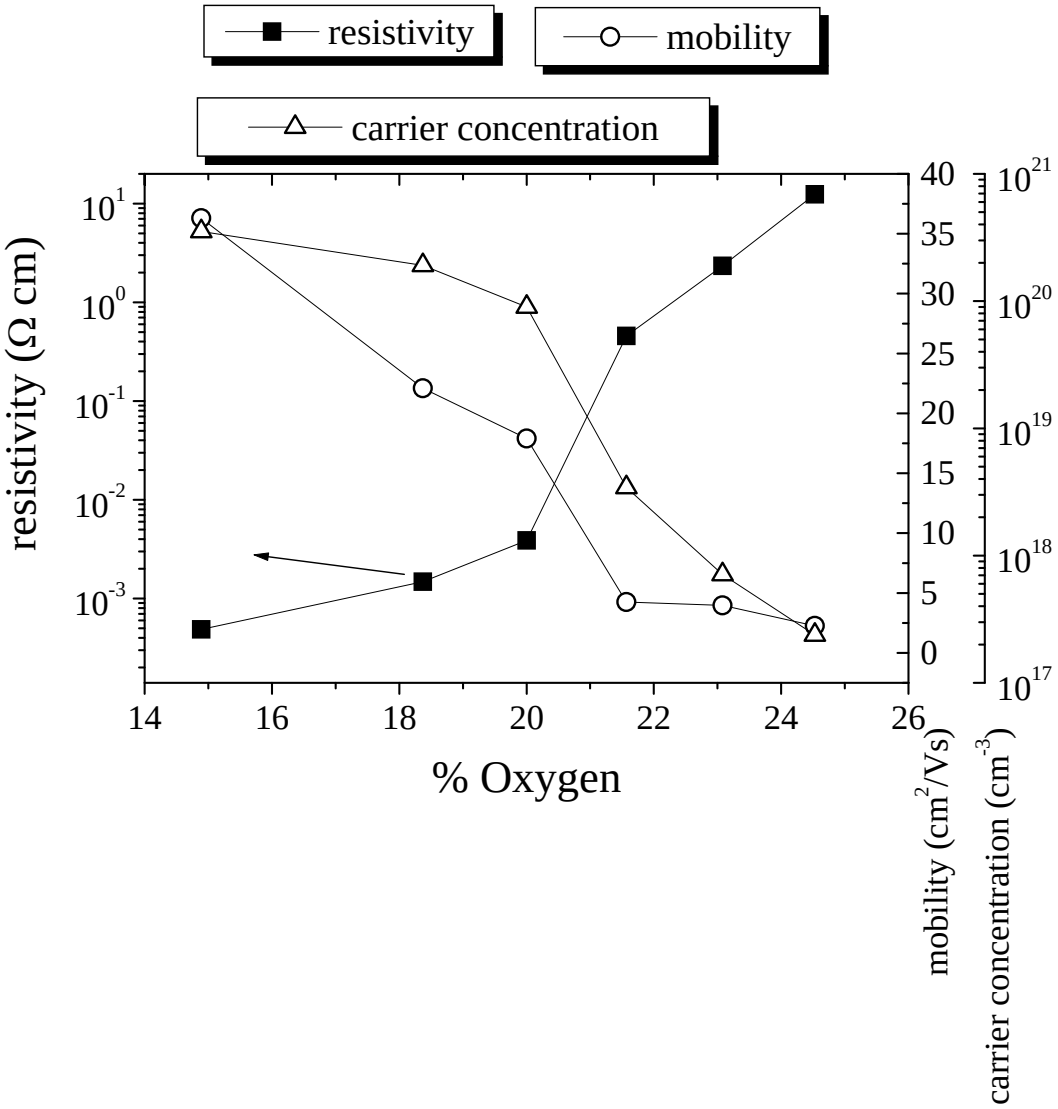

Figure 3-10 The influence of oxygen content during growth on the electrical properties of ZnO:Al (2 wt%) thin films.

and thus the mobility of the electrons is increased. The results of the ZnO study presented in section 3.2 suggest that to achieve the best overall crystal quality the oxygen content during growth should be ~25%. However, it was shown that for doped ZnO:Al films it was necessary to grow films at much lower oxygen contents in order to achieve the desired electrical properties. The ultimate goal of high carrier concentration and optimized crystal quality requires post deposition processing as discussed in the next chapter.

Chapter 4

Annealing Studies

4.1 Introduction

Post deposition annealing changed the structural and electrical properties of ZnO, ZnMgO, and multilayer epitaxial thin films. Samples were annealed in air, hydrogen/argon mixtures, and in the presence of indium in an attempt to improve the film properties. Along with the annealing atmosphere, the annealing times and temperatures were also varied in order to assess their influence on film properties.

Annealing is used to improve the crystal structure of the film and to increase the epitaxial alignment with the substrate. The annealing process had various effects on epitaxial ZnO based films including: partially relieving the residual compressive stress,[1] increasing the grain size by reducing low angle grain boundaries, and influencing the out-of-plane (rocking curve) and in-plane (phi scans) alignment. Annealing also effected the surface morphology, which was important when considering using annealed films as buffer layers for subsequent growth. The effects of annealing conditions on elemental diffusion were a factor when considering multilayer samples.

Post deposition annealing also significantly influenced the electrical properties of the films. There are various mechanisms that explained the increase in free electrons as a result of annealing. Films that were grown with donor impurities present often experienced a large increase in free carrier concentration as a result of annealing which can be explained by activation of the electron donors. By adjusting the growth conditions

(increasing the oxygen contents), it was possible to grow films that contained donor atoms (typically aluminum) but had very poor electrical properties because the donors were inactive in the as-grown film. In these cases, annealing in a reducing atmosphere of H_2/Ar was necessary to render the aluminum as an active donor. Free carriers could also be generated in intrinsic ZnO using a reducing anneal by activating native electron donor defects in the films. As discussed in the introduction, the mechanism for this intrinsic conductivity is still a matter of debate. Post deposition annealing was also conducted in the presence of indium in an attempt to improve the electrical properties of the films. Indium has a melting temperature of 156.6^{o}C, and indium diffusion into the films was detected using SIMS.

4.2 The Effect of Air Annealing on Structural Properties

The effect of the annealing temperature in air on the structural properties of ZnO thin films was investigated. A series of ZnO samples were grown on c-plane sapphire by dc reactive magnetron sputtering at a substrate temperature of 300^{o}C, in 4 mTorr Ar, and 1 mTorr O_2. Each film was ~120 nm thick, and air anneals were performed for 2 hours at 800^{o}C, 1000^{o}C, and 1200^{o}C.

The effect of the 1000^{o}C anneal on the $\theta - 2\theta$ XRD scan is shown in figure 4-1. The shift of the $\theta - 2\theta$ peak to a higher value was determined to be a result of the relaxation of the residual compressive stress typically present in ZnO films grown on (0001) sapphire.[2] The annealed peak position of 34.46^o agreed quite well with the calculated value of 34.4^o for relaxed (002) planes in ZnO (JCPDS 80-0075). The

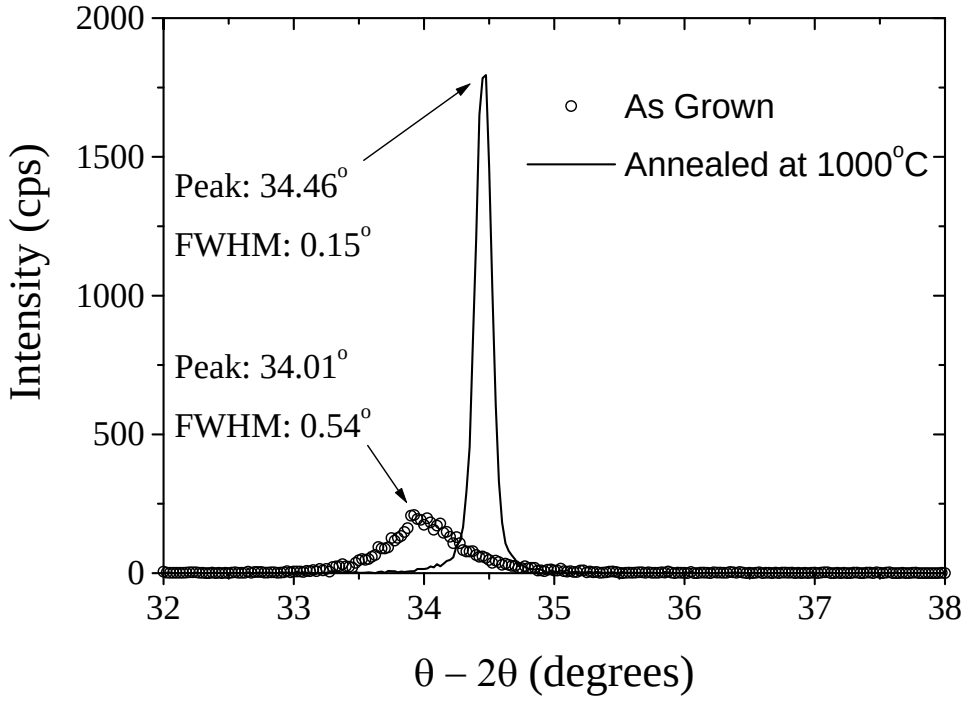

Figure 4-1 The effect of air annealing on the $\theta - 2\theta$ XRD scan of a ZnO thin film.

decrease of the $\theta - 2\theta$ FWHM was consistent with an increase in the coherence length resulting from a reduction in the number of low angle grain boundaries in the epitaxial films. Applying the Scherrer formula to the data for the 1000°C film gave a coherence length of 16 nm for the as-grown film and 57 nm for the annealed film. The $\theta - 2\theta$ peak position for the film annealed at 800°C shifted from 33.98°C to 34.44°C and the FWHM changed from 0.60°C to 0.17°C, showing similar effects as at 1000°C. For the 1200°C sample, no XRD signal could be found, even though there was still a film there as measured by the profilometer. The conclusion was that the film had recrystallized and no longer had (002) preferred orientation.

The rocking curves and the phi scans for the ZnO sample annealed at 1000°C are shown in figure 4-2(a). The increase in the intensity and decrease in the FWHM (from 1.82° to 0.59°) of the rocking curve indicated an improvement in the out of plane alignment of the ZnO (002) planes relative to the basal plane of the substrate. The rocking curve of the 800°C sample changed from 2.52° to 0.60°, and the (002) rocking curve for the 1200°C sample could not be measured. The $\{1\bar{1}01\}$ phi scans for the 800°C and 1000°C samples showed six-fold symmetry consistent with the hexagonal wurtzite structure expected for ZnO. A detailed scan of one of the six phi peaks is shown in figure 4-2(b) for the 1000°C sample before and after annealing. The FWHM of the phi scan changed from 1.82° to 0.59° as a result of the annealing process. This change in the phi scan indicated that the in-plane alignment of the film had improved, the epitaxial

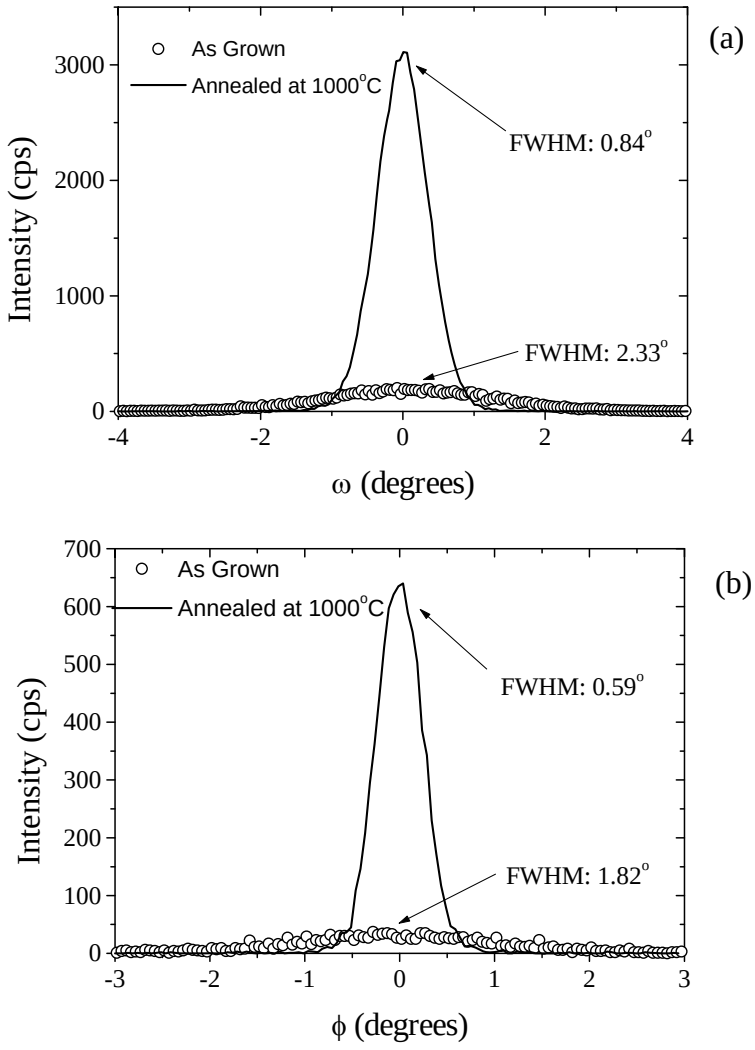

Figure 4-2 XRD rocking curve (a) and phi (b) scans for ZnO samples annealed at 1000°C in air.

relationship between the ZnO domains and the sapphire substrate had become more perfect as a result of the post deposition anneal. The 800^{o}C sample showed a phi peak FWHM change from 1.34^{o} to 0.62^{o} with annealing, indicating a similar improvement of the in-plane allignment. Once again, no phi scan was obtained from the 1200^{o}C sample after annealing.

AFM images (shown in figure 4-3) were obtained to investigate the effect of air annealing on the surface morphology of ZnO films. The scans were all 20 μm x 20 μm in size, the height scale for the as-grown sample is 20 nm and for each annealed sample the height scale is 50 nm. In each case the root-mean-square surface roughness of the annealed sample increased relative to the as-grown value of 1.59 nm. The 800^{o}C sample still had a very smooth surface with an rms roughness of 1.93 nm. The 1000^{o}C film had a considerably rougher surface (rms: 6.94 nm), and, as can be seen by the enlarged section of the image, there was hexagonal faceting apparent on the surface of the film. The hexagonal faceting is consistent with the wurtzite structure of (002) oriented ZnO. The 1200^{o}C film surface was extremely rough (rms: 15.7) and showed no discernable faceting. The AFM information is consistent with the XRD data for the 1200^{o}C film both of which indicated that the ZnO had recrystalized into a film without preferred orientation.

Based on the experimental results it was concluded that annealing ZnO films in air could dramatically influence both the crystal quality and the surface morphology. For the temperatures investigated it was concluded that an 800^{o}C air anneal of ZnO films

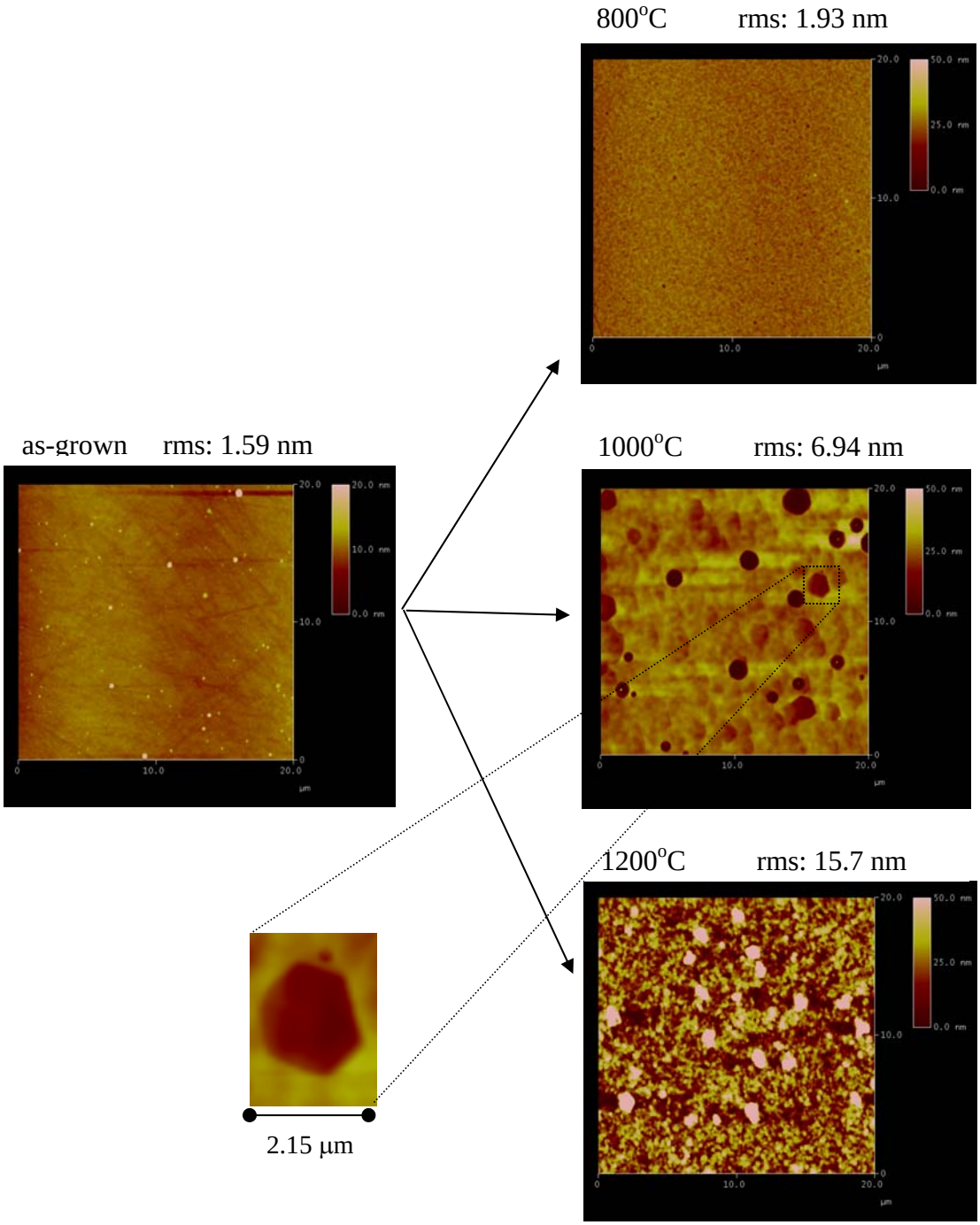

Figure 4-3 The effect of air annealing temperature on the rms roughness of ZnO thin films. Note: Height scale for as-grown is 20 nm and for annealed it is 50 nm.

could provide improvement in the crystal quality while maintaining a smooth surface. This processing technique can be used to prepare high quality ZnO buffer layers for subsequent film growth, or to improve the crystal quality of as-grown films in an attempt to improve free carrier mobility. The use of a ZnO buffer layer on c-plane sapphire is an attractive option in light of the fact that ZnO single crystal substrates are relatively expensive ($330,10 mm x 10 mm, c-plane, MTI Corporation).

4.3 The Effect of Annealing Temperature on Electrical Properties

Thin films of ZnO, ZnMgO:Al, and a ZnO/ZnMgO:Al multilayer were grown at 300^{o}C on c-plane sapphire substrates. The argon pressure was 4.5 mTorr, the oxygen pressure was 1.5 mTorr, and the film thickness ranged from 140 nm to 180 nm. The ZnO film was grown from a zinc target at 50 W sputtering power, the ZnMgO:Al film was co-sputtered from a Zn (80 at%)/Mg (20 at%) alloy target at 50 W and an aluminum target at 150 W (SIMS was used to determine that this gave an Al concentration of ~6.5 at%). The multilayer was designed to consist of alternating 5 nm layers of ZnO and ZnMgO:Al with a total of 15 periods (the multilayer deposition started with a ZnO layer).

The as-grown films were characterized by XRD and then cut into four square pieces. None of the as-grown films had a conductivity that could be measured with the BioRad Hall system. The pieces were annealed at 300^{o}C, 400^{o}C, and 500^{o}C for 4 hours. Films were only annealed up to 500^{o}C because it was found that under these reducing conditions the films completely sublimed at temperatures of 600^{o}C. The films were annealed inside an alumina tube in the presence of a 70% argon, 30% hydrogen mixture

that flowed over the samples at a rate of 70 sccm. The films were held in an alumina boat containing indium metal and covered with a mullite boat.

The effects of the reducing anneal on the electrical properties are shown in figure 4-4. For all samples, the resistivity (figure 4-4(a)) decreased as the annealing temperature increased. An increase in annealing temperature increased the carrier concentration (figure 4-4(b)) for all samples, and the ZnMgO:Al sample had the highest carrier concentration for all annealing temperatures. The carrier concentration in the multilayer increased over three orders of magnitude as the annealing temperature was increased, and for the 500^{o}C samples the average carrier concentration in the multilayer was higher than in the ZnO sample. The increase in free carrier concentration of the doped ZnMgO:Al and the multilayer films as a result of annealing in a reducing atmosphere can be explained by the following defect reaction:

$$Al_2O_3 \rightarrow 2Al_{Zn}^{\bullet} + 2O_O + 2e^{'} + \frac{1}{2}O_2 \qquad \text{Equation 4-1}$$

Under low oxygen partial pressures the defect reaction in equation 4-1 is thought to be energetically favorable, and the formation of defects that compensate free carrier generation are suppressed. The ability of a reducing atmosphere to influence the defect chemistry of ZnO based films is supported by the relatively high diffusion coefficient of oxygen in aluminum doped ZnO of ~ 1 x 10^{-13} cm^2/s^3 for temperatures of ~ 1000^{o}C. In the non-intentionally doped ZnO film free carrier generation may be from a combination of several sources including native charged defects such as oxygen vacancies[4] and zinc interstitials, the diffusion of aluminum from the substrate into the film,[3] and the presence of hydrogen as a shallow donor.[5,6]

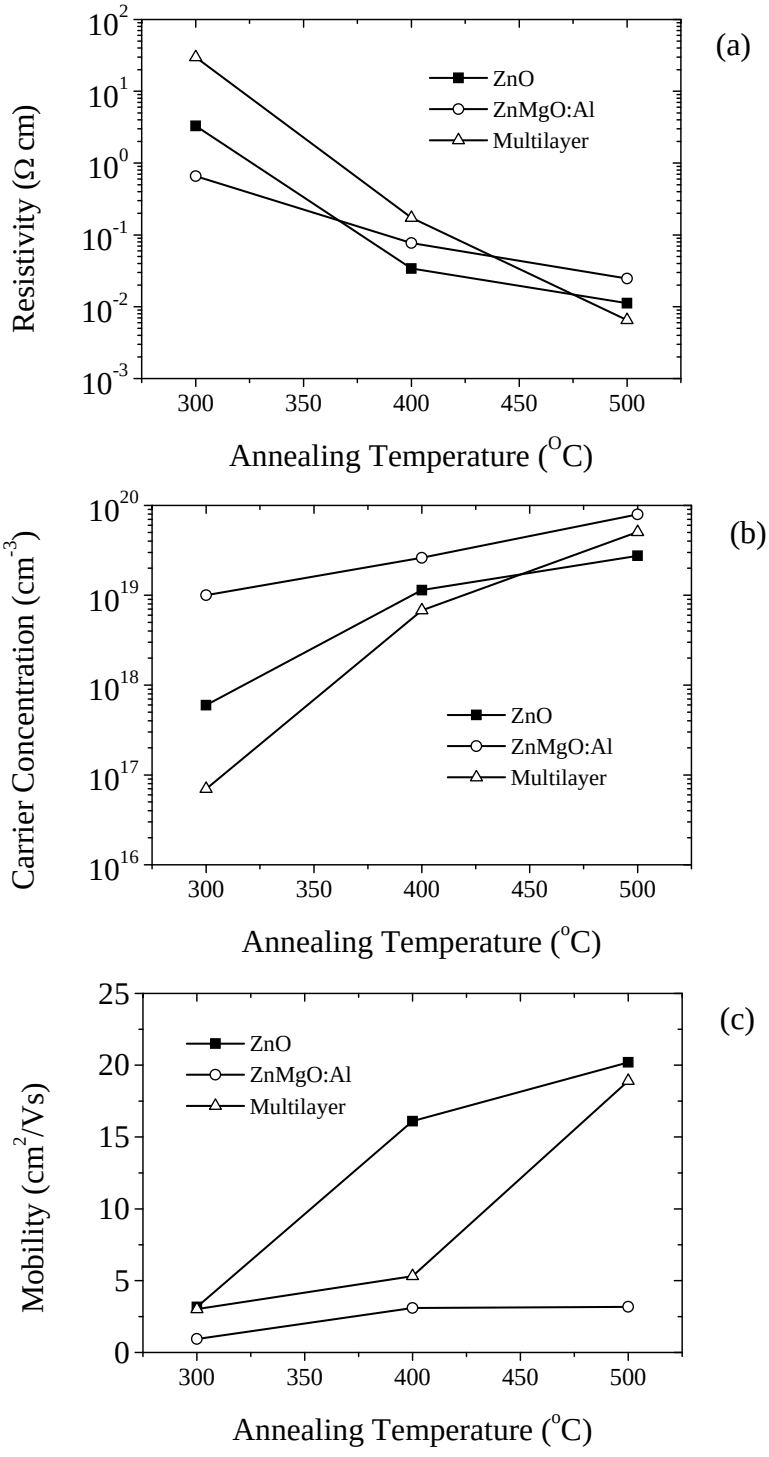

Figure 4-4 The effect of annealing temperature on the electrical properties of ZnO, ZnMgO:Al, and multilayer samples.

Perhaps the most interesting results were obtained for the carrier mobility (figure 4-4(c)). The ZnMgO:Al sample had extremely low mobility compared to ZnO:Al samples with similar carrier concentrations. For example, a ZnO:Al (2 wt%) grown under similar conditions had a carrier concentration of 9×10^{19} cm^{-3} and a mobility of 17.9 cm^2/Vs. The mobility limiting scattering mechanism for the ZnMgO:Al was therefore unlikely to be grain boundaries because at the range of carrier concentrations present the grain boundary energy barrier is expected to be lower than would produce a mobility of ~ 3 cm^2/Vs. It was also unlikely that ionized impurity scattering was the dominant scattering mechanism because the carrier concentration was below the threshold level (~1×10^{20} cm^{-3})[7] where ionized impurity scattering limits the mobility. The most likely explanation for the low mobility in the ZnMgO:Al films was a combination of neutral impurity scattering from Mg atoms, alloy disorder scattering, and scattering from Mg and Al complexes formed in the films. These issues are treated quantitatively in chapter 5 whenZnMgO is discussed. The electrical data for the ZnO films was consistent with grain boundary limited mobility, where an increase in the carrier concentration leads to an increase in the carrier mobility.

The mobility results for the multilayer samples were not a simple average of the properties of the individual layers. In the 400^oC annealed samples the average mobility seemed to be dominated by the behavior of the ZnMgO:Al layers, and in the 500^oC annealed samples the average mobility seemed to be dominated by the high mobility ZnO layers. The combination of high average carrier concentration and high average mobility in the multilayer annealed at 500^oC produced a resistivity lower than that achieved by

either of the monolithic films grown for the constituent layers. One possible explanation for the results was diffusion between the layers at 500°C leading to a redistribution of the Mg and Al dopants, which would change the composition of the original low mobility ZnMgO:Al layers. The effects of annealing on diffusion will be discussed later in this chapter.

4.4 The Effect of Annealing Time on Electrical Properties

As mentioned previously, films were annealed in the presence of indium in an attempt to improve their electrical properties. Figure 4-5 shows the effect of the In anneal time *t*, at 415°C in 20 sccm hydrogen, 50 sccm argon, on the resistivity of a pure ZnO, ZnO:Al (4.8 at % Al), and a $Zn_{0.9}Mg_{0.1}O$:Al (2.2 at % Al) film. The films were first annealed for 4 hours at 415°C in 20 sccm hydrogen, 50 sccm argon without indium present. The data points at $t = 0$ represent the resistivity of these In-free films. As is typically observed in ZnO films, the insulating as-grown films became conducting after the indium-free anneal; this has been attributed to the formation of intrinsic defects (oxygen vacancies/hydrogen) during the reducing anneal.[8,9] The ρ value decreased rapidly within the first ≈ 5h of In annealing, after which it decreased more gradually. The substantial decrease in ρ indicates the effectiveness of the In doping, particularly for undoped ZnO and ZnMgO:Al. For all samples, the carrier concentration and mobility changes were directly related, that is they increased and decreased together. This is consistent with a grain boundary or neutral impurity scattering limited mobility

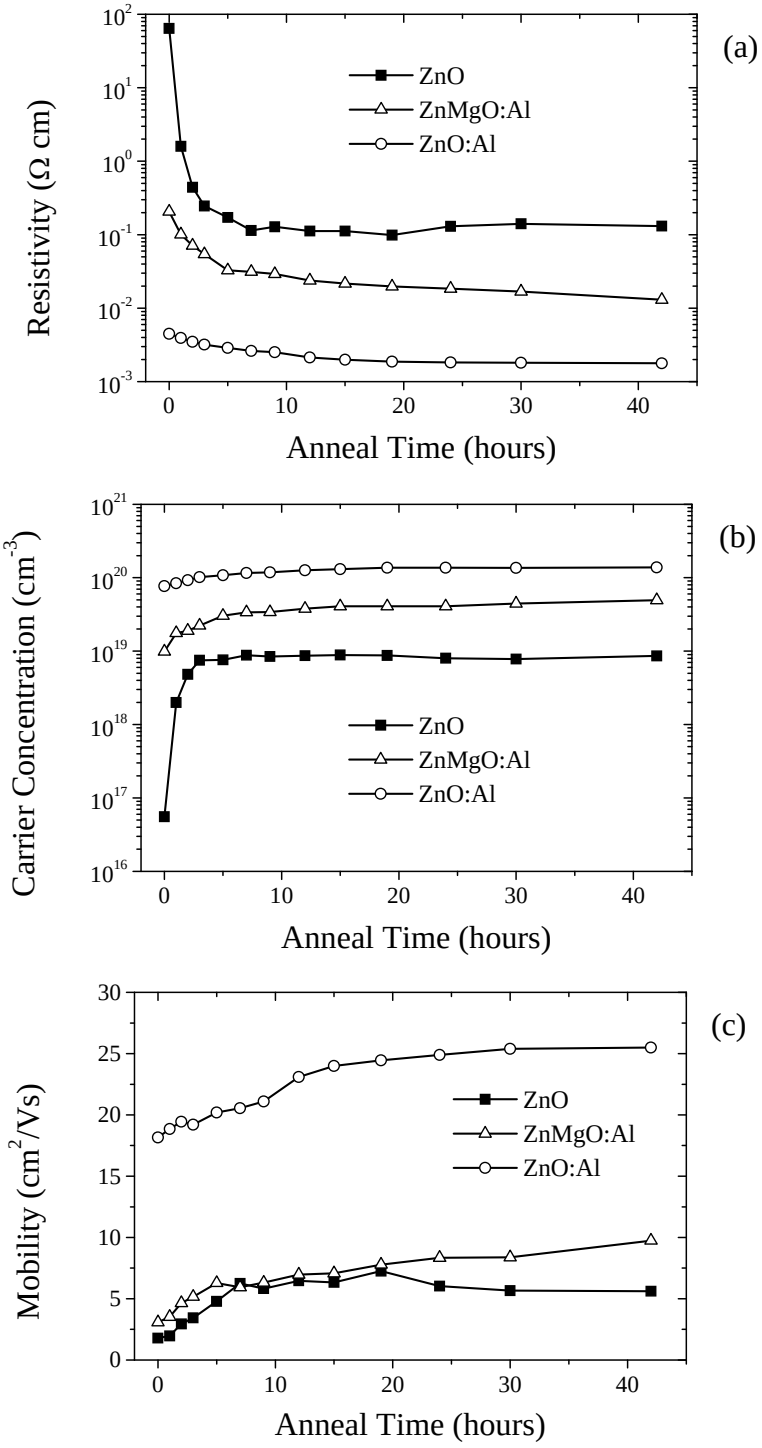

Figure 4-5 The effect of annealing time on the electrical properties of ZnO, ZnMgO:Al, and ZnO:Al thin films.

mechanism, where higher carrier concentrations reduce the energy barrier for electron motion and thus the mobility is increased.

Figure 4-6 shows the time-of-flight secondary ion mass spectrometry (SIMS) depth profiles taken after 42 hours of annealing in the presence of indium. The In concentration decreased rapidly with increasing depth within the first 50 nm, followed by a more gradual decrease. Note that the background In signal for an undoped sample was < 10 counts, such that even the lowest In level in figure 4-6 was well above the background. By comparison with an In-doped ZnMgO standard, obtained by sputtering from a ZnMgIn target, the reasonably constant In concentration throughout most of the film was $\approx 9 \times 10^{19}$ cm^{-3}. The In concentration profile in figure 4-6, combined with the decrease in ρ with increasing time in figure 4-5, is consistent with solid-state diffusion of In into the films from a vapor source.

4.5 The Effect of Annealing Temperature on Multilayer Films

The effect of annealing temperature on the stability of multilayer structures was investigated using time-of-flight SIMS depth profiling. A multilayer sample was grown at 300^{o}C in 4.5 mTorr Ar, and 1.5 mTorr O_2. A 20 nm ZnO layer was deposited first at a Zn target power of 50 Watts, followed by a 5 nm layer of $Zn_{0.8}Mg_{0.2}O$:Al (6.5 at% Al) deposited with a ZnMg target power of 50 Watts and an Al target power of 150 Watts. A total of six periods of the multilayer were deposited. A SIMS depth profile was taken of the as-grown sample (see figure 4-7) and then the multilayer was annealed for 4 hours in

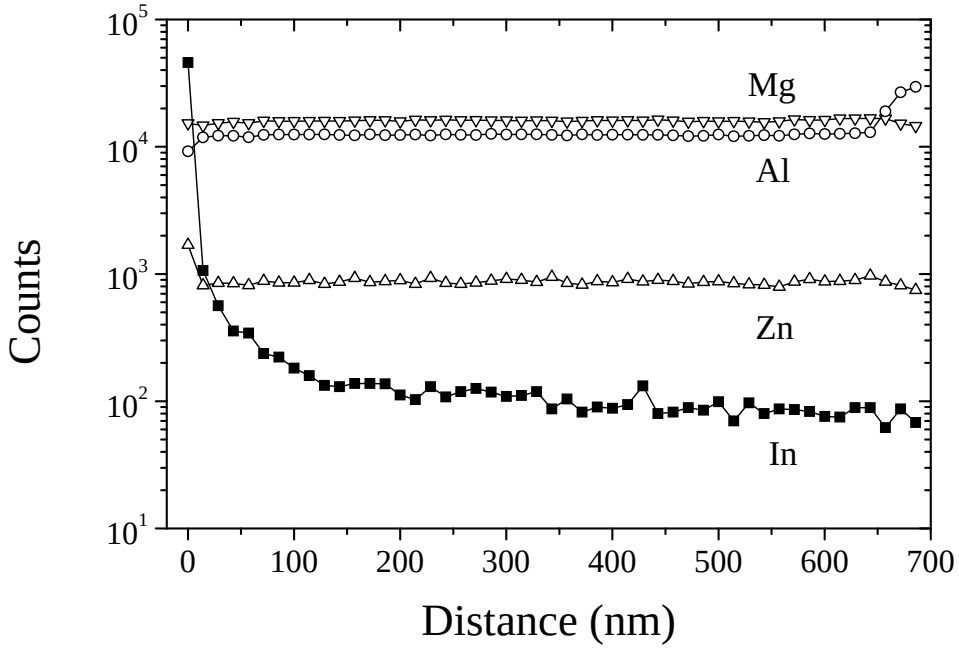

Figure 4-6 Depth profile of the SIMS In, Al, Zn, and Mg peaks from an In annealed $Zn_{0.9}Mg_{0.1}O$:Al (2.2 at % Al) film.

As Grown:

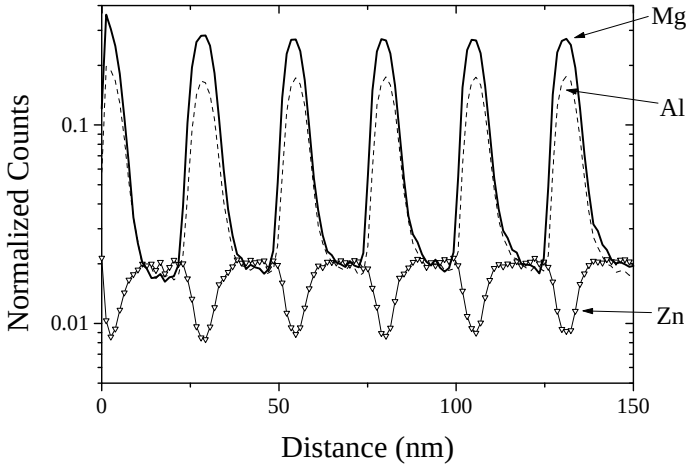

After 350°C Anneal:

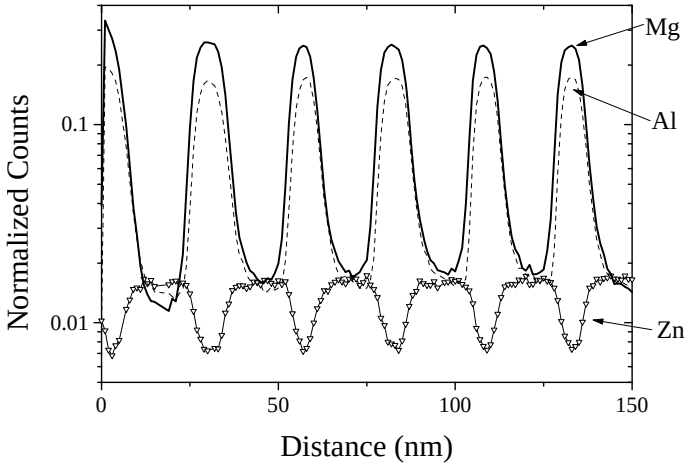

After 500°C Anneal:

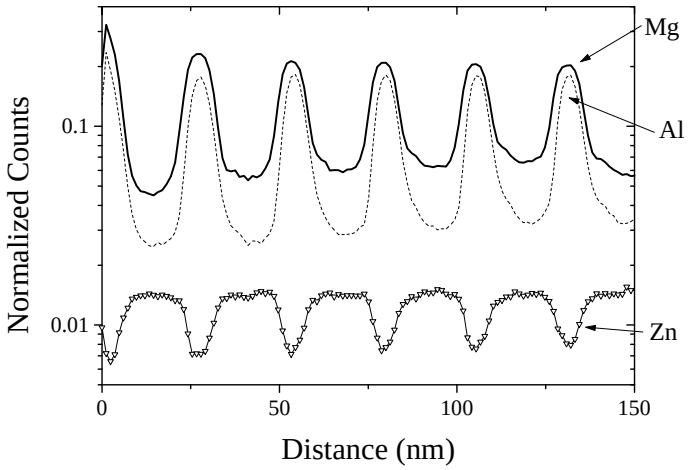

Figure 4-7 The effect of annealing temperature on the SIMS depth profile of a multilayer sample.

the presence of indium at 350^{o}C in a 70% Ar, 30% H_2 atmosphere flowing at 70 sccm. A second SIMS depth profile was taken and then the sample was annealed again at 500^{o}C under the same conditions, after which a third SIMS depth profile was taken.

The SIMS depth profiles showed no discernable difference between the as-grown sample and the sample after the 350^{o}C anneal. Therefore, annealing at 350^{o}C could be used to influence the electrical properties of a multilayer film without causing appreciable diffusion to occur between the layers. However, after the 500^{o}C anneal the SIMS depth profile showed substantial diffusion of the Mg and Al between the layers. Subsequent experiments performed on these samples, by Blake Stevens, determined that the diffusional broadening of the Mg peak was on the order of 0.65 nm. As a result of this broadening, a mechanism such as modulation doping that relies on sharp interfaces between the layers would be lost after a 500^{o}C anneal. The SIMS results in figure 4-7 helped explain the electrical data shown in figure 4-4. Diffusion of electrically inactive Al atoms out of the ZnMgO:Al layer and into the ZnO layer where they could become donors may be the reason for the higher average carrier concentration after the 500^{o}C anneal. The redistribution of Mg also helped explain the increase in the average mobility, by reducing the neutral impurity and alloy disorder scattering in the ZnMgO:Al layers.

Chapter 5

ZnMgO:(Al,In) Growth and Characterization

5.1 Introduction

Transparent conducting oxides are characterized by a unique combination of low electrical resistivity and high optical transparency. ZnO is one of a select group of materials currently being considered to compete with tin doped indium oxide and tin oxide for applications including flat panel displays, solar cells, and energy efficient windows.[1] Intrinsic ZnO has a room temperature band gap E_G of 3.4 eV, relatively large among transparent conducting oxide materials, and with heavy doping (electron concentrations above ~10^{20} /cm^3) E_G increases further[2] to ≈ 3.64 eV due to the Burstein-Moss shift.[3]

There is also interest in conducting layers exhibiting optical transparency into the ultraviolet range for applications such as solar cells.[4,5] An additional application for large E_G conducting oxides is in proposed modulation doped transparent conducting oxide hetero-structures designed to increase electron mobilities.[6,7] In these structures, large E_G layers with high doping concentrations are needed to donate electrons to intrinsic zinc oxide layers. It has been reported that ZnMgO solid solution thin films can be grown epitaxially, extending E_G values into the ultra-violet range: 3.99 eV in films with 33 mol percent Mg.[8] However, the work reported on donor doping of ZnMgO films is limited,[9] so the range of properties in large-E_G TCO's that can be produced is not known.

In this chapter we the growth and characterization of $Zn_{1-x}Mg_xO$:(Al,In) thin films on c-plane sapphire substrates by direct current reactive magnetron sputtering is reported. Sapphire is the substrate most often used to grow epitaxial ZnO films for electro-optic applications owing to its hexagonal crystal structure and low cost. Detailed characterization of the microstructure, electrical, and optical properties of the films as a function of film composition, deposition conditions, and annealing conditions are reported. The results are compared with those for doped ZnO films and discussed in terms of doping and electrical conduction models.

5.2 Experimental Procedure

$Zn_{1-x}Mg_xO$:Al films were deposited in a reactive magnetron sputtering chamber. The load-locked chamber, described in detail elsewhere,[10] was turbomolecular pumped to a base pressure of $\approx 1 \times 10^{-7}$ Torr, and contains three sputter sources, mounted at 35^o from the substrate surface normal. The target to substrate distance was ≈12 cm. The films were deposited by co-sputtering from two 5-cm-diam targets in Ar-O_2 mixtures at a total pressure P_T = 6 mTorr. One target was a 99.99% pure metallic Zn-Mg alloy with Mg contents of 5, 10, or 20 at%, sputtered at 50W power unless otherwise noted. The other target was 99.999% pure Al, sputtered at power levels from 25W to 150W yielding Al contents up to 4.5%. Unless otherwise stated, the Ar partial pressure was 4.5×10^{-3} Torr and oxygen partial pressure $P_{O_2} = 1.5 \times 10^{-3}$ Torr.

The double side polished (0001) sapphire substrates were ultrasonically cleaned for 10 minutes each in acetone then methanol and blown dry with nitrogen before being

placed in the load-lock. The sapphire substrate was clamped to a silicon wafer that was resistively heated; the temperature had previously been calibrated with a thermocouple attached to the sapphire. The substrates were heated in vacuum at 600^{o}C for 30 minutes in order to remove any residual surface contamination, and then allowed to cool to the growth temperature. Films were grown at substrate temperatures ranging from T_s = 175^{o}C to T_s = 500^{o}C. A value of 300^{o}C was used unless otherwise noted. The targets were pre-sputtered in pure argon for 15 minutes to remove surface contamination, and then oxygen was introduced and the target voltage was allowed to stabilize for an additional 15 minutes. The shutter was then removed to commence growth. The gas pressure was monitored and adjusted during growth using mass flow controllers. Film thicknesses ranged from 350 – 550 nm, and the growth rates ranged from 2.0 – 4.4 nm/min with higher magnesium content targets yielding lower rates.

In order to achieve low resistivities it was typically necessary to thermally anneal the films. The films were placed in an alumina boat inside an alumina tube furnace. A piece of 6N pure indium shot (Alfa Aesar) ~ 5mm in length was placed at the front and back end of the alumina boat, except for a few cases as noted below. A mixture of hydrogen (20 sccm) and argon (50 sccm) was bubbled through deionized water and allowed to flow over the samples. The furnace was ramped up to the anneal temperature of 415^{0}C at 40^{o}/min and held for 4 hours. The films were allowed to cool back to room temperature at 2^{o}/min under the same H_2/Ar atmosphere.

The film thickness was measured with a surface profiler (Tencor P-10) and confirmed using the interference fringes from optical transmission spectra.[11] A UV-VIS-

IR dual-beam spectrophotometer (Varian Cary 500) was used to measure the optical transmission for wavelengths from 3000 - 250 nm. Electrical resistivity, mobility, and carrier concentration were measured using the van der Pauw[12] geometry with Hall effect measurements (BioRad Hall system). Crystal quality was investigated using x-ray diffraction (Rigaku RU-200PL). Surface roughness was measured using an atomic force microscope (Digital Instruments) in contact mode.

The aluminum concentration was determined using time-of-flight secondary ion mass spectrometry (Physical Electronics). The ratio of the aluminum peak to the zinc peak was determined for each sample and calibrated using known standards.

5.3 Experimental Results

5.3.1. Growth Rate

For all the ZnMg target compositions and substrate temperature $T_S \leq 300^oC$, the growth rate decreased with increasing oxygen partial pressure due to target poisoning.[13] For example, for a $Zn_{0.8}Mg_{0.2}$ alloy target sputtered at 50 W, P_T = 6 mTorr, and T_S = 300^oC, the rate decreased from 4.7 nm/min at P_{O_2} = 0.45 mTorr to 1.0 nm/min at P_{O_2} = 3 mTorr. The sputtering rate generally decreased with increasing Mg content in the target. For example, under the same conditions as noted above but with P_{O_2} = 2 mTorr, the rate decreased from 3.6 nm/min for pure Zn to 1.5 nm/min for $Zn_{0.8}Mg_{0.2}$.

The growth rate did not vary substantially with $T_S \leq 300^oC$, but decreased with increasing T_S above this value. For example, for a $Zn_{0.9}Mg_{0.1}$ target sputtered at 50 watts in 1.5 mTorr O_2 with P_T = 6 mTorr, the rate decreased from 3.6 nm/min at 300^oC to 3.0

nm/min at 500°C. This is presumably due to desorption of Zn and/or Zn-oxygen species from the substrate surface.[14] Note that at $T_S > 300^oC$, Zn evaporation tended to reduce the growth rate more at low P_{O_2}, due to the presence of more un-oxidized Zn on the growing film surface.

5.3.2. Morphology and Crystal Structure

Figure 5-1 shows XRD results from a typical $Zn_{0.95}Mg_{0.05}O$ film as deposited and after annealing, including θ-2θ scan, omega scan, and phi scan. The results are typical of films with 5 – 20% MgO. The film was grown at $T_S = 300^oC$ in 25% oxygen with $P_T = 6$ mTorr, and then annealed in the presence of indium at 415^oC for 4 hours in a H_2/Ar atmosphere. The phi scan in figure 5-1(c) clearly indicates that the film is epitaxial with hexagonal symmetry, but the width of the peak indicates a mosaic-structure film as expected given the rather large lattice mismatch.[15] The addition of Mg to zinc oxide shortens the c-axis length[8] and thus shifts the ZnO (0002) peak position to higher angles; however, at 5%Mg the shift is very small. The as deposited 5% Mg film had a θ-2θ peak position of 34.25^o, indicating a residual in plane compressive stress of 2.1 GPa calculated using the biaxial stress model.[16] After the anneal, the ZnO (0002) peak position shifted to 34.41^o. For comparison, the ZnO (0002) peak position for annealed zinc oxide powder, 34.4^o,[16] is also shown. The shift is explained by the relief of compressive residual stress in the as-deposited film.[17] The anneal increased the grain size, as shown by a decrease in the FWHM of the θ-2θ peak from 0.48^o to 0.29^o. The increase in grain size was interpreted as a reduction in the density of low-angle grain boundaries. The anneal

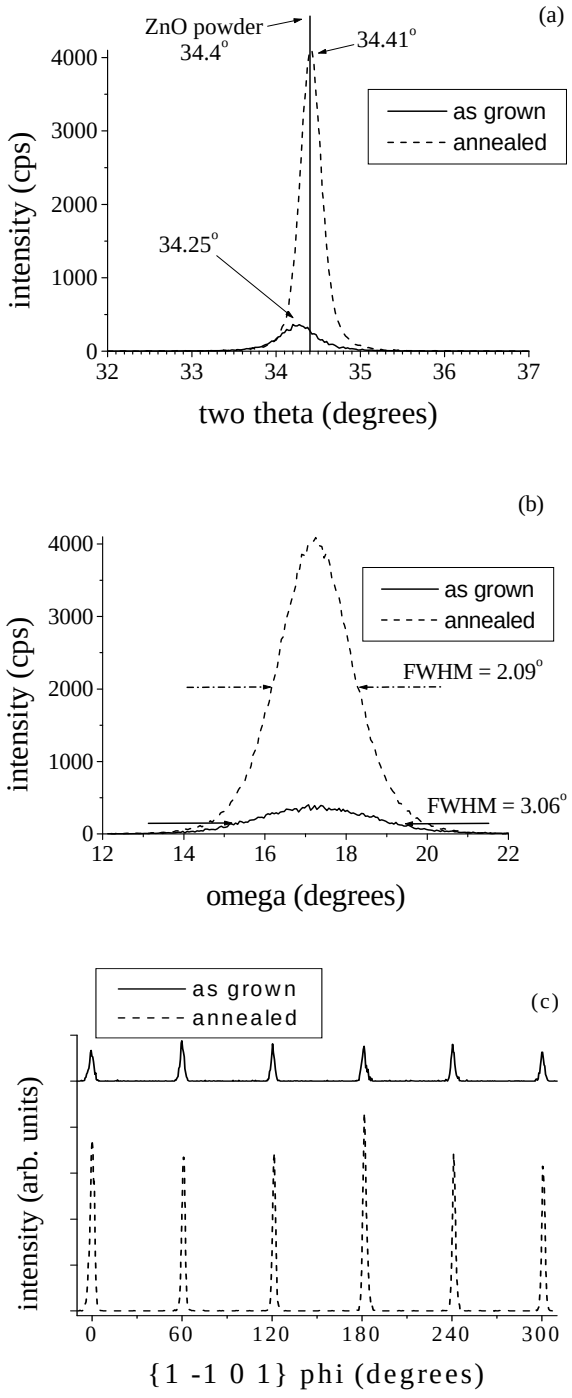

Figure 5-1 Comparisons of x-ray diffraction θ–2θ (a), omega (b), and phi (c) scans from as-grown and annealed $Zn_{0.95}Mg_{0.05}O$ films.

improved the out of plane alignment of the film – the FWHM rocking curve width decreased from 3.06° to 2.09° – however the in plane alignment was slightly deteriorated after the anneal - the FWHM phi scan width increased from 2.15° to 2.57°. The increased intensity in all scans following the anneal is a result of improved crystallinity. The effects of the anneal on residual stress, grain size, and out of plane alignment are consistent with prior results for ZnO films.[17]

The oxygen content in the sputtering gas was varied from 6.67% to 50%, P_T = 6 mTorr, for a set of $Zn_{0.8}Mg_{0.2}O$:Al (1.4 at % Al) films. The 6.67% oxygen sample was $(10\bar{1}1)$ oriented; all other films had the low energy[18] (0002) orientation, as shown in figure 5-2. The film grown at 12.5% oxygen had a θ–2θ position of 34.37° compared to 34.51° for the 25% oxygen sample, and the 50% oxygen film had a θ–2θ FWHM of 0.55° compared to 0.39° for the 25% oxygen sample. Based on this XRD data, the film grown at 25% oxygen had the least residual compressive stress and the largest grain size. The 25% oxygen films also typically showed the smoothest surfaces. Figure 5-3 shows atomic force microscope images for the 12.5%, 25%, and 50% oxygen films. The minimum root-mean-square (rms) roughness was 0.48 nm for the 25% oxygen film, substantially less than the other partial pressures.

Figure 5-4 shows the XRD results as a function of temperature for a set of $Zn_{0.9}Mg_{0.1}O$:Al (2.2 at % Al) films. The FWHM values of the omega and phi scan peaks had a minimum value for $T_S \approx 300^oC$. Varied effects of substrate temperature on crystal quality have been observed depending on the deposition technique. Results for ZnO:Al films deposited on c-plane sapphire by pulsed laser deposition[19] show an improvement in

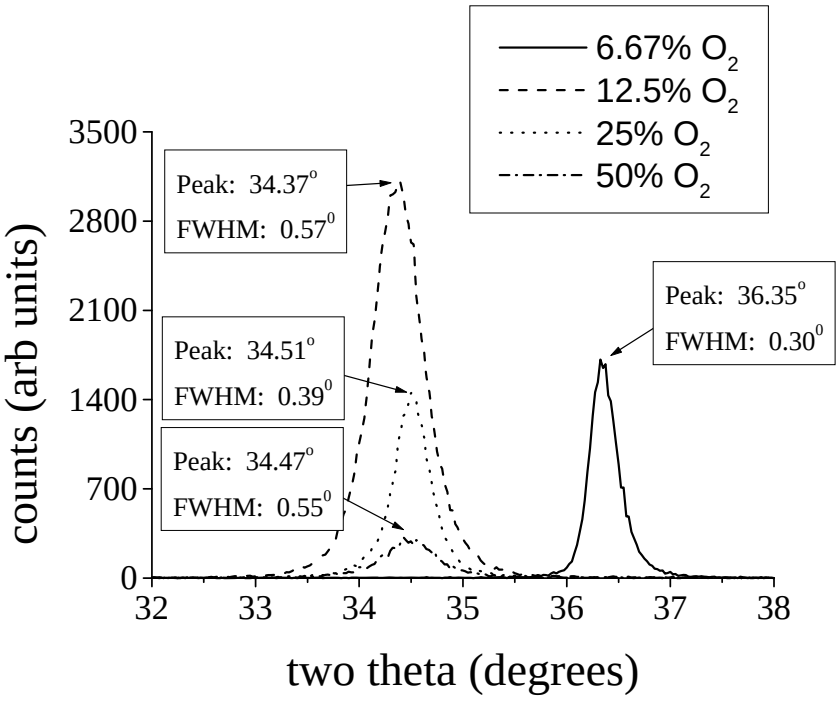

Figure 5-2 Effect of oxygen partial pressure on the (0002) x-ray reflection from $Zn_{0.8}Mg_{0.2}O$:Al (1.4 at % Al) films.

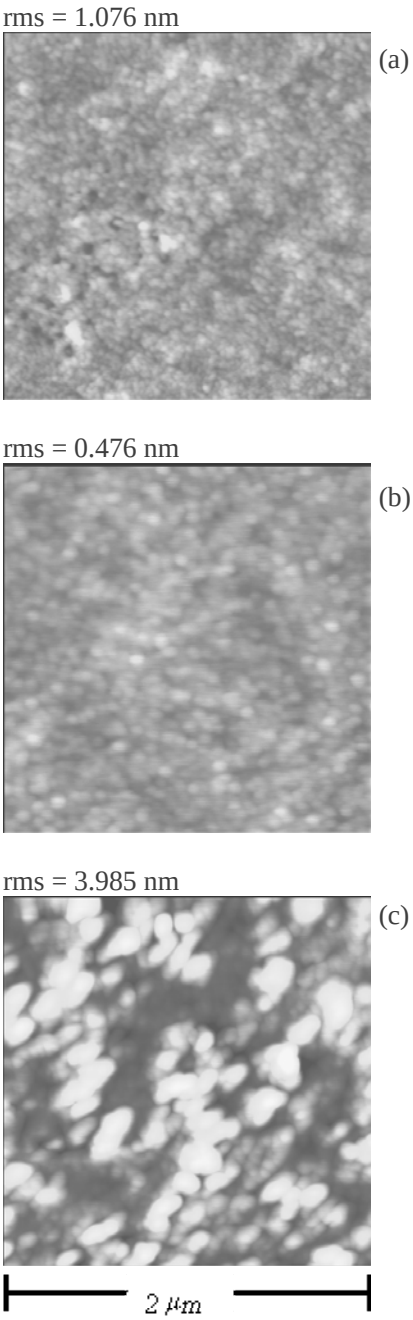

Figure 5-3 Atomic force microscope images of $Zn_{0.8}Mg_{0.2}O$:Al (1.4 at % Al) films grown at 12.5% O_2 (a), 25% O_2 (b), and 50% O_2 (c) with P_T = 6 mTorr. The full grey-scale height for each image is 20 nm.

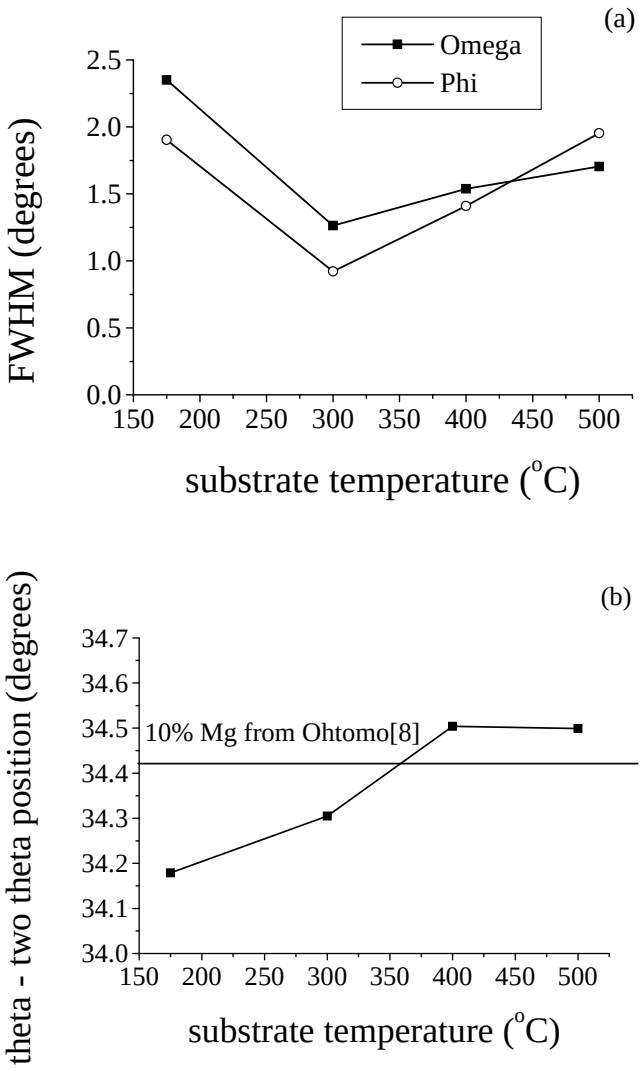

Figure 5-4 X-ray diffraction θ–2θ peak widths (a) and peak positions (b) versus substrate temperature from annealed $Zn_{0.9}Mg_{0.1}O$:Al (2.2 at % Al) films.

crystal quality up to T_S = 700°C. However, ZnO films deposited by r.f. magnetron sputtering[20] had a minimum in the rocking curve FWHM at T_S = 100°C. The θ–2θ position as a function of temperature is shown in figure 5-4(b), along with the value reported by Ohotmo et al[8] for $Zn_{0.9}Mg_{0.1}O$. Based on these results, a substrate temperature between 300°C and 400°C serves to relieve the residual compressive stress in these films. The trends are similar to those reported for ZnO:Al films grown by d.c. reactive magnetron sputtering.[21]

Figure 5-5(a) shows the θ-2θ peak position as a function of Al concentration for three different Mg contents. Adding Mg increased the 2θ value, i.e. the lattice spacing decreased, in agreement with prior results.[8] Increasing the Al content decreased the 2θ value, i.e. the lattice spacing increased, in agreement with prior results for ZnO:Al.[19] The lattice constants in the annealed films were in good agreement with values previously measured for ZnMgO, e.g. 0.519 nm measured here versus 0.518 nm by Ohtomo[8] for 20% Mg.

Figure 5-5(b) shows the θ-2θ peak width as a function of Al concentration for three different Mg contents. The θ-2θ peak width can be used to estimate the grain size using the Sherrer formula,[22] $d = 0.9\lambda/(B\cos\theta)$, where d is the grain size, λ is the wavelength of the x-rays, B is the θ-2θ peak width, and θ is the peak position. The grain size in the films, estimated using the Scherrer formula, ranged from ≈30 nm for undoped films to ≈ 10 nm for >2 at% Al. The small grain size in these epitaxial films is explained by a high density of low-angle grain boundaries due to the large lattice mismatch with the sapphire substrates.[15] The decrease of grain size with aluminum content has been

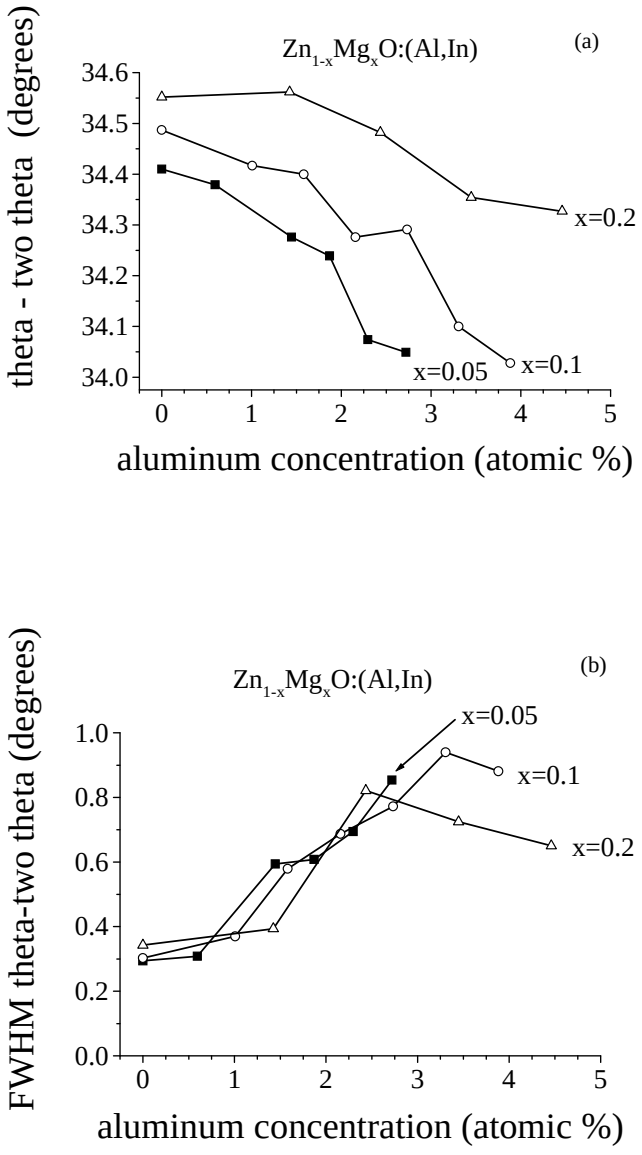

Figure 5-5 Effect of aluminum concentration on the θ–2θ peak position (a) and the θ–2θ peak width (b) for $Zn_{1-x}Mg_xO$:(Al,In) films with different Mg contents.

observed previously.[23] Although the mechanism is not completely understood, Nunes et al[24] attribute the decrease in grain size to the relatively large difference in ionic radius between zinc and aluminum. In general, annealing decreased the θ-2θ peak widths (figure 5-1(a)), indicating an increase in grain size; this can be explained by a reduction in the density of low-angle grain boundaries.

The full width at half maximum of the omega (out of plane) and phi (in plane) peaks varied relatively weakly as a function of Al content, and annealing had little measurable effect. The rocking curve FWHM values were typically 2-3^{o}, whereas the phi scan widths were 1.5-2.5^{o}. The relatively large peak widths were due to the large lattice mismatch of ~18% with the sapphire (0001) substrates, which leads to a mosaic structure.

5.3.3. Effect of Indium Annealing

Doping $Zn_{1-x}Mg_xO$ films with aluminum proved to be less effective than in pure ZnO. Table 5-1 summarizes the electrical properties of ZnO and $Zn_{0.9}Mg_{0.1}O$ films for different doping combinations. ρ is 100 times higher for ZnMgO:Al than for ZnO:Al. In order to improve the electrical properties, the films were annealed in the presence of indium, which acts as a donor in ZnO.[23] As can be seen in Table 5-1, double doping with In and Al generally decreased ρ, especially for ZnMgO. Figure 4-5(a), discussed in the last chapter, shows the effect of the In anneal time *t*, at 415^{o}C in 20 sccm hydrogen, 50 sccm argon, on the resistivity of a pure ZnO, ZnO:Al, and a $Zn_{0.9}Mg_{0.1}O$:Al (2.2 at % Al) film. The films were first annealed for 4 hours at 415^{o}C in 20 sccm hydrogen, 50 sccm

Table 5-1 Summary of the effect of doping on the electrical properties of ZnO and $Zn_{0.9}Mg_{0.1}O$ films. The Al-doped films were annealed at 415^{o}C for 4 hours in a H_2/Ar atmosphere. The In doping was achieved by annealing the films at 415^{o}C for 5 hours in a H_2/Ar atmosphere in the presence of indium.

Film	Al content (%active) (at %)	Resistivity (Ω cm)	Mobility (cm^2/Vs)	Carrier concentration (cm^{-3})
ZnO:In	0	1.72×10^{-1}	4.79	7.61×10^{18}
ZnO:Al	4.8 (3.8)	4.49×10^{-3}	18.15	7.67×10^{19}
ZnO:(Al,In)	4.8 (5.0)	2.89×10^{-3}	20.20	1.08×10^{20}
$Zn_{0.9}Mg_{0.1}O$:Al	2.2 (1.1)	2.06×10^{-1}	3.07	9.88×10^{18}
$Zn_{0.9}Mg_{0.1}O$:(Al,In)	2.2 (3.0)	3.28×10^{-2}	6.29	3.04×10^{19}

argon without indium present. The data points at $t = 0$ represent the resistivity of these In-free films. As is typically observed in ZnO films, the insulating as-grown films became conducting after the indium-free anneal; this has been attributed to the formation of intrinsic defects (oxygen vacancies/hydrogen) during the reducing anneal.[24,25] The ρ value decreased rapidly within the first $\approx$ 5h of In annealing, after which it decreased more gradually. The substantial decrease in ρ indicates the effectiveness of the In doping, particularly for undoped ZnO and ZnMgO:Al.

Figure 4-6 showed time-of-flight secondary ion mass spectrometry (SIMS) depth profiles taken after 42 hours of annealing in the presence of indium. The In concentration decreased rapidly with increasing depth within the first 50 nm, followed by a more gradual decrease. Note that the background In signal for an undoped sample was < 10 counts, such that even the lowest In level in figure 4-6 was well above the background. By comparison with an In-doped ZnMgO standard, obtained by sputtering from a ZnMgIn target, the reasonably constant In concentration throughout most of the film was $\approx 9 \times 10^{19}$ cm^{-3}. The In concentration profile in figure 4-6, combined with the decrease in ρ with increasing time in figure 4-5(a), is consistent with solid-state diffusion of In into the films from a vapor source. A similar effect could presumably be achieved by sputtering from a double-doped target. All of the results that follow are from films that were annealed in the presence of indium. The effect of the growth and annealing conditions on the hydrogen content in the films was not detectable using SIMS depth profiling. Once surface contamination was sputtered away, the hydrogen signal from the bulk film was at background levels (~ 10 counts).

5.3.4. Effect of Oxygen Partial Pressure and Temperature

The resistivity and mobility of annealed ZnMgO:(Al,In) films showed no clear trend as a function of T_S over the range from 175 to 500°C. For the 10% Mg alloy with 2.2% Al, for example, $\rho \approx 0.02\ \Omega$cm and $\mu \approx 10\ cm^2/Vs$. Given that there was considerable variation in structural perfection in this T_S range (figure 5-4), it appears that μ was not controlled by the film crystal structure.

Figure 5-6 shows the electrical properties as a function of oxygen partial pressure P_{O_2} for $Zn_{0.8}Mg_{0.2}O$:(Al,In) films grown at T = 300°C. The resistivity ρ shows a pronounced minimum at 1.5 mTorr oxygen, corresponding to an increase in electron density *n* with increasing P_{O_2} up to 1.5mTorr and a continuous increase in electron mobility μ with increasing P_{O_2}. The variation of *n* and μ with P_{O_2} can be explained by considering the deviation from stoichiometry caused by oxygen deficiency. Films grown at low oxygen contents have increased oxygen vacancy defect densities that lead to higher *n* after the post deposition anneal. On the other hand, this higher vacancy concentration will tend to increase electron scattering, decreasing μ. The results in figure 5-6 suggest a critical transition above 1.5 mTorr oxygen that drastically decreaseses the free carrier concentration. The transition can be understood in the context of the defect chemistry presented in equation 3-6. At lower oxygen partial pressures, the reaction producing aluminum atoms on zinc sites and free electrons is favored; however, above 1.5 mTorr oxygen the defect reaction favoring the formation of zinc vacancies is

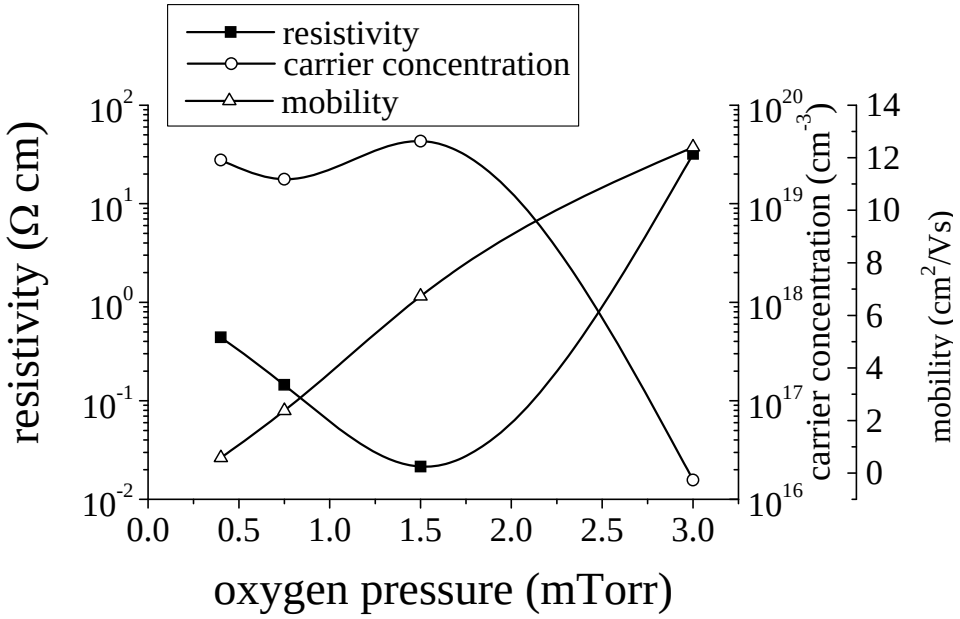

Figure 5-6 Effect of oxygen partial pressure on the electrical properties of In annealed $Zn_{0.8}Mg_{0.2}O$:(Al,In) (1.4 at% Al) films.

dominant. The zinc vacancies formed during growth in a high oxygen atmosphere compensate the free carriers produced by aluminum atoms on zinc sites. The electrical properties of the ZnMgO films were generally inferior to those of the best ZnO:Al films grown in this chamber, which showed μ = 26 cm^2/Vs, n = 4 x 10^{20} cm^{-3}, and ρ = 6.46 x 10^{-4} Ω-cm.

Figure 5-7 shows optical transmission spectra for annealed $Zn_{0.8}Mg_{0.2}O$:(Al,In) (1.4 at% Al) films that were grown at different oxygen partial pressures. An increase in electron density increases the free-carrier absorption in the near-infrared wavelengths and shifts the fundamental absorption edge to lower wavelengths due to the Burstein-Moss shift,[3] similar to ZnO:Al films. From 12.5 to 50% oxygen, the films showed sharp absorption edges and good transparency indicative of films with electron densities less than 1x10^{21}cm^{-3}.[26] The 20% Mg shifted the fundamental absorption edges to lower wavelength (higher E_G) relative to comparably doped ZnO films. The 6.67% oxygen film showed poor optical transmission and had a milky white appearance typical of an oxygen deficient film.[27] Note that films with higher Mg content targets generally showed lower sputter rates at a given target power, and hence a lower P_{O_2} (12.5% for $Zn_{0.8}Mg_{0.2}O$ versus ~ 20% for ZnO) was sufficient to maintain an O_2-to-metal flux ratio that yielded optically transparent films. Based on the above electrical and optical results, 25% oxygen was chosen for the films described below, in order to ensure high optical transparency and good electrical properties for all target compositions. This condition also yielded the best crystal perfection and surface flatness (see section 5.3.2.).

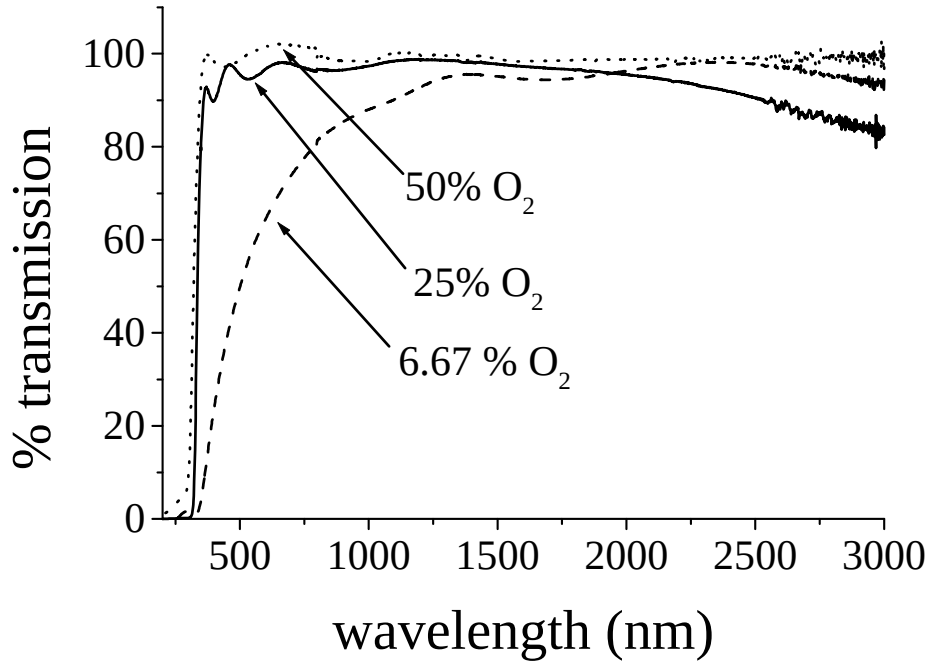

Figure 5-7 Effect of oxygen partial pressure on the optical transmission versus wavelength of In annealed $Zn_{0.8}Mg_{0.2}O$:(Al,In) (1.4 at% Al) films.

5.3.5. Effect of Mg and Al Content

Figure 5-8 summarizes the electrical properties of the In-annealed alloy films as a function of Al content, for three different alloy compositions and pure ZnO. The resistivity as a function of aluminum content for different alloy compositions and pure ZnO is displayed in figure 5-8(a). The resistivity values were generally higher for higher Mg content. For 20% Mg, there was an initial decrease in ρ with increasing Al content, but the resistivity showed only a weak variation with further increases in Al content. This is a result of the combined effects of the decrease in μ [figure 5-8(b)] and the increase in *n* [figure 5-8(c)] as the aluminum content was increased. These trends agree with prior results for ZnO:Al.[28] For 5 and 10% Mg, there was no clear correlation between ρ and Al content, but again this was due to the opposing variations in μ and *n*. Carrier concentration values generally decreased with increasing Mg content indicating that the Al and In dopants were less effective. μ values generally decreased with increasing Mg content.

Figure 5-9 shows the percent optical transmission as a function of wavelength for 20%Mg films with different Al concentrations. Also shown for comparison on figure 5-9 is the result for pure ZnO. The free-carrier absorption increased with increasing Al content, indicating an increase in the plasma frequency as expected based on the increase in electron density [figure 5-8(c)].[29] The plasma frequency (ω_p) is proportional to the square root of the carrier concentration (n) as given by the equation:[26]

$$\omega_p = \left(\frac{ne^2}{\varepsilon_0 \varepsilon_\infty m^*} \right)^{1/2} \qquad \text{Equation 5-1}$$

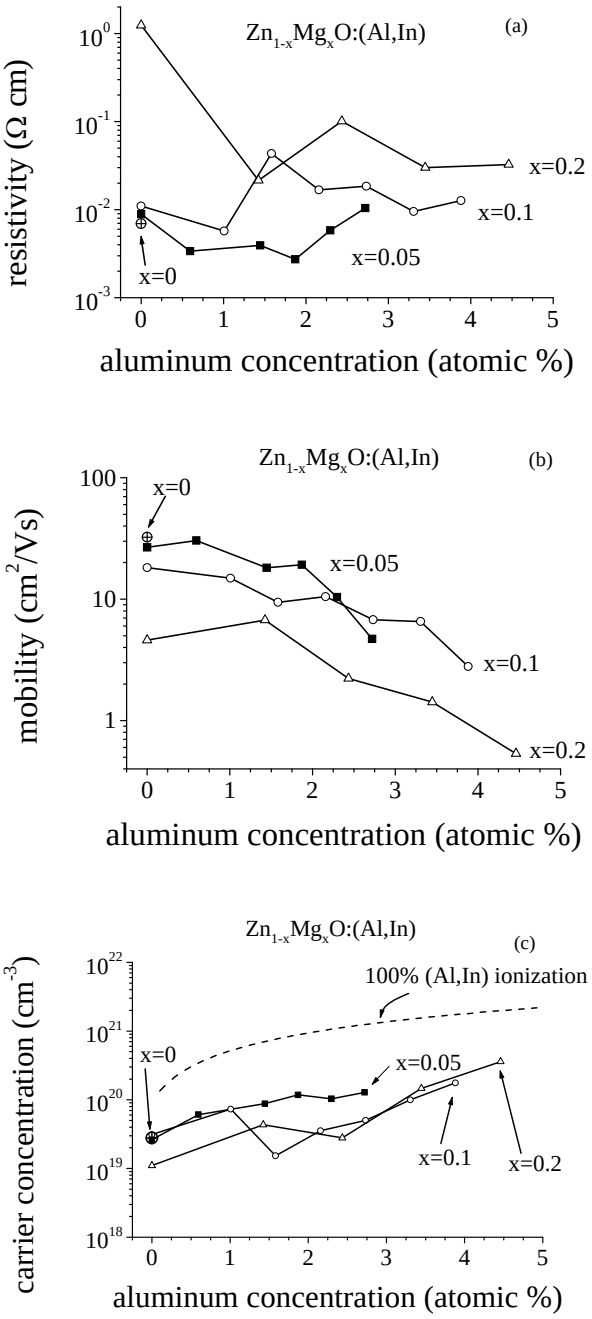

Figure 5-8 Resistivity (a), mobility (b), and carrier concentration (c) versus Al concentration in In annealed $Zn_{1-x}Mg_xO$:(Al,In) films with different Mg contents. Also plotted in (c) is the carrier concentration expected for 100% Al and In ionization.

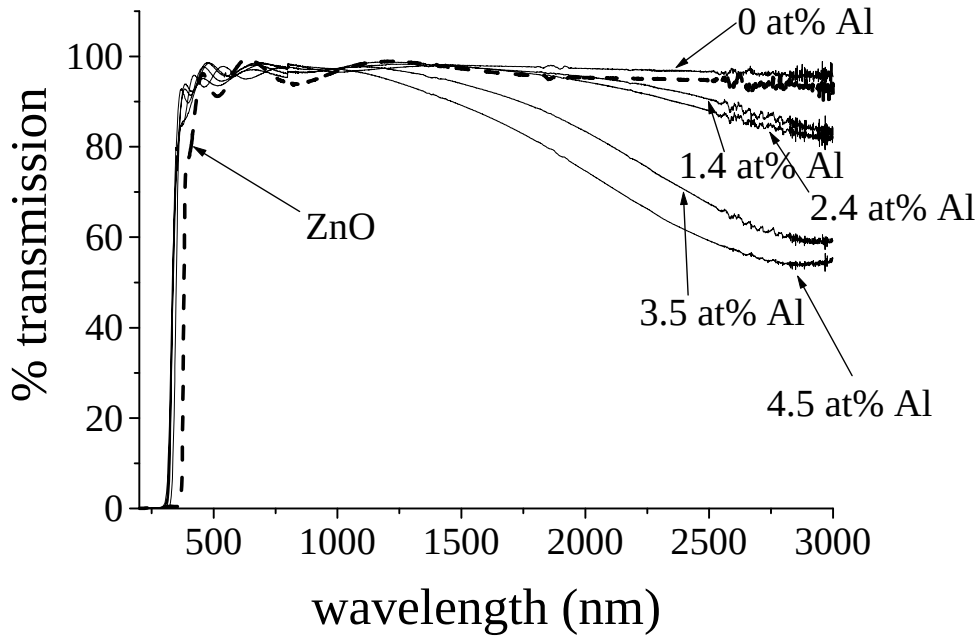

Figure 5-9 Optical transmission versus wavelength for In annealed $Zn_{0.8}Mg_{0.2}O$:(Al,In) films with different Al contents.

The constants in the equation are the electron charge (e), the effective mass (m^*), the permittivity of free space (ε_0), and the high-frequency permittivity (ε_∞). The plasma frequency for each of the films in figure 5-9 is less than the smallest frequency used for the scan, as demonstrated by the relatively high transmission values even at the smallest frequencies. Based on the carrier concentrations of the 4.5 at% Al sample (3.59 x 10^{20} cm^{-3}) and the 3.5 at% Al sample (1.46 x 10^{20} cm^{-3}), equation 5-1 predicts that the ratio of the plasma frequencies should be ~1.57. Although the plasma frequencies cannot be read from the plot, a rough estimate of the plasma frequency was taken to be the frequency that produced 60% transmission. Using this assumption, the ratio of the plasma frequencies for the two samples is 1.14, which is 28% smaller than that predicted by the carrier concentration. Clearly it is difficult to estimate the plasma frequencies from these plots; however, the general principal of increased free carrier absorption with increased free carrier concentrations is apparent. Despite the free carrier absorption, all films demonstrated an average transparency in the visible spectrum above 90%. Further evidence of the effect of the free carrier concentration on the plasma frequency is found by plotting the optical absorption coefficient at 2250 nm as a function of the free carrier concentration for the three highest aluminum concentrations in figure 5-9. The rationale is that the optical absorption coefficient should scale approximately linearly with the plasma frequency. The optical absorption coefficient roughly scales (within 20%) with the square root of the carrier concentration. Based on this analysis, the optical transmission scan can be used as a qualitative measure of the free carrier concentration in these ZnO based thin films.

The fundamental absorption edge shift to lower wavelengths caused by Mg is not visible on the scale shown in figure 5-9. Figure 5-10 shows the optical band gap E_G as a function of Mg and Al content. The optical band gaps were determined from data such as that shown in figure 5-9 by plotting the square of the optical absorption coefficient as a function of the photon energy and extrapolating the linear region to the energy axis.[30] The optical band gap increased with increasing Al content, due to the Moss-Burstein shift.[3] The values obtained for the optical band gap as a function of Mg content, for films with no Al, compare well to those obtained by Ohtomo.[8]

5.4 Discussion

All of the $Zn_{1-x}Mg_xO$:Al films were annealed in a H_2/Ar mixture in order to make them electrically conducting. Similar procedures are commonly used for ZnO:Al films. The results of intrinsic and extrinsic doping experiments suggest similar defect chemistry in ZnMgO:Al and ZnO:Al films. The role of intrinsic defects is evident from the observation that as-grown ZnO films were insulating, whereas after a reducing In-free anneal the films became mildly conductive. By analogy with results for ZnO, one explanation for the improved electrical properties after a reducing anneal is the creation of oxygen vacancies and zinc interstitials that are believed to be electron donors in ZnO, and are produced according to the following reactions[31]:

$$Zn_{Zn} + O_O \Leftrightarrow Zn_i^{\bullet} + e^{-} + \frac{1}{2}O_2(g) \qquad \text{(Equation 5-2)}$$

$$O_O \Leftrightarrow V_O^{\bullet} + e^{-} + \frac{1}{2}O_2(g)$$

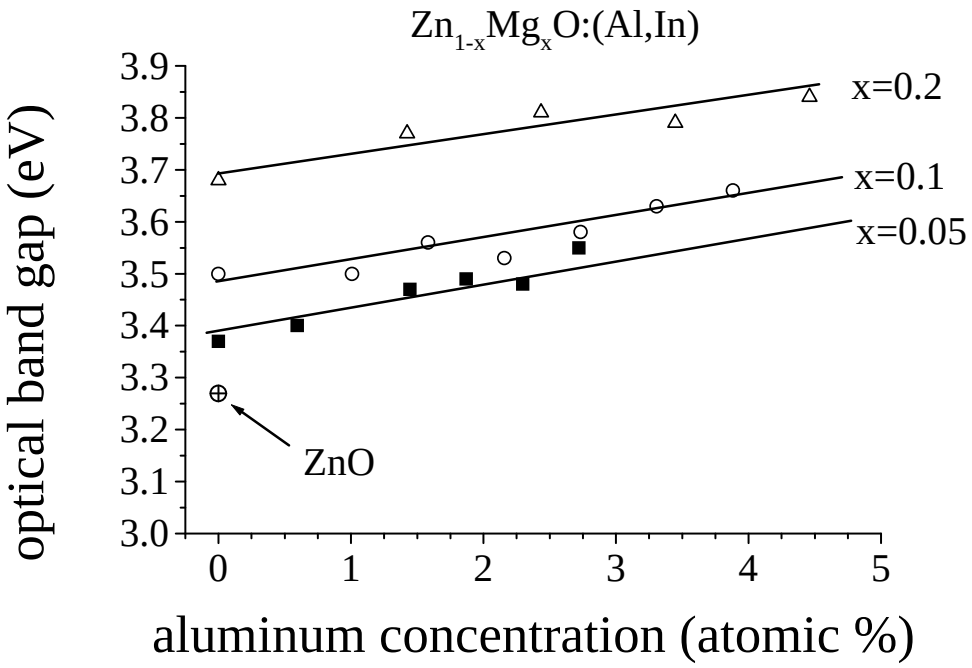

Figure 5-10 Effect of aluminum concentration on the optical band gap for In annealed $Zn_{1-x}Mg_xO$(Al,In) films with different Mg contents. Also shown is a data point for a pure ZnO film.

However, theoretical and experimental results point to hydrogen as a shallow donor in zinc oxide[25,32-34] providing an alternative or additional explanation.

The generally higher resistivities for ZnMgO resulted from both lower doping efficiency and lower mobility (figure 5-8) with increasing Mg content. Since these changes suggest a substantial change in band structure, we have estimated the conduction band effective mass *m** by plotting the shift in optical band gap ΔE_G with *n*. Assuming parabolic energy bands and a spherical Fermi surface, ΔE_G can be expressed as[26]:

$$\Delta E_G = \frac{\hbar^2 (3\pi^2 n)^{\frac{2}{3}}}{2m_r^*} \qquad \text{(Equation 5-3)}$$

where $\hbar$ is Planck's constant divided by 2π. Figure 5-11 shows a plot of E_G versus $n^{2/3}$. The y-intercept of the plot represents the fundamental energy gap (E_{G0}), and the slope can be used to calculate the reduced effective mass using equation 5-3. The fundamental energy gap calculated for 5% Mg (E_{G0}= 3.32 eV), 10% Mg (E_{G0}= 3.51 eV), and 20% Mg (E_{G0}= 3.73 eV) compares well with the pre-annealed optical band gap values obtained experimentally for the Al-free samples. The calculated reduced effective mass increases with magnesium content, 5% Mg m_r^* = 0.462 m_e, 10% Mg m_r^* = 0.7338 m_e, 20% Mg m_r^* = 1.5586 m_e, where m_e is the free electron mass. The addition of Mg seems to increases the effective mass compared to ZnO, m^* = 0.38 $m_{e;}$[35] however, without detailed information concerning the hole effective mass it is not possible to convert the reduced effective mass into an electron effective mass. Lu et. al. found a similar result when alloying ZnO films with MgO. Based on their measurements and calculations they concluded that the effective mass substantially increased with magnesium content.[36] Although the actual

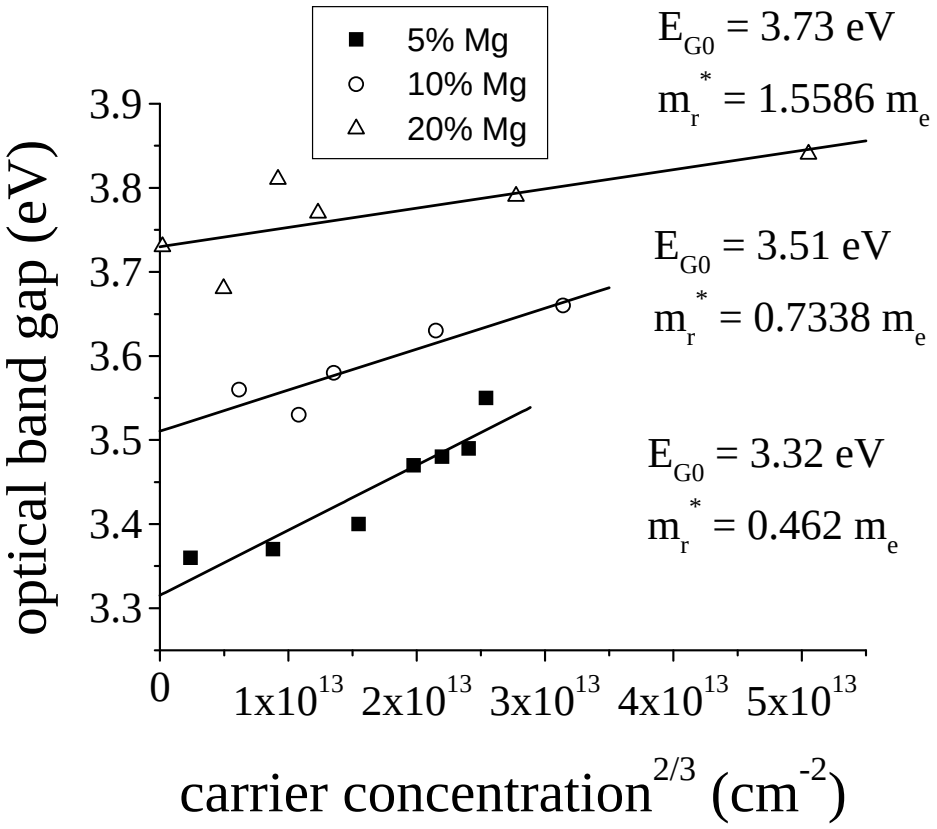

Figure 5-11 Optical band gap versus carrier concentration for $Zn_{1-x}Mg_xO$:(Al,In) films. Also shown are fits to the data using equation 5-3, and the fitting parameters.

values for the effective mass are lower in their work than in this study, the linear increase of the effective mass (and a resultant decrease in the mobility) with Mg concentration is a consistent result in both experiments.

The above results may help explain why the doping efficiency decreased with increasing MgO content, and extrinsic Al doping of the ZnMgO films proved to be ineffective [see table 5-1 and figure 5-8(a)]. Assuming a hydrogenic donor dopant model, the donor activation energy increases with increasing effective mass, and this would decrease doping efficiency. Alternatively, the formation of magnesium aluminate may have prevented aluminum from acting as an electron donor, according the equation[37]:

$$Mg_{Zn}^{X} + 2Al_{Zn}^{\bullet} + 2e^{-} + 3O_{O}^{X} + \frac{1}{2}O_{2(g)} \Leftrightarrow MgAl_2O_4(ppt) \qquad \text{(Equation 5-4)}$$

Note that magnesium aluminate clusters would be present at very low (≈1 vol%) levels due to the low Al concentrations in these films, such that they would not be easily detected by the techniques (x-ray diffraction) used in this study. In order to achieve lower resistivities, the films were double doped with indium through annealing in a reducing atmosphere. Figure 4-5(a) shows the reduction in resistivity possible when a ZnMgO:Al film is double doped with indium. The present results do not indicate that In is a superior dopant to Al – see for example the relatively high resistivities for In-doped ZnO in table 5-1 and figure 4-5(a). Rather, it was the combination of Al and In that was effective for doping ZnMgO. Co-doping of a TCO (tin oxide) with a cation donor (Sb) and an anion donor (F) has been reported,[38] although no substantial benefits were found. Co-doping has also been explored to enhance the conductivity of p-type semiconductors, e.g. GaN,[39] and mechanisms including alteration of complex formation, decrease of

compensation, increase in acceptor incorporation, and screening effects have been proposed. Co-doping with two cation donors has not been reported to our knowledge.

The addition of MgO to ZnO decreased electron mobilities, as shown in figure 5-12. μ did not appear to be strongly dependent on the crystal structure, based on results presented in section 5.3.4. For comparison, the mobility in intrinsic ZnO and ZnO:Al films is typically dominated by grain boundary scattering up to $n \sim 10^{21}\text{cm}^{-3}$, above which ionized impurity scattering dominates.[28] In the present ZnMgO films, the mobility appears to be controlled by the addition of Mg.

In order to understand the mobility decrease with increasing MgO content, both the effective mass variation and alloy disorder scattering were considered. Figure 5-12 shows the mobility calculated based on the increase in effective mass (figure 5-11) using the expression $\mu_{m^*}=e\tau/m^*$ and assuming that the relaxation time τ did not vary with alloy composition. This provides quite good agreement with the data. The mobility μ_{ad} due to alloy disorder scattering can be written as[40]:

$$\mu_{ad} = \frac{(2\pi)^{1/2} e\hbar^4 N_o}{3(m^*)^{5/2}(kT)^{1/2} x(1-x)(E_a - E_b)^2} \qquad \text{(Equation 5-5)}$$

where N_o is the number of atoms per unit volume, x is the fraction of alloy present, and E_a and E_b are the positions of the energy band edges in the pure materials. For (E_a-E_b) we have followed prior work,[40] where the energy gap difference was used to successfully fit the data. A value of 6.0 eV was used for the band gap of pure MgO, based on an

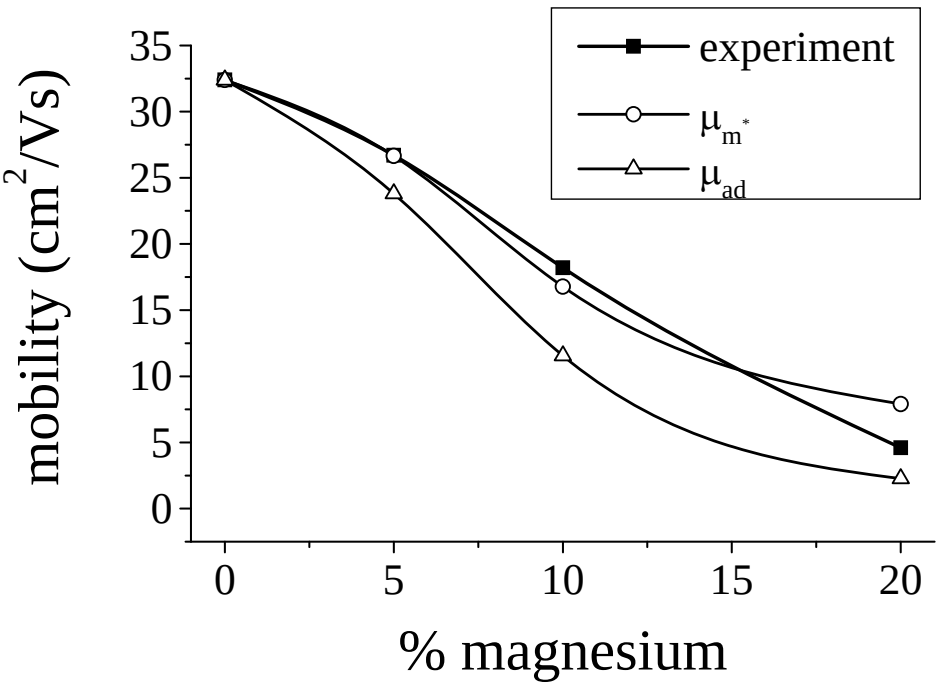

Figure 5-12 Effect of magnesium content on the mobility of $Zn_{1-x}Mg_xO$:In films. The effects of an increase in the effective mass (μ_{m^*}), and alloy disorder scattering [μ_{ad}, equation 5-5] are shown.

extrapolation of band gap vs. %Mg in hexagonal ZnMgO to 100% Mg, whereas the band gap for MgO in the cubic structure is 7.8 eV.[41] Figure 5-12 shows the mobility calculated using equation 5-5 and accounting for effective mass variations. The effect of alloy scattering appears to be relatively small, but it did yield slightly worse agreement with the experimental mobilities. The results of the calculations suggest that the increase in effective mass had the most significant effect on the mobility.

In order to compare the properties of the present films to other TCO's for applications such as solar cells, it is useful to define a figure of merit. An accepted figure of merit is the ratio of the electrical conductivity (σ) to the absorption coefficient in the visible spectrum (α).[42] A theoretical estimate of σ/α can be obtained based on the Drude free electron model[42]:

$$\frac{\sigma}{\alpha} = \frac{4\pi^2 \varepsilon_0 c^3 n (m^* \mu)^2}{\lambda^2 e^2} \qquad \text{(Equation 5-6)}$$

where ε_0 is the permittivity of free space, c is the speed of light, and e is the charge of an electron. Based on equation 5-6, the increasing m^* and decreasing μ with the addition of Mg to ZnO results in competing effects on σ/α. Equation 5-6 was used to estimate σ/α for the present films using an index of refraction (n) of 2.0,[42] a wavelength (λ) of 550 nm, experimentally measured Hall mobilities (μ), and effective masses (m^*) determined from figure 5-11. The resulting values are σ/α=3.07 Ω^{-1} for 5%Mg, σ/α=3.60 Ω^{-1} for 10% Mg, and σ/α=1.04 Ω^{-1} for 20% Mg. These σ/α values are comparable to those for ZnO films donor doped with group III elements (In, B, Ga, Al), ranging from 0.2 Ω^{-1} to 5 Ω^{-1}, although a higher value, σ/α=7.0 Ω^{-1}, was achieved for ZnO:F.[42]

5.5 Summary and Conclusions

High quality $Zn_{1-x}Mg_xO$:Al thin films were grown by direct current reactive magnetron sputtering, with FWHM values of the theta-two theta peak ~ 0.3-0.8 degrees, and FWHM values of the rocking curve ~ 2-3 degrees. These values compare well with a study that investigated ZnMgO films grown by RF magnetron sputtering (FWHM theta-two theta ~ 0.3-0.8 degrees, and FWHM rocking curve ~ 3-6 degrees).[43] The films also compare well to ZnMgO:Al films grown by PLD (FWHM theta-two theta ~ 0.35-0.5).[44] A post deposition indium anneal in a H_2/Ar mixture at 415°C was used to add In dopant and thereby significantly improve the electrical properties. The double doping of $Zn_{1-x}Mg_xO$ films with aluminum and indium achieved electrical resistivities an order of magnitude lower than doping with aluminum alone. The optimal electrical properties and optical transmission were achieved at a growth temperature of 300°C in a 25% oxygen atmosphere. The optical band gap was varied from 3.3 eV to 3.8 eV by controlling the magnesium content. The wide band gap and moderate electrical conductivity make these films potentially useful as transparent electrodes in photovoltaic cells to improve efficiency. $Zn_{1-x}Mg_xO$:(Al,In) films are also of interest for use in modulation doped TCO hetero-structures, based on their wide band gaps and high carrier concentration.

Chapter 6

Multilayer Simulations

6.1. Introduction

Transparent conductive oxides (TCOs) are utilized as electrodes in technologically important applications such as flat panel displays[1] and solar cells.[2] The development of larger screen sizes, higher efficiency photovoltaic cells, and transparent electronics[3-5] creates a need for TCO materials with improved properties, particularly lower resistivity and higher transparency. Recent attempts to decrease the resistivity $\rho = (ne\mu)^{-1}$ have typically focused on increasing the mobility μ rather than the carrier concentration n (e is the electron charge). This is because increasing n above a certain level leads to diminishing returns: decreased mobility due to ionized impurity scattering[6] and decreased transparency due to free carrier absorption.[7] The mobility $\mu = e\tau/m^*$ can be increased by increasing the relaxation time τ or by decreasing the effective mass m^*. Recently, TCO materials with lower effective masses and improved crystal quality, in order to increase τ, have been developed.[8-10] There is also an interest in achieving high mobility layers for transparent field-effect transistors.[11]

One proposed method for increasing τ in TCO's is by using modulation-doped multilayer films.[12,13] In this method, donor atoms are placed in wider band gap layers and the resulting conduction-band electrons transfer across the heterojunction interfaces to undoped, smaller band gap layers. Since the electrons are confined in the undoped

layers, there is minimal scattering by ionized impurities. While modulation doping has been successfully used to increase mobilities in many semiconductor systems including GaAs/AlGaAs,[14,15] GaN/AlGaN,[16] and Si/SiGe,[17] it has not been demonstrated in TCO's as a means for improving the average electrical and optical properties. The parameters defining modulation-doped multilayer structures, including layer thicknesses, compositions, and doping levels, must be chosen such that complete charge transfer from the doped to the undoped layers is achieved at high electron densities typical of TCO films. There is a need for a simulation tool that will provide information on the structural dimensions that can best achieve effective electron transfer and high mobility. Calculations were recently reported predicting enhanced electronic properties of modulation-doped oxides.[18] However, these calculations assumed generalized oxide properties, did not vary all of the key multilayer parameters, and did not consider the requirements for multilayer growth, e.g. lattice match between layers.

One-dimensional Poisson/Schrödinger simulations have been carried out for a proposed TCO modulation-doped system: ZnO/ZnMgO. The advantages of this system include reasonable lattice match (good quality ZnMgO epitaxial growth has been demonstrated)[19] and many of the parameters needed for the calculation – e.g. band gaps and effective masses[19] – have been measured. Thus, fairly realistic results can be expected from the calculation. The effect of layer thicknesses, donor concentration, and band gap offset on the simulated electrical properties are presented.

6.2. Simulation Procedure

The simulation program, developed by Snider,[20] uses the method of finite differences to self-consistently solve the one-dimensional Poisson and Schrödinger equations.[21] The number of mesh points used for each simulation was 500, which corresponds to a mesh spacing of between 0.27 nm and 0.071 nm. The boundary conditions used in the simulations were to set the slope of the bands equal to zero at the substrate and the surface. The output of the program includes the conduction and valence bands, electron distribution, and the wave functions for confined states.

Figure 6-1 shows a schematic diagram of the simulated multilayer structure. The ZnMgO, which has a larger band gap than ZnO,[22] is donor doped with aluminum to provide excess electrons.[19,23] The aluminum was assumed to be fully ionized to achieve the desired carrier concentration, and the mobility was controlled with a separate parameter. Undoped ZnMgO spacer layers separate undoped ZnO layers and the ZnMgO:Al layers. The values of the variables used in the calculations are given in Table 6-1. The band gap, effective mass, and mobility values for the ZnMgO layers are based on experimental results for 20 atomic % Mg films.[19] The heterojunction between ZnO and ZnMgO is assumed to have type I alignment with the difference in the band gap evenly divided between the conduction band offset and the valence band offset.[24] X-ray photoelectron spectroscopy (Omicron ESCA Probe) was performed on ZnO/ZnMgO samples grown in our lab by dc reactive magnetron sputtering to estimate the conduction band offset at the heterointerface.[25] While there was a relatively large uncertainty in the

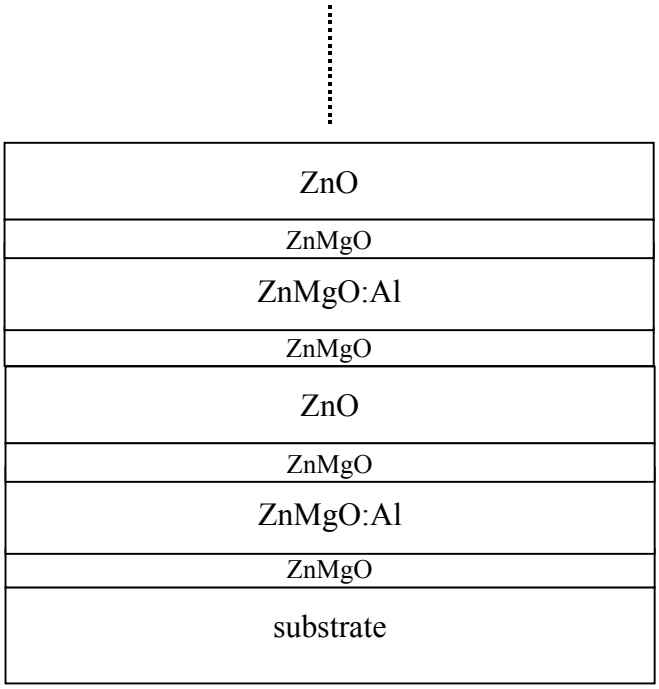

Figure 6-1 Schematic diagram showing two periods of the simulated modulation-doped multilayer structure.

Table 6.1. Summary of materials properties used in the simulations unless otherwise indicated.

Material	Band gap (eV)	Conduction band offset (eV)	effective mass ($/m_o$)	mobility (cm^2/Vs)
ZnO	3.3	0	0.38[37]	200
ZnMgO	3.8	0.25	1.5	5
ZnMgO:(Al)	3.8	0.25	1.5	5

measured position of the valence band edge, the results were consistent with equal valence and conduction band offsets, as used in the simulations.

Overall mobility values (for conduction parallel to the layers) were calculated by averaging the mobilities expected for each layer weighted by the predicted electron distributions. Table 6.1 shows the individual layer carrier concentration and the mobility values used in the calculations. A mobility of 200 cm^2/Vs, the value for pure bulk single crystal ZnO,[26] was assumed for electrons in the pure ZnO layers. The thickness of the undoped ZnMgO layer was set at 1.5 nm; as discussed in section 6.4, this thickness was chosen in order that ZnO mobilities would not be reduced by remote ionizied impurity scattering. The mobility for $Zn_{0.80}Mg_{0.20}O$, 5 cm^2/Vs, was a previously measured experimental value.[19,27] The carrier concentration in the undoped ZnO and ZnMgO layers was set at 1 x 10^{15} cm^{-3}. The static dielectric constant for all layers was set to 8.5.[28] The temperature was set to 300K for all of the simulations. All mobility, carrier density, and resistivity values quoted below are averages over the entire multilayer structure.

6.3. Results

Figure 6-2 shows the carrier concentration profiles and conduction band diagrams for typical structures: ZnMgO:Al thickness of 5 nm with [Al] = 1 x $10^{19}cm^{-3}$ (a), and [Al] = 1 x $10^{21}cm^{-3}$ (b), ZnO thickness of 5 nm, and ZnMgO thickness of 1.5 nm. For [Al] = 1 x $10^{19}cm^{-3}$, the conduction band shows the band bending typical of modulation doping, with energy minima at the edges of the pure ZnO layer. For [Al] = 1 x $10^{21}cm^{-3}$, local minima are still present, but they are actually at a higher energy than in the ZnMgO:Al

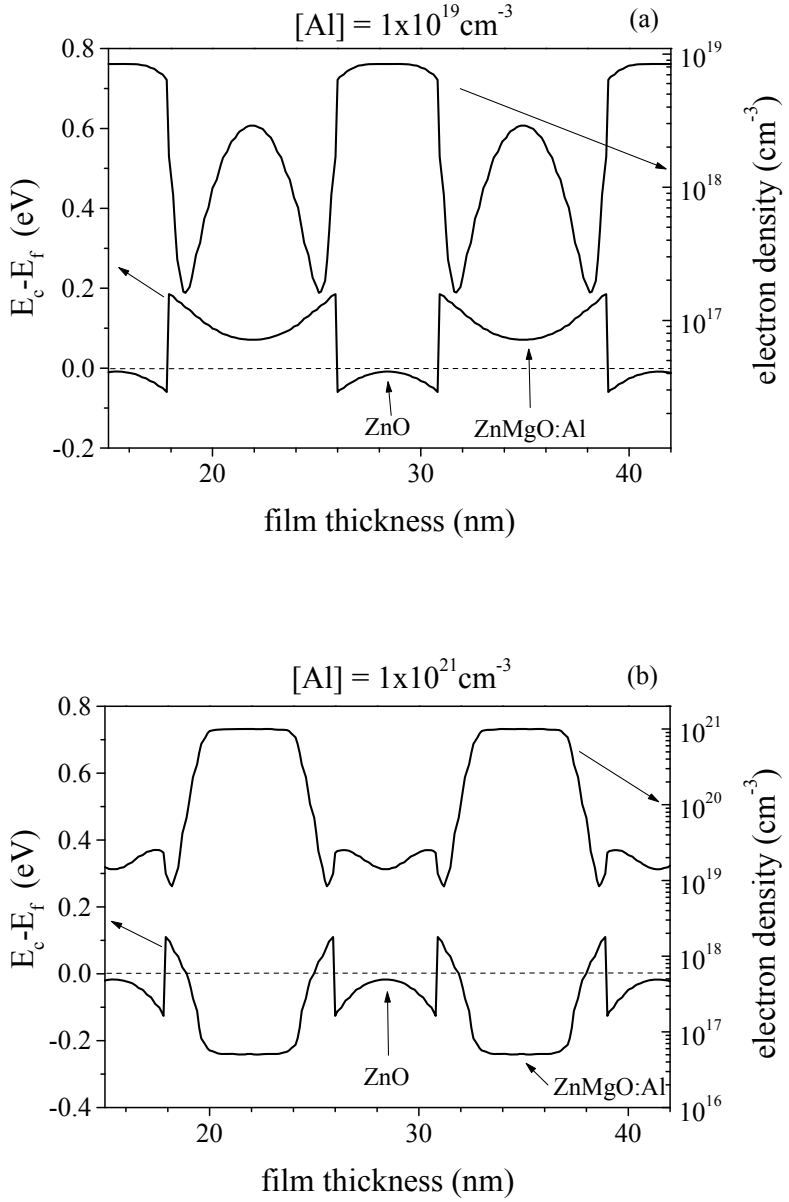

Figure 6-2 Calculated electron densities and conduction band positions for ZnMgO:Al doping densities of 1 x 10^{19} cm^{-3} (a) and 1 x 10^{21} cm^{-3} (b). The layer thickness values used are ZnMgO:Al = 5 nm, ZnMgO = 1.5 nm, and ZnO = 5 nm. The dashed line represents the position of the Fermi level.

layer. This results from the space charge density from the transfer of a large electron density from the ZnMgO:Al layers into the ZnO. The electron distributions within the layers are quite different for the two doping levels. For [Al] = 1 x $10^{19}cm^{-3}$, the electrons transfer into the ZnO layers up to a level of ~ 8 x $10^{18}cm^{-3}$, and the carrier concentration in the ZnMgO:Al layers falls to ~ 2 x $10^{18}cm^{-3}$. That is, ~88% of the electrons from the ZnMgO:Al layer are transferred to the ZnO and ZnMgO layers. Rather than forming a two-dimensional electron gas at the interfaces, there is a fairly uniform electron density throughout the ZnO layer. This results because the ZnO layer is relatively thin and electron sheet densities are relatively high. As the doping density is increased, larger electron densities [note that the ZnO electron density is much higher in figure 6-2(b) than figure 6-2(a)] result in space charge that raises energy levels thereby limiting further electron transfer. For example, in the [Al] = 1 x $10^{21}cm^{-3}$ case only ~8% of the electrons are transferred from the ZnMgO:Al. This shows an important trend: a limited number of electrons can be transferred between layers because of the space charge that builds up between transferred electrons and their ionized donors.

Figure 6-3 shows the effect of the ZnMgO:Al layer thickness and donor concentration on the average mobility [figure 6-3(a)] and the resistivity [figure 6-3(b)]. For all of the simulation results in figure 6-3, the ZnO thickness was 5 nm and the ZnMgO thickness was 1.5 nm. In figure 6-3(a) for a ZnMgO:Al layer thickness of 5 nm (the value used in figure 6-2), the mobility decreases from ~150 cm^2/Vs for an Al doping level of 10^{19} cm^{-3} to ~10 cm^2/Vs for an Al doping level of 10^{21} cm^{-3}. The higher mobility at the lower Al content reflects the efficient electron transfer to the high mobility ZnO

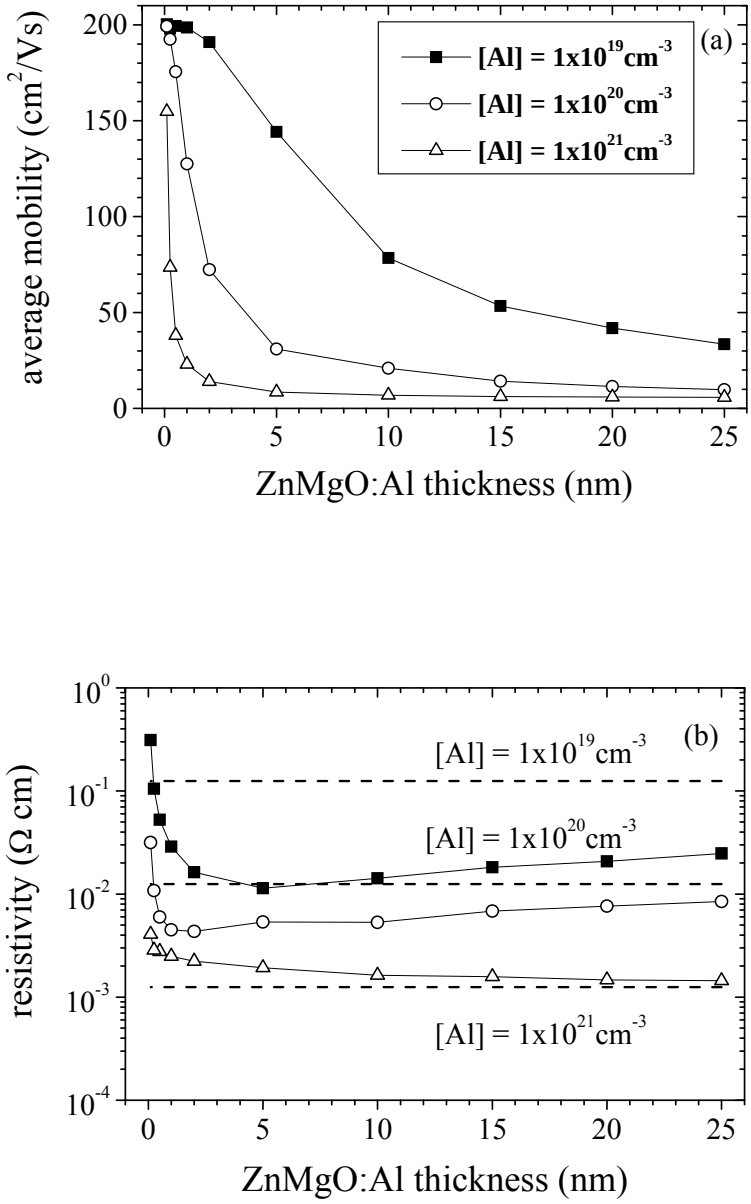

Figure 6-3 The calculated effect of doped layer thickness and donor concentration on the average multilayer mobility (a) and resistivity (b). The ZnO thickness is 5 nm and the ZnMgO thickness is 1.5 nm. The dashed lines in 6.3(b) represent the resistivities expected for the ZnMgO:Al layers at each donor concentration.

layer, whereas the higher electron density is mostly retained in the low mobility ZnMgO:Al layer (figure 6-2). In general, as the ZnMgO:Al layer thickness decreased, the average multilayer mobility increased, as it was possible to transfer a greater fraction of the electrons. Based on figure 6-3(a) there is a critical electron sheet density for efficient electron transfer. Typically, an average multilayer mobility of $\geq$150 cm^2/Vs was achieved for electron transfer of $\geq$ 88%, which occurred for electron sheet densities $\leq$ 10^{13} cm^{-2}.

Figure 6-3(b) shows that the overall multilayer resistivity decreases as the donor concentration increases. The dashed lines in figure 6-3(b) indicate the resistivity that would be expected for monolithic ZnMgO:Al layers for each donor concentration. For the lower Al doping levels, modulation doping substantially decreases the resistivity, primarily because of the high mobility achieved. The resistivity decreases as the doped layer thickness decreases, reaching a minimum at ~5 nm for an Al doping level of 10^{19} cm^{-3}, due to the increase in mobility shown in figure 6-3(a). Further decreases in doped layer thickness result in an increase in resistivity, despite increasing mobility, due to the decreasing fraction of the structure that is doped. For the highest Al doping concentration, the mobility increases only for very small doped layer thicknesses, and no resistivity decrease was observed.

The effect of ZnO layer thickness on the average mobility is shown in figure 6-4(a), and on multilayer resistivity in figure 6-4(b). The ZnMgO:Al thickness is 5 nm and the ZnMgO thickness is 1.5 nm. High mobilities were achieved for lower Al concentrations, with the low mobilities at higher Al concentrations again due to

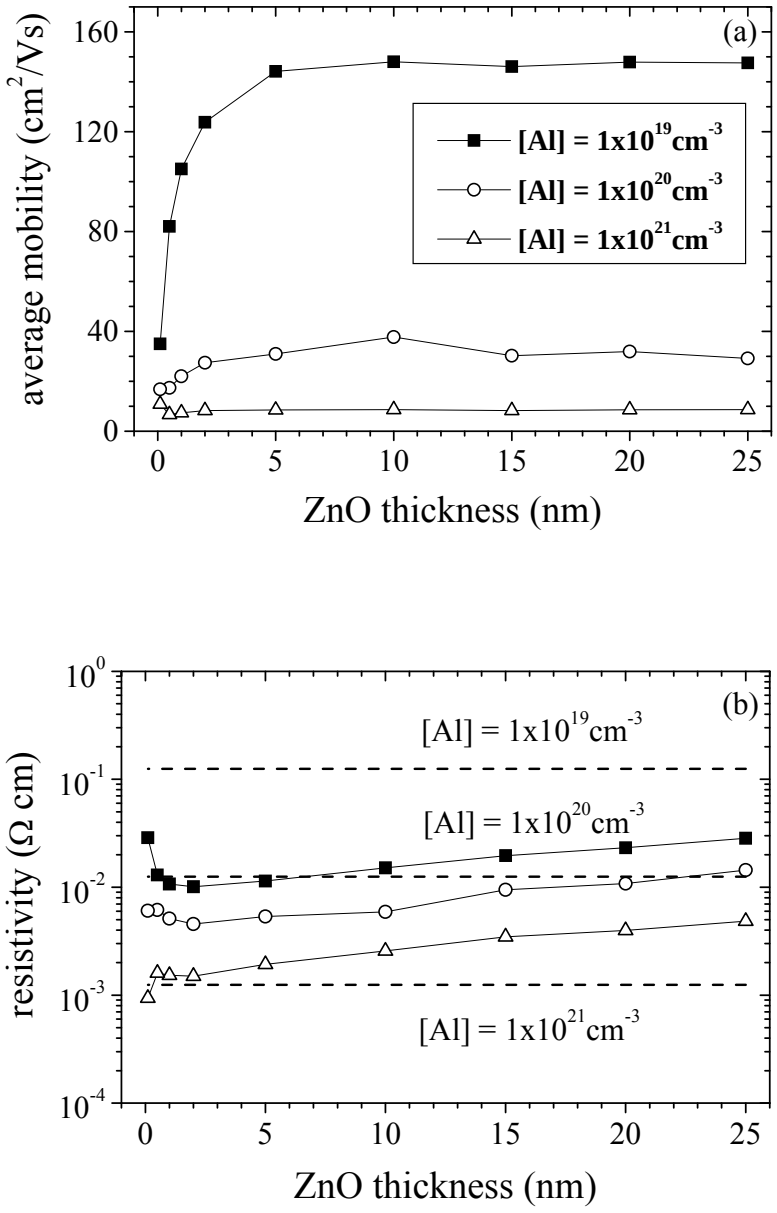

Figure 6-4 The calculated effect of ZnO layer thickness and donor concentration on the average multilayer mobility (a) and resistivity (b). The ZnMgO:Al thickness is 5 nm and the ZnMgO thickness is 1.5 nm. The dashed lines in 6.4(b) represent the resistivities expected for the ZnMgO:Al layers at each donor concentration.

ineffective electron transfer as in figure 6-3(a). There was little effect of ZnO thickness above 5 nm on the mobility, but below 5 nm the mobility decreased. This was explained by a rapid decrease in the number of confined electron states with decreasing ZnO thickness, which limited the density of electrons that could be transferred to the ZnO, thereby limiting the mobility. For example, the wavefunction calculations showed no confined states for ZnO thickness < 1-2 nm for ZnMgO:Al doping densities of 10^{19} - 10^{20} cm^{-3}. The multilayer resistivity [figure 6-4(b)] decreases as the ZnO thickness decreases down to ~2 nm, due to the decreasing fraction of undoped material (higher average doping density). The resistivity increase for thickness decreased below 2 nm is explained by the mobility decrease shown in figure 6-4(a). The dashed lines in figure 6-4(b) represent the resistivity of the ZnMgO:Al layers for each donor concentration. The multilayers with lower donor concentrations show a greater improvement in resistivity when compared to the resistivity of the ZnMgO:Al layer by itself [dashed lines in figure 6-4(b)].

The lowest resistivity value obtained in these simulations was 1.21 x 10^{-3} Ωcm for a multilayer with 1 nm thick ZnO and ZnMgO:Al layers and an Al concentration of 10^{21} cm^{-3}. In this case, however, the mobility was only ~20 cm^2/Vs. Further improvements with decreased layer thicknesses were not possible owing to the low average mobility of the multilayer when the ZnO thicknesses were small.

In the above calculations, the conduction band offset ΔE_C was taken to be $\Delta E_G/2$, or 0.25eV assuming $Zn_{0.8}Mg_{0.2}O$. However, the actual offset may be different based on a different alloy composition or if the offset is actually a different fraction of the band gap.

Thus, we have explored the effect of ΔE_C on the average mobility [figure 6-5(a)] and the resistivity [figure 6-5(b)]. As shown in figure 6-5, the mobility increases and resistivity decreases as ΔE_C increases. The influence of ΔE_C on the average mobility is more pronounced at lower donor concentrations indicating a greater efficiency in the transfer of electrons from the ZnMgO:Al layers to the ZnO layers. Above ~0.3 eV the average mobility for the [Al] = 1 x 10^{19}cm^{-3} series tends to level out as the mobility value approaches the ZnO value of 200 cm^2/Vs, indicating 100% electron transfer. As a result, further increases in ΔE_C will not significantly improve the electron concentration in the ZnO layers. The changes in resistivity with ΔE_C along with the resistivity values of the ZnMgO:Al layers by themselves (dashed lines) are shown in figure 6-5(b). Once again, the improvement in the resistivity as a result of the multilayer structure is most pronounced at lower donor concentrations.

6.4. Discussion

The simulations in this work provide insight into the possibility of using ZnO/ZnMgO modulation-doped TCO's. In order to compete with existing TCO's for applications such a flat panel displays and solar cells it is necessary to achieve a low resistivity. Based on figure 6-3(b) and figure 6-4(b) the lowest resistivity can be achieved when the ZnMgO:Al and ZnO layers are less than 5 nm. In our simulations we found that the multilayer structures had lower resistivities than their constituent monolithic layers [dashed horizontal lines in figure 6-3(b) and 6-4(b)] at low donor concentrations. For a

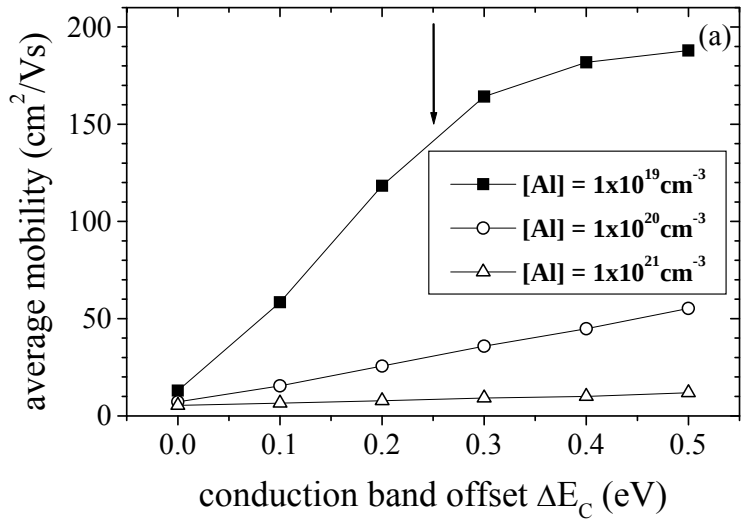

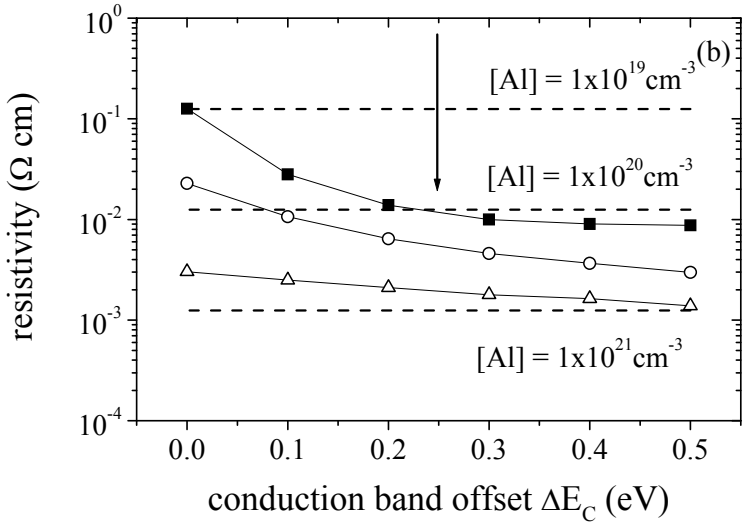

Figure 6-5 The calculated effect of conduction band offset ΔE_C and donor concentration on the average mobility (a) and resistivity (b). The ZnO thickness is 5 nm, the ZnMgO:Al thickness is 5 nm, and the ZnMgO thickness is 1.5 nm. The dashed lines in 6.5(b) represent the resistivities expected for the ZnMgO:Al layers at each donor concentration. The arrows indicate the offset value used in the calculations.

donor concentration of 1 x 10^{21}cm^{-3} the resistivity approaches the monolithic limit when the ZnO thickness is 2 nm [figure 6-4(b)]. This result is in agreement with simulations performed by Robbins and Wolden[18] showing that the conductivity of a multilayer TCO structure approached that of a monolithic TCO film when well thicknesses were $\leq$ 5 nm. In general, it was not possible to achieve resistivities significantly lower than 10^{-3} Ωcm. This was due to the inability to transfer very high electron densities into the undoped ZnO layers for reasonable layer thicknesses, i.e. > 1nm. Also, the maximum average carrier density is reduced because only one of the three layers is doped. Thus, these materials will not compete directly with conventional TCO's in applications that require very low resistivities. However, they can provide superior transparency in moderately conductive layers because of the high mobilities that can be achieved. Modulation doping also offers the possibility of creating a high mobility two-dimensional electron gas (2DEG), which will be important in all-transparent electronics to improve device speeds.[3,4,11]

The present results apply specifically to the ZnMgO system. However, they can be extended to make general predictions about other multilayer TCO's. The general characteristics that will make for a good modulation-doped TCO are as follows: (1) the doped layer should have the ability to be heavily doped; (2) the undoped layer should have the highest possible mobility; and (3) there should be a large conduction band offset. One possible candidate for the undoped layer is CdO, where a mobility of 600 cm^2/Vs has been reported.[10] Although this material has a band gap that is too small to be a good TCO on its own, in a thin layer the quantum size effect would increase the

effective band gap, improving transparency. CdO also exhibits a large Burstein-Moss effect[10] which should increase the effective band gap when electrons are transferred from the wide band gap layers.

The following discussion concerns the assumptions used regarding mobility values in the calculations. One of the key features in a modulation-doped structure is the intrinsic spacer layer, which physically separates the 2DEG from the ionized impurities. The choice to include an intrinsic ZnMgO spacer layer in the simulations was based on theoretical and experimental results for GaAs/AlGaAs modulation-doped structures. Previous simulations on multi-layer TCO's did not include an undoped spacer layer in their calculations.[18] The presence of the spacer layer, which minimizes electron wavefunction overlap into the doped layers, makes the assumption of $\mu = 200$ cm^2/Vs in the ZnO layers more realistic. However, this depends on a correct choice of the ZnMgO layer thickness. This choice is discussed further below.

Simulations were performed to compare the electron wavefunction widths in ZnO/ZnMgO and GaAs/AlGaAs quantum wells. In both cases the quantum well was 2 nm thick, the donor concentration was 1 x 10^{19}cm^{-3}, the conduction band offset was 0.25 eV, and there was only one confined state in the quantum well. The barrier layers in each simulation were made sufficiently thick so that boundary effects did not influence the calculation near the quantum well. The wavefunction in the ZnO system attenuates within ~ 1.5 nm of the quantum well, whereas in the GaAs system the wavefunction extends ~ 7 nm into the barrier region. The larger extent of the wavefunction in GaAs is a result of the much lower electron effective mass (0.067 m_e for GaAs and 0.094m_e for Al

$_{0.324}$Ga $_{0.676}$As) compared to ZnO (0.38 m_e for ZnO and 1.5 m_e for Zn $_{0.8}$Mg $_{0.2}$O). The simulation for GaAs/AlGaAs agrees very well with experimental data for GaAs/AlGaAs quantum wells which show a mobility maximum at a spacer layer thickness between 5 nm and 7 nm.[29] This result suggests that a 1.5 nm ZnMgO spacer layer effectively separates the electron wavefunction from the ionized impurities.

A more quantitative calculation considers the effect of spacer layer thickness on the mobility of the 2DEG limited by remote ionized impurity scattering μ_{2d}, given by[30,31]

$$\mu_{2d} = \frac{16\sqrt{2\pi}ed^3 n^{\frac{3}{2}}}{\hbar n_I} \qquad \text{(Equation 6-1)}$$

where e is the electric charge, d is the spacing between the 2D sheet of electrons (n cm^{-2}) and the 2D sheet of ionized impurities (n_I cm^{-2}), and $\hbar$ is Plank's constant divided by 2π. Equation 6-1 is derived from a calculation of the scattering potential in a modulation doped structure, which assumes that the impurities reside in a thin layer, located a distance d from the conduction electrons. It is also assumed that the doping density is low enough, so that each impurity scatters electrons independently.[32] The critical result is that the mobility increases with the cube of the spacer layer thickness. The values for mobility calculated from equation 6-1 agree well with experimental results for GaAs/AlGaAs modulation-doped structures.[30] Figure 6-6 shows the mobility based only on this remote ionized impurity scattering mechanism, assuming $n = n_I$, and that only the first subband in the 2DEG is occupied. Figure 6-6 indicates that at the spacer layer

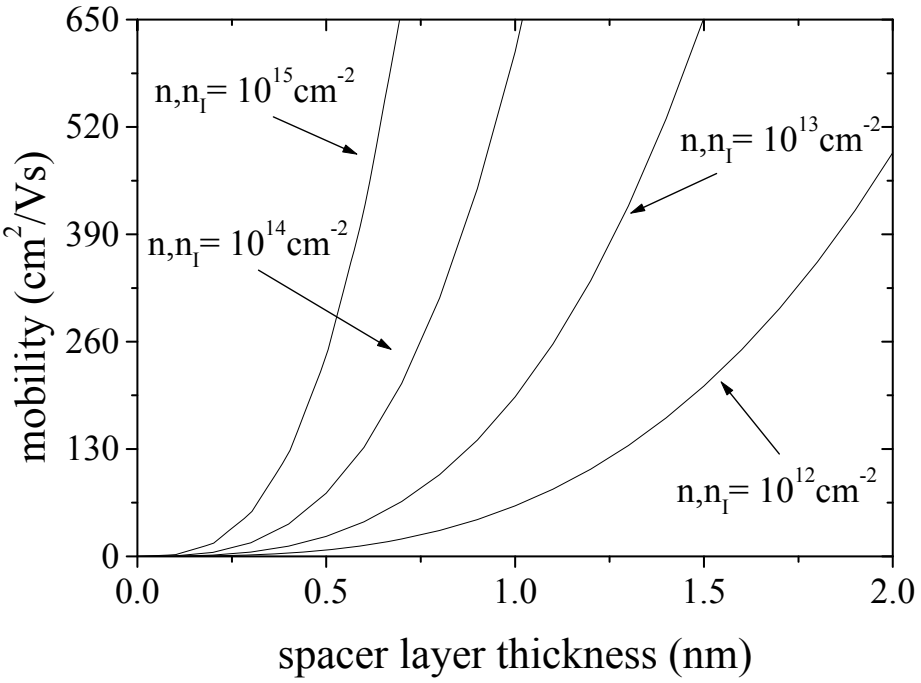

Figure 6-6 Remote ionized impurity scattering mobility as a function of spacer layer thickness and electron/ion sheet concentration.

thickness used in the simulations (1.5 nm) and the critical transferable electron sheet density (10^{13} cm^{-2}), the mobility limited by remote ionized impurity scattering is ~650 cm^2/Vs, substantially higher than the bulk ZnO mobility of ~200 cm^2/Vs which is limited by phonon scattering.

The success of a high mobility 2DEG in ZnO/ZnMgO structures depends on finding a layer thickness and donor concentration that produces a single confined state per quantum well, thereby eliminating inter-subband scattering.[31] Figure 6-7 shows the effect of ZnO thickness on the square of the electron wavefunction. For clarity, the conduction band diagram is shown as a dashed line. Figure 6-7 shows two types of potential wells that exist in these structures. The first is the triangular shaped well formed at the heterointerface due to band bending, the second is the quantum well formed in the entire ZnO layer as a result of the conduction band offset between the layers. When the ZnO thickness is 25 nm all of the confined energy states lie within the triangular shaped well at the heterointerface. At a ZnO thickness of 10 nm quantized states reside both in the triangular shaped well and within the well formed by the entire ZnO layer. When the ZnO thickness reaches 5 nm there are only states confined by the entire ZnO well, since the quantized energy levels are above the triangular wells at the interface. The transition from states being confined to the triangular well to states being confined to the entire ZnO layer as the ZnO thickness decreases is clearly shown. When the ZnO thickness is large [figure 6-7(a)] there are two triangular quantum wells per ZnO layer. Although the large ZnO thickness is not conducive to a low overall resistivity [figure 6-4(b)], it may be the best conditions to produce a high mobility 2DEG. At

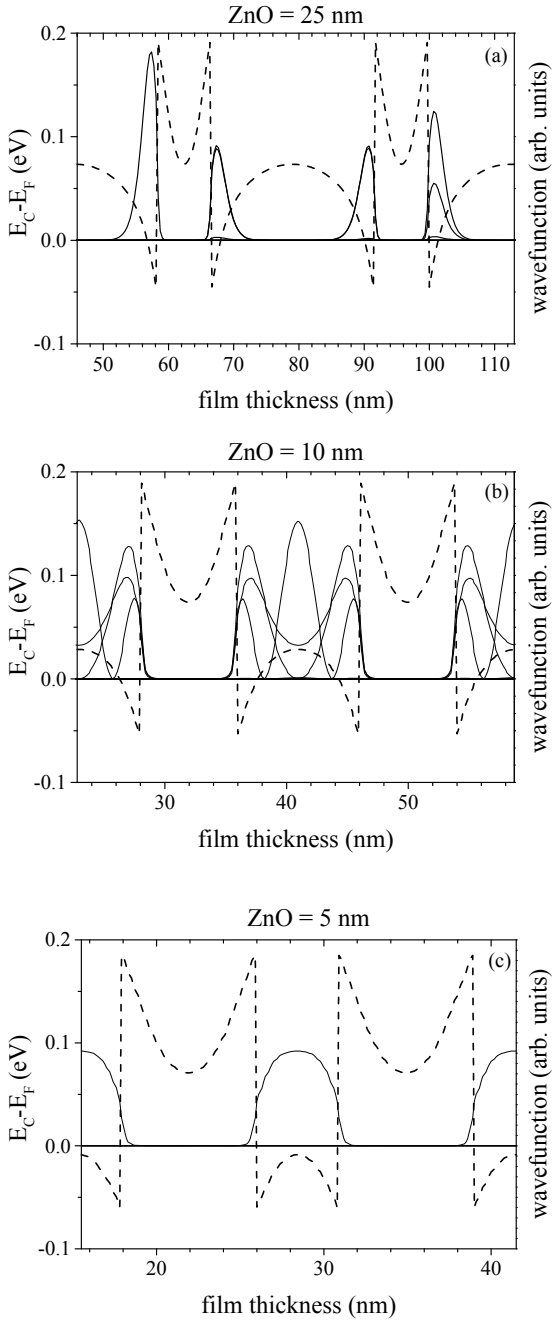

Figure 6-7 Conduction band energy diagrams (dashed lines) and the square of the electron wavefunctions for ZnO thicknesses of 25 nm (a), 10 nm (b), and 5 nm (c). The ZnMgO:Al thickness is 5 nm with a donor concentration of 1 x 10^{19} cm^{-3}, and the ZnMgO thickness is 1.5 nm.

ZnO = 10 nm [figure 6-7(b)] there is the possibility of extensive inter-subband scattering which may reduce the mobility.[31,33] When the ZnO layer is 5 nm it may be possible to achieve low resistivity and a high mobility 2DEG at the same time since there is only one confined state per quantum well [figure 6-7(c)].

The simulations in this work assume the ability to grow highly perfect, lattice matched epitaxial films with the desired purity and dopant levels. According to Gossard and Pinczuk the criteria for successful modulation doping are (1) absence of scattering centers in the conducting channel regions, (2) smooth and pure interfaces bounding these regions, (3) minimization of traps and compensating centers in the barriers, and (4) separation of the dopant atoms from the channel regions.[31] The choice of the ZnMgO system with reasonable lattice match (0.3% lattice mismatch for 20% Mg)[22] reflects these requirements. Furthermore, oxide crystal growth technology has improved to the point where high quality heterojunctions can be grown.[34-36] Nonetheless, most epitaxial ZnO films are grown on (0001) sapphire substrates in which there is a 18% lattice mismatch between film and substrate, introducing surface roughness and crystal imperfections. Finally, the ability to control the carrier concentrations in TCO films is always a challenge as a result of inherent non-stoichiometry, but recent work has shown that this is possible with ZnMgO.[19] Many TCO applications would require a polycrystalline modulation-doped structure. Thus, if modulation doping is successfully demonstrated in epitaxial films, investigations of polycrystalline films will be needed. The strong preference of ZnO to grow with a (0002) orientation and a columnar grain strucuture[37] may provide locally smooth interfaces necessary for electron transfer. The role of grain

boundaries as electron traps and scattering centers may ultimately limit the attainable properties in polycrystalline films.

6.5. Summary and Conclusions

A one-dimensional Poisson/Schrödinger program was used to investigate the effect of layer thicknesses, donor concentration, and band gap offset on the electrical properties of transparent conducting modulation-doped ZnO/ZnMgO multilayer structures. Mobilities as high as 144 cm^2/Vs were predicted for a structure with average carrier density 8 x 10^{18} cm^{-3} and resistivity 1 x 10^{-2} Ωcm; for a comparable resistivity in monolithic ZnO, the mobility would be lower ~30 cm^2/Vs and the carrier density higher. The ability to confine conduction electrons to a 2DEG offers enhanced flexibility in the design of transparent electronics, allowing for the possibility of modulation-doped field-effect transistors. Thus, the modulation doping approach is a possible means for enhancing TCO properties. However, it was found that the maximum sheet electron density that could be transferred from the doped to the undoped layers was ~10^{13} cm^{-2}, limiting the lowest resistivity to 1.5 x 10^{-3} Ωcm. Thickness ranges providing highest mobilities combined with low resistivity were 2-5 nm for the pure ZnO and 2-5 nm for the ZnMgO:Al. A pure ZnMgO set-back layer thickness of ~ 1.5 nm was used in order to minimize the impact of remote ionized impurity scattering on mobility. The undoped ZnO layer thickness should be either small, ≤ 5 nm, or large, ≥ 25 nm, in order to avoid possible inter-subband scattering.

The results obtained based on these one-dimensional Poisson/Schrödinger simulations can be compared to experimental results reported by other investigators. Koike et.al.[38,39] used molecular beam epitaxy to grow $Zn_{0.60}Mg_{0.40}O$/ZnO modulation doped heterostructures. When the $Zn_{0.60}Mg_{0.40}O$ layer was doped with aluminum to a carrier concentration of $8x10^{19}$ cm^{-3} the mobility at room temperature was ~80 cm^2/Vs and the sheet carrier density in the ZnO well was ~$4x10^{13}$ cm^{-2}. When the $Zn_{0.60}Mg_{0.40}O$ layers were not intentionally doped, the room temperature mobility was ~175 cm^2/Vs and the sheet carrier density in the ZnO well was ~$1.5x10^{13}$ cm^{-2}. The experimental results reported by Koike quantitatively agree with the simulation results presented in figure 6-4 (a). Koike used a ZnO thickness of 50nm so it is appropriate to use the right hand side of figure 6-4 (a) where the dependence on ZnO thickness is very weak. The prediction results are consistent with the above experimental results (although a direct comparison cannot be made because the exact carrier densities simulated did not the experimental values). The experimental sheet carrier densities also agree well with the maximum transferable densities suggested by the model, which were on the order of 10^{13} cm^{-2}.

Tampo et. al.[40,41] have also grown ZnMgO/ZnO heterostructures using MBE. They did not intentionally donor dope the ZnMgO layers, and the carrier concentration was ~$8x10^{18}$ cm^{-3}. The Mg composition was varied from 0.05 to 0.45, however, the sheet carrier concentration in the ZnO well remained constant at $1x10^{13}$ cm^{-2}. The room temperature mobility showed a strong dependence on the Mg composition, for Mg=0.05 the mobility was ~100 cm^2/Vs and it increased to ~250 cm^2/Vs at Mg=0.20, after which it stayed constant up to Mg=0.45. These results agree well with the simulations shown in

figure 6-5(a), where conduction band offset is controlled by the Mg composition. For a carrier concentration of $1x10^{19}$ cm^{-3}, the simulations predict a strong increase in mobility up to a band offset of ~0.25 eV, after which the mobility levels off to ~190 cm^2/Vs.

The theoretical simulations qualitatively and quantitatively agree with the available experimental results for ZnMgO/ZnO heterostructures. A good agreement was also obtained with the present experimental results, that were at higher doping concentrations than the above results, as discussed in Chapter 7. The simulations should prove to be a useful tool in the design of future experiments, and they can also be used to explain experimental results for modulation-doped structures.

Chapter 7

ZnO/ZnMgO Growth and Characterization

7.1. Introduction

The central goal of the research in this dissertation was to develop materials that could be incorporated into multilayer transparent conducting oxides, and to investigate the possibility of applying the technique of modulation doping to TCOs. In this chapter the optical, electrical, and structural properties of multilayer films grown by reactive magnetron sputtering are reported. The properties of multilayer films were compared to monolithic films, and the effects of post-deposition annealing were studied. The optical properties were investigated using UV-VIS-NIR spectrophotometry, electrical measurements were done using the temperature dependent Hall effect, and the structural properties were characterized using XRD, SIMS, and TEM. Although the multilayer films were structurally stable, the optical and electrical properties indicated an averaging effect rather than greatly improved properties resulting from significant electron transfer.

7.2. Optical Properties

Consistent with the results for monolithic films it was necessary to perform a post deposition thermal anneal in order to achieve improved properties. The effect of the post deposition thermal anneal on the optical properties are shown in figure 7-1. The sample consisted of a 100 nm ZnO buffer layer, 10 nm $Zn_{0.80}Mg_{0.20}O$ spacer layers, 15 nm $Zn_{0.80}Mg_{0.20}O$:Al (4.5 at%) donor layers, and 35 nm ZnO active layers. The sample

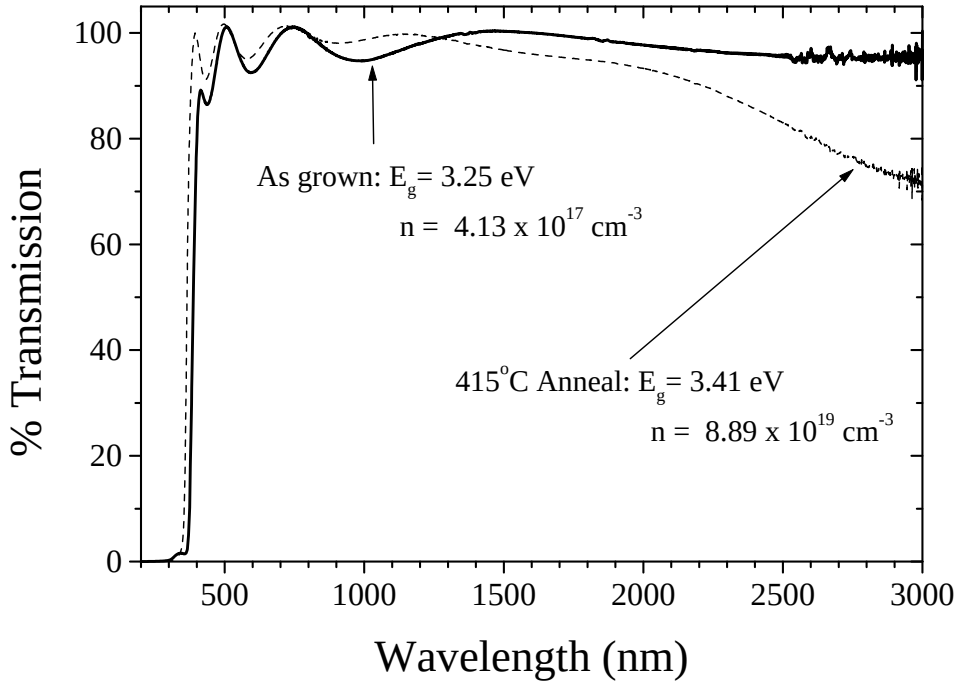

Figure 7-1 Effect of annealing on the optical properties of ZnO/ $Zn_{0.80}Mg_{0.20}O$:Al (4.5 at%)multilayer sample.

contained 5 periods, and was grown in 4.5 mTorr argon and 1.5 mTorr oxygen at 300^{o}C on c-plane sapphire. The anneal was performed at 415^{o}C for 4 hours in a hydrogen (20 SCCM), argon (50 SCCM) atmosphere. Two dramatic features resulting from the anneal were apparent in figure 7-1; the first is the shift of the fundamental absorption edge to lower wavelengths (band gap shift from 3.25 eV to 3.41e eV), and the second was the decreased transmission in the near infrared region. Both of these results were consistent with the two orders of magnitude increase in the free carrier concentration resulting from the anneal, from 4.13 x 10^{17} cm^{-3} to 8.89 x 10^{19} cm^{-3}. The band gap effect was attributed to the well-known Burstein-Moss effect, and the near infrared absorption was attributed to the free carrier resonance effect.[1]

In an attempt to better understand the optical properties of the multilayer films, the electromagnetic transmission spectrum for a multilayer film was compared to the scans of the constituent monolithic layers. The three scans are shown in figure 7-2. The multilayer film consisted of a 100 nm ZnO buffer layer, followed by five periods of a $Zn_{0.80}Mg_{0.20}O$:Al (4.5 at %) (15 nm)/ZnO (55 nm) bilayer. In an attempt to simplify the analysis of the results, the ZnMgO spacer layer was eliminated from this sample. Both the multilayer and the monolithic ZnMgO:Al films were grown and annealed under identical conditions to the film described in figure 7-1. The only processing differences for the monolithic ZnO film were that it was grown at 4 mTorr argon, 1 mTorr oxygen, and that it was annealed at 500^{o}C. The multilayer film displayed optical properties that were a hybrid of the monolithic films. The fundamental absorption edge was close to that of monolithic ZnO, indicating that the multilayer films contained relatively pure ZnO

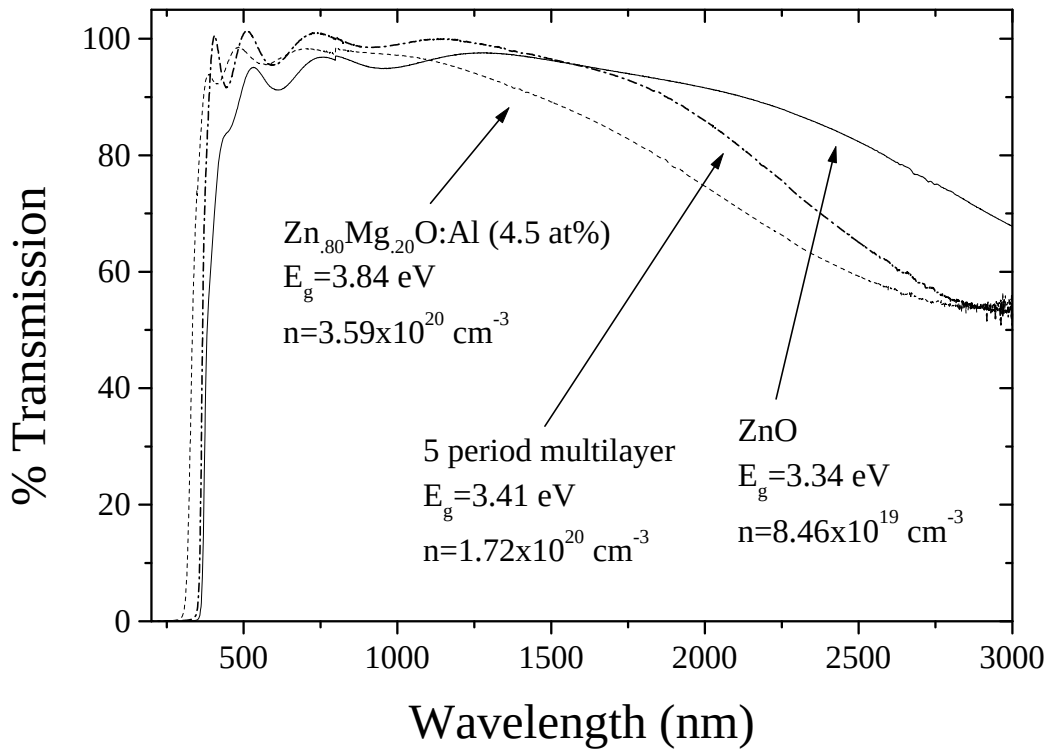

Figure 7-2 Comparison of the optical properties of a 5 period multilayer to monolithic ZnO and $Zn_{0.80}Mg_{0.20}O$:Al (4.5 at %) films.

layers even after the anneal. The free electron absorption at higher wavelengths suggested that the multilayer film also contained layers with higher electron concentrations. At 3000 nm the free carrier absorption of the multilayer film and the monolithic ZnMgO:Al layer were almost identical. The higher transmission of the multilayer compared to the ZnMgO:Al film between 1000 nm and 3000 nm may have been a result of the small thickness (15 nm) of the high carrier concentration layers in the multilayer sample. The overall reduced transmission of the ZnO films between 500 nm and 1500 nm may be a result of the growth at lower oxygen partial pressure, which is known to negatively effect optical transmission by producing oxygen deficient, yellow tinted films.[2] The average free carrier concentration of the multilayer film (1.72×10^{20} cm^{-3}) was consistent with what would be expected from a combination of layers having carrier concentrations similar to the ZnO and ZnMgO:Al monolithic films. The optical absorption coefficients at 2000 nm for the ZnO ($\alpha=2.67x10^{-4}$), the multilayer ($\alpha=3.86x10^{-4}$), and the ZnMgO:Al ($\alpha=7.67x10^{-4}$) films as a function of average carrier concentrations produced a linear plot with a correlation coefficient of .996.

To further investigate the consequences on the optical properties of growing multilayer films, the transmission spectrum for the multilayer film in figure 7-2 was compared to a ZnMgO:Al film that had a similar average carrier concentration. The results are shown in figure 7-3. The ZnMgO:Al film was co-sputtered from a ZnMg alloy target (20 at% Mg) and a ZnAl alloy target (2 wt% Al) both were set at a power of 50 Watts. The c-plane sapphire substrate was heated to 300^{o}C and the deposition was performed in 4 mTorr argon and 1.5 mTorr oxygen. The ZnMgO:Al sample was

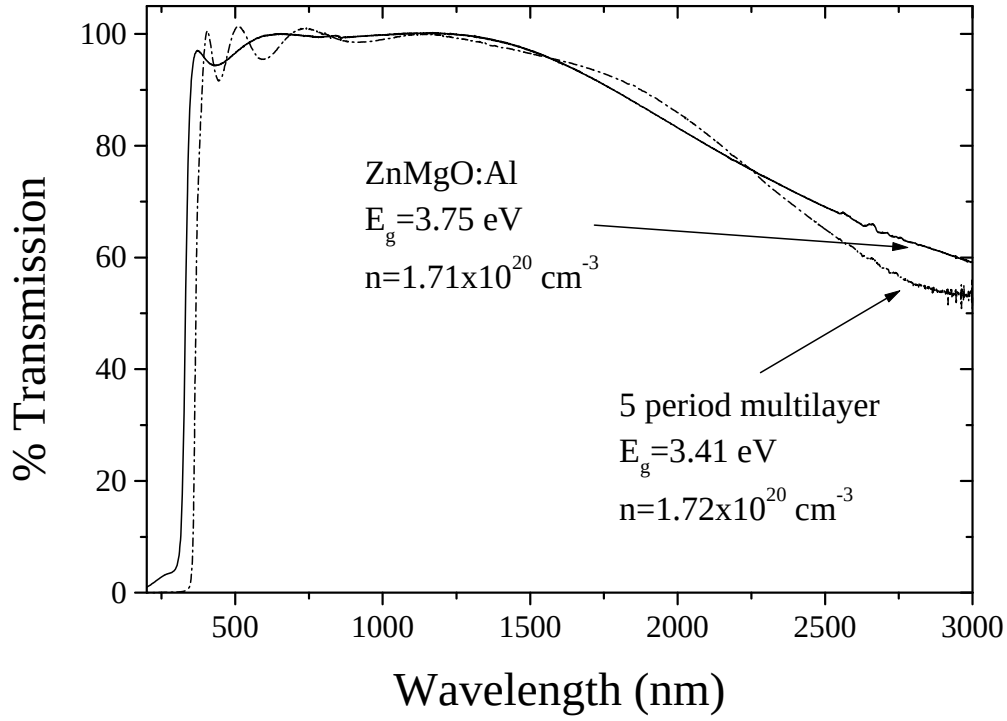

Figure 7-3 Comparison between the optical transmission of a 5 period multilayer film and a ZnMgO:Al monolithic film with similar average carrier concentrations.

annealed at 500^{o}C for for hours in 70% argon, 30% hydrogen at a flow rate of 70 SCCM. The multiayer film and the monolithic film had a similar optical transmission spectrum between 500 nm and 2250 nm; however, the multilayer films showed less transmission at 3000 nm. As mentioned previously, the optical and electrical properties are intimately linked in TCO materials. It is interesting to note that although the transmission spectrum between 500 nm and 2250 nm, and the average carrier concentration were similar for the multilayer and monolithic film, the resistivity of the multilayer films was approximately half of the monolithic film. The multilayer film had a resistivity of 8.93×10^{-4} Ω-cm with an average mobility of 40.7 cm^2/Vs, and the ZnMgO:Al film had a resistivity of 1.74×10^{-3} Ω-cm with a mobility of 20.9 cm^2/Vs. These results suggested that multilayer films could be used to tailor the optical and electrical properties of TCO films in order to maximize the optical transmission while minimizing the electrical resistivity.

7.3. Electrical Properties

Temperature dependent Hall effect measurements were made in an attempt to investigate the effect of using multilayer films on the electrical properties. The properties of multilayer films were compared to those of monolithic films grown of the constituent individual layers. All films were grown at 300^{o}C on c-plane sapphire in an atmosphere of 5.25 mTorr Ar and 0.75 mTorr O_2. The films were annealed at 415^{o}C for 4 hours in H_2 (20 SCCM) and Ar (50 SCCM). The multilayer film was designed to have a 160 nm ZnO buffer layer, followed by 10 periods of: 10 nm $Zn_{0.80}Mg_{0.20}O$ spacer layer, 15 nm $Zn_{0.80}Mg_{0.20}O$:Al (2.4 at %) donor layer, 10 nm $Zn_{0.80}Mg_{0.20}O$ spacer layer, and 35 nm

ZnO active layer. The thickness of the multilayer films was measured to be 1200 nm, indicating that the control of the layer thickness during growth was not precise. The properties of the multilayer were compared to a 992 nm ZnO film and a 385 nm $Zn_{0.80}Mg_{0.20}O$:Al (2.4 at %) film. Figure 7-4 shows the optical transmission data for the three films. At room temperature the multilayer had an average carrier concentration of 1.96×10^{20} cm^{-3}, a mobility of 42.2 cm^2/Vs, and a resistivity of 7.58×10^{-4} Ω-cm. The ZnO had a carrier concentration of 4.2×10^{20} cm^{-3}, a mobility of 27.6 cm^2/Vs, and a resistivity of 5.39×10^{-4} Ω-cm. The $Zn_{0.80}Mg_{0.20}O$:Al (2.4 at %) film had a carrier concentration of 1.56×10^{20} cm^{-3}, a mobility of 5.6 cm^2/Vs, and a resistivity of 7.21×10^{-3} Ω-cm. The dramatic effect of a high carrier concentration on the optical transmission was obvious for the ZnO sample.

The temperature dependent Hall effect data for the same three samples is shown in figure 7-5. For all samples, the carrier concentration was relatively constant over the temperature range tested, which was expected for the highly degenerate samples that were tested. The mobility of the multilayer sample and the ZnO sample increased as the temperature decreased, which indicated that phonon scattering played a role in limiting the mobility at room temperature. The mobility of the multilayer sample increased ~19% over the range of temperatures studied, and the mobility of the ZnO sample increased ~12%. The $Zn_{0.80}Mg_{0.20}O$:Al (2.4 at %) film did not show a mobility increase with a decrease in the temperature, this was presumably a result of the dominance of alloy disorder scattering and the effect of Mg on the effective mass of ZnO, as discussed in chapter 5. The overall effect of decreased temperature on the resistivity was relatively

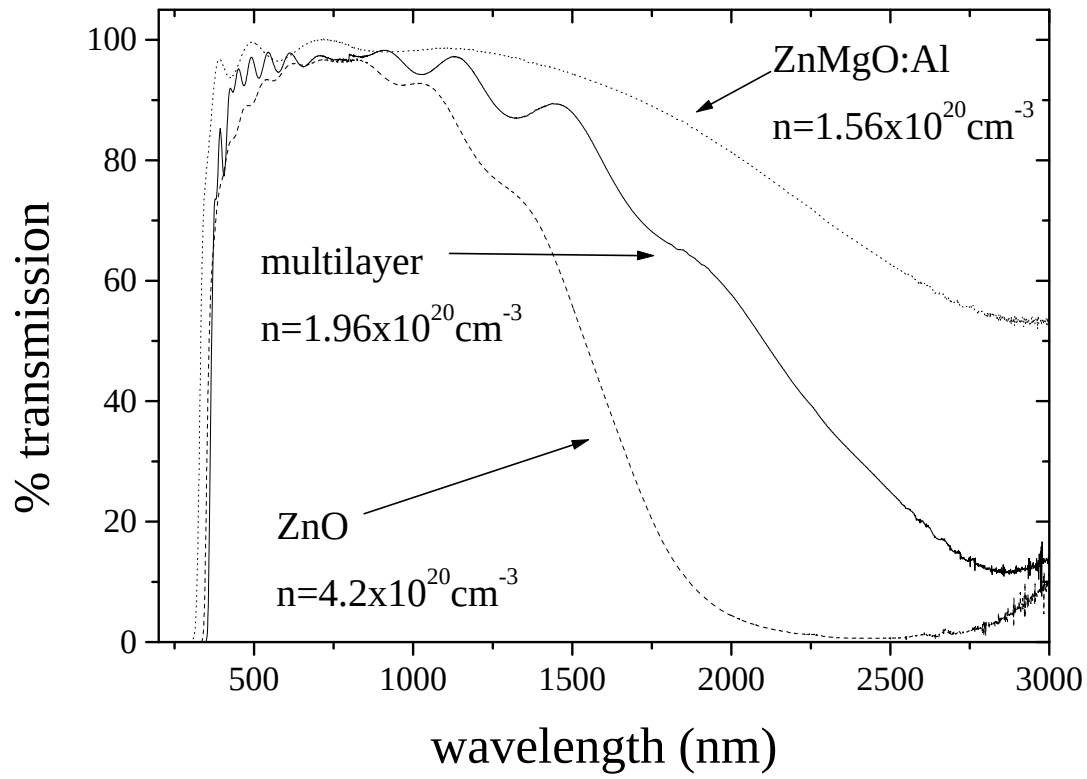

Figure 7-4 Comparison of the optical transmission data from a 10 period multilayer film, a monolithic ZnO film, and a monolithic $Zn_{0.80}Mg_{0.20}O$:Al (2.4 at %) film.

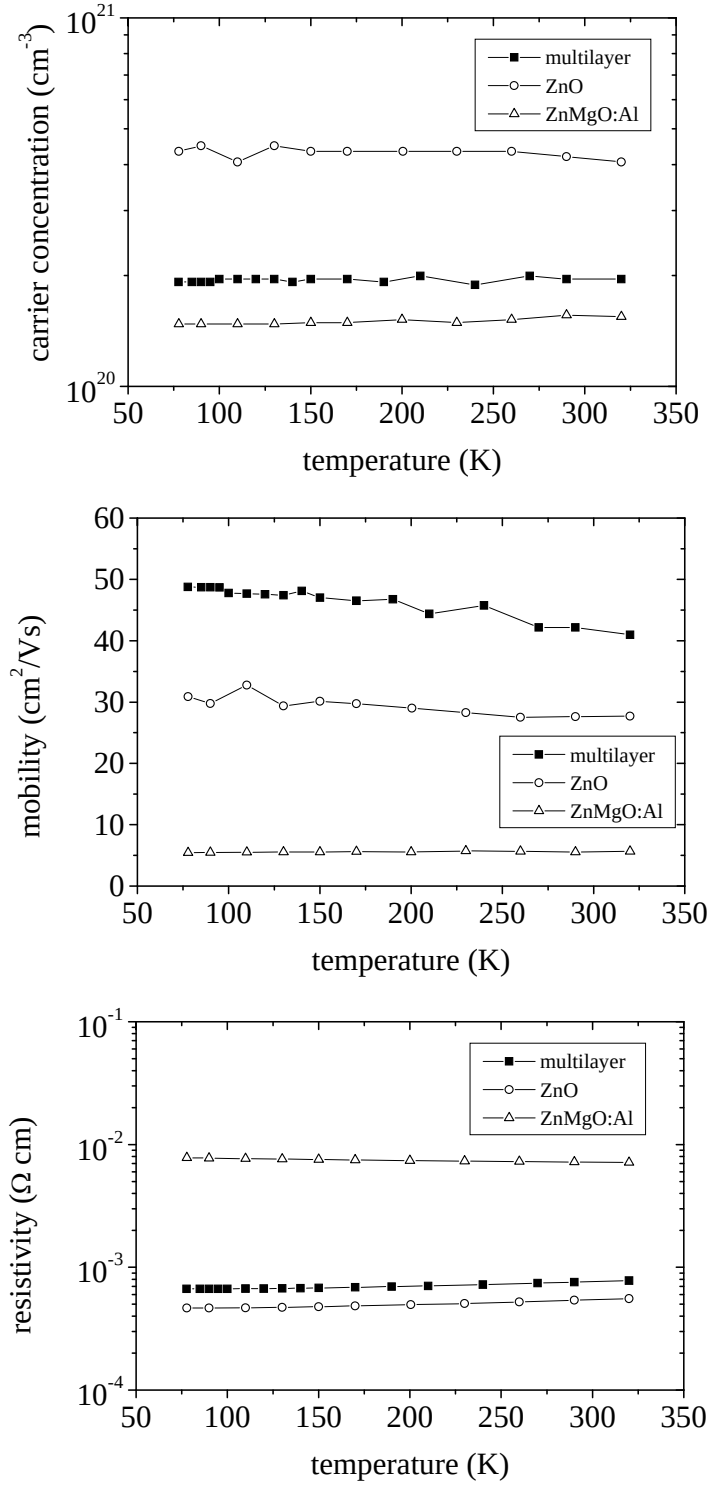

Figure 7-5 Comparison of the temperature dependent Hall effect data for a 10 period multilayer film, a monolithic ZnO film, and a monolithic $Zn_{0.80}Mg_{0.20}O$:Al (2.4 at %) film.

minor for each of the three films, as expected from highly doped, degenerative semiconductor films.[3] The ability to achieve a higher average mobility in the multilayer film was not completely understood, as there was not direct evidence of electron transfer, or the formation of a two-dimensional electron gas. However, the combination of properties possible in multilayer films warranted further investigation.

Based on the theoretical results presented in chapter 6, multilayer films with layer thickness values on the order of 1 nm to 20 nm were grown and characterized. The properties of the multilayer films were compared to those of ZnO, ZnMgO, and ZnMgO:Al monolithic films grown and annealed under the same conditions. The films were grown at a substrate temperature of 300^{o}C on c-plane sapphire, in an atmosphere of 4 mTorr Ar and 1.5 mTorr O_2. All films were annealed for 4 hours at 500^{o}C in an atmosphere of 40% Ar and 30% H_2 at a flow rate of 70 SCCM. ZnO layers were deposited at a target power of 50 W from a zinc target. ZnMgO layers were co-deposited from a zinc target at 50 W, and a ZnMg (20 at%) target at 50 W. ZnMgO:Al layers were co-deposited from a ZnMg (20 at%) target at 50 W, and a ZnAl (2 wt%) target at 50 W. The multilayer films consisted of 5 periods, each period contained a ZnMgO spacer layer, a ZnMgO:Al donor layer, a ZnMgO spacer layer, followed by a ZnO active layer. Based on the results presented in chapter 6, the spacer layers were all designed to be 1 nm thick. The donor layer and the active layer were set at combinations of either 5 nm or 20 nm.

The optical transmission data for the films in this study are shown in figure 7-6. The ability to tune the fundamental absorption edge as well as the near infrared transmission was evident from the scans. The optical scan for the ZnO (5 nm),

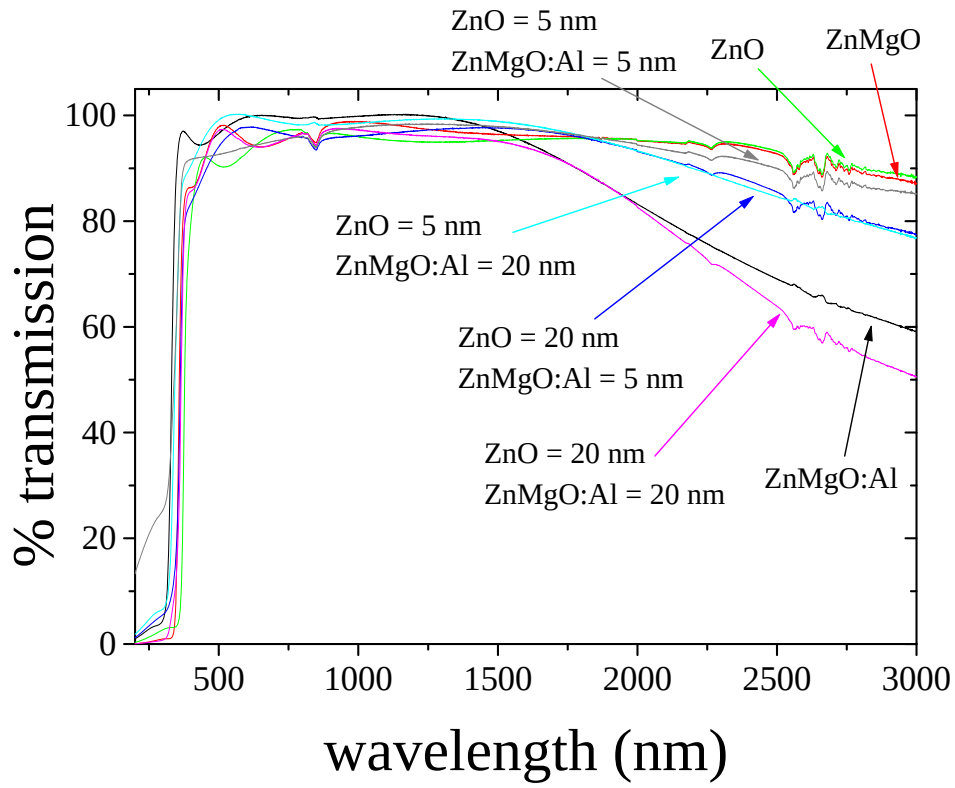

Figure 7-6 Comparison of the optical transmission scans for 5 period multilayer films as a function of layer thickness, and monolithic films of the constituent layers.

ZnMgO:Al (5 nm) multilayer was influenced by the fact that the film was only 68 nm thick, resulting in the tail seen at small wavelengths. The electrical properties of the films were determined using room temperature Hall effect measurements. The electrical data is displayed in figure 7-7 as a function of the bandgap calculated from the optical scan for each film. The data for the monolithic films, shown as open squares, followed the expected trends for ZnO films doped with Mg and Al (see chapter 5). The average carrier concentrations for the multilayer films was higher in samples with small ZnO thickness; however, the free carrier absorption shown in figure 7-6 indicates that the film with 20 nm ZnO and 20 nm ZnMgO:Al has regions with the highest free carrier concentration. The implication is that the electrons are not uniformly distributed throughout the film. The films with 5 nm ZnMgO:Al layers showed higher mobility values than those with 20 nm ZnMgO:Al layers. The low mobility of the ZnMgO:Al layers, resulting from impurity scattering and an increased effective mass (chapter 5), requires that these layers be kept thin in order to achieve a high average mobility. The resistivity was minimized in the multilayer film with 5 nm ZnO layers and 5 nm ZnMgO:Al layers, this film combined the benefits of high carrier concentration with high mobility to outperform any of the monolithic films.

The experimental results shown in figure 7-7 correlate quite well with the theoretical simulation results presented in figure 6-3 and figure 6-4. The simulation with an aluminum concentration of $1x10^{20}$ cm^{-3} was used for comparison based on the experimentally measured carrier concentration for the ZnMgO:Al layer of ~$1.5\ x10^{20}$ cm^{-3} shown in figure 7-7. For the sample with 20 nm ZnO and 5 nm ZnMgO:Al layers

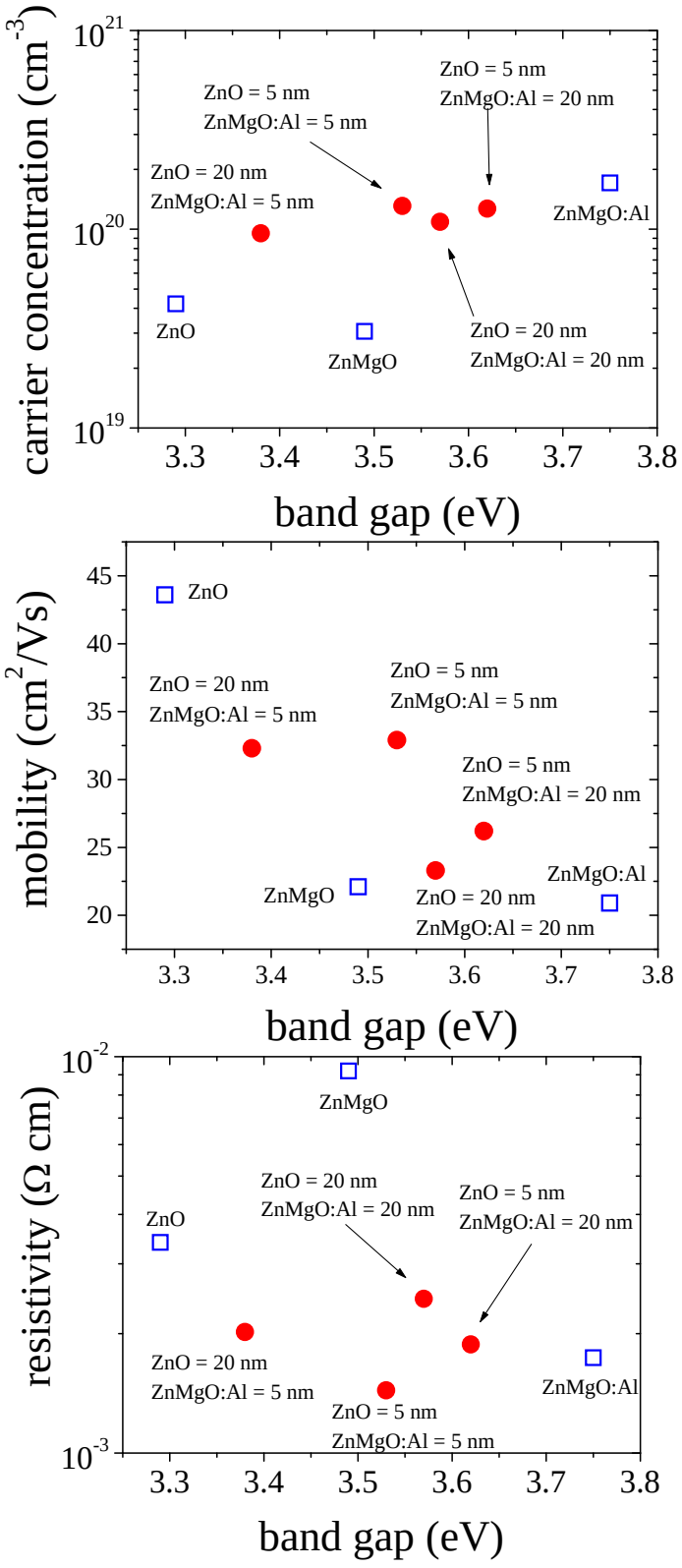

Figure 7-7 Comparison of the electrical data for 5 period multilayer films as a function of layer thickness, and monolithic films of the constituent layers.

the simulation predicted an average mobility of 31.9 cm^2/Vs and a resistivity of $1.08x10^{-2}$ Ωcm, the experimental result where a mobility of 32.3 cm^2/Vs and a resistivity of $2.02x10^{-3}$ Ωcm. For the sample with 5 nm ZnO and 20 nm ZnMgO:Al layers the simulation predicted an average mobility of 11.4 cm^2/Vs and a resistivity of $7.63x10^{-3}$ Ωcm, the experimental result where a mobility of 26.2 cm^2/Vs and a resistivity of $1.88x10^{-3}$ Ωcm. For the sample with 5 nm ZnO and 5 nm ZnMgO:Al layers the simulation predicted an average mobility of 31 cm^2/Vs and a resistivity of $5.36x10^{-2}$ Ωcm, the experimental result where a mobility of 32.9 cm^2/Vs and a resistivity of $1.44x10^{-3}$ Ωcm. The simulations were able to predict both the average mobility and the resistivity in the multilayer films with reasonable accuracy. The theoretical and experimental mobility values for the optimized film with 5 nm ZnO and 5 nm are extremely close.

The results suggested that multilayer TCOs could be used to not only tailor the optical properties, but that electrical properties may be optimized by using thin (~5 nm) layers in a multilayer TCO film. Furthermore, the experimental results suggest that the theoretical calculations presented in chapter 6 can be used to predict and explain the properties of modulation doped multilayaer films. As discussed in section 6.5, the simulations predict higher mobilities for lower doping concentrations in the ZnMgO:Al layers, which has been confirmed experimentally by other groups.

7.4. Structural Properties

The possibility of modulation doping in TCOs to improve optical and electrical properties will require high quality, multilayer films, with precise layer interfaces. The multilayer structure must not only be stable throughout the growth process, but it must also withstand any post deposition processing that is necessary, such as thermal annealing. In this section results are presented from a variety of experiments used to determine the stability of the ZnO/ZnMgO:Al interface.

The first goal was to establish the existence of a multilayer structure, and to investigate the stability of the layers with post deposition annealing. A multilayer sample consisting of a 100 nm ZnO buffer layer followed by five periods of 15 nm of $Zn_{0.80}Mg_{0.20}O$:Al (4.5 at%), and 55 nm of ZnO was grown and annealed for 4 hours at 415^{o}C, in an atmosphere of 70% argon and 30% hydrogen at a flow rate of 70 SCCM. The sample was prepared for cross sectional TEM, and the result is shown in figure 7-8. The layers in the film are clearly visible in the image resulting from the relatively high Mg concentration in the $Zn_{0.80}Mg_{0.20}O$:Al (4.5 at%) layers. The TEM image also clearly showed a strong columnar grain structure in the film, which is typical of ZnO films grown using magnetron sputtering.[2,4] The insert image on figure 7-8 shows the interface between the (Al_2O_3) substrate and the ZnO buffer layer, which appeared smooth and atomically sharp.

In order to further investigate the nature of the multilayer structures, time-of-flight SIMS depth profiling was used to compare as-grown and annealed samples. A qualitative comparison of SIMS depth profiles was presented in figure 4-7 which showed

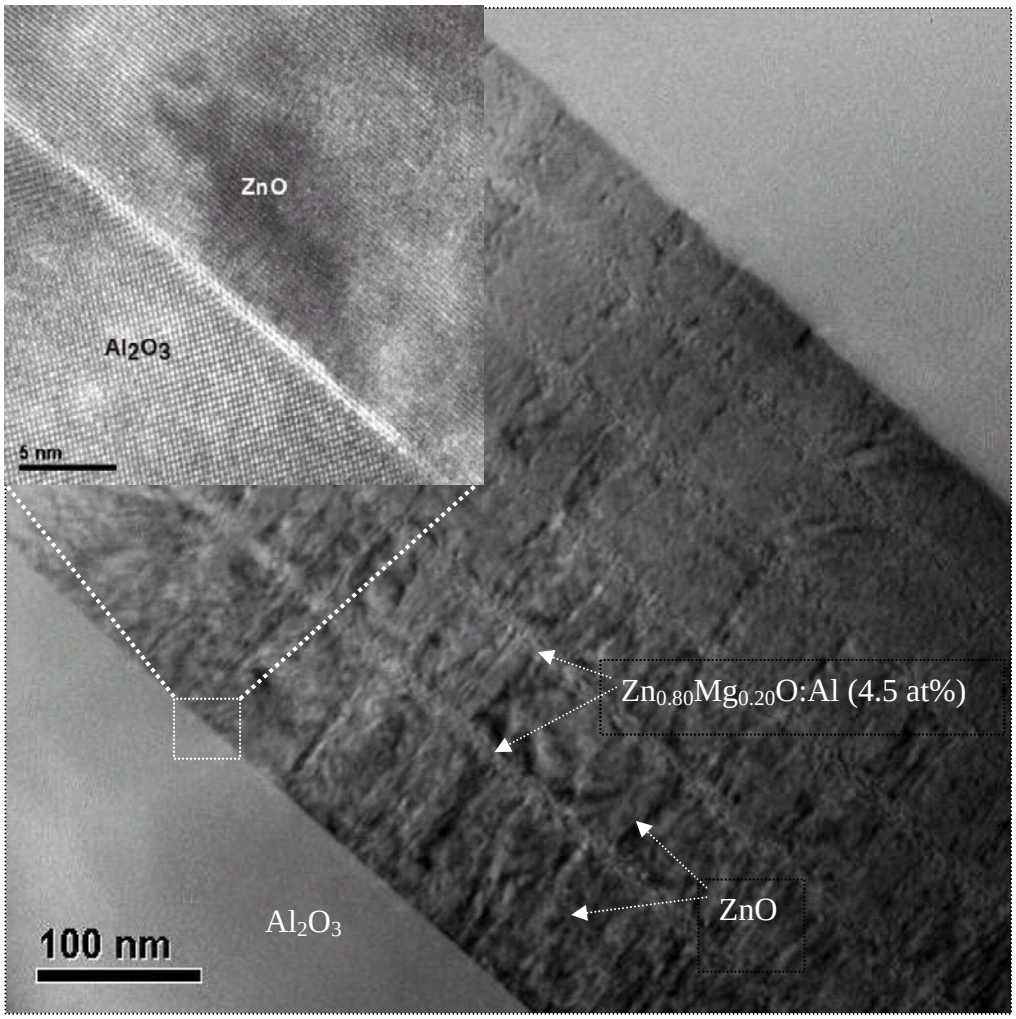

Figure 7-8 TEM image of a ZnO/ZnMgO:Al multilayer structure showing a clear distinction between layers following a post deposition thermal anneal.

that the interfaces were relatively stable for a 350^{o}C anneal, but that substantial interdiffusion occurred for a 500^{o}C anneal. In an attempt to quantify the interdiffusion in the ZnO/ZnMgO system, the SIMS data was modeled to calculate a Mg diffusion coefficient. A multilayer film consisting of 6 periods of 20 nm ZnO and 5 nm $Zn_{0.80}Mg_{0.20}O$:Al was grown and then annealed at 500^{o}C for 4 hours in ambient air. The SIMS data was modeled using an equation that relates the Mg concentration (C_{Mg}) to the position (z) in the multilayer film:[5,6]

$$C_{Mg} = C_0\left\{1-\frac{1}{2}\left[erf\left(\frac{L_z+2z}{4L_d}\right)+erf\left(\frac{L_z-2z}{4L_d}\right)\right]\right\} \quad \text{Equation 7-1}$$

C_0 is the initial Mg concentration in the ZnMgO:Al layers, L_z is the initial ZnMgO:Al layer thickness, and L_d is the Mg diffusion length. The mathematical fits to the experimental data are shown in figure 7-9. The diffusion length calculated before annealing ($L_{d,BA}$) and the diffusion length calculated after annealing ($L_{d,AA}$) were used to calculate the experimental interface broadening ($L_{d,D}$) by using the relationship $L_{d,AA}^2 = L_{d,BA}^2 + L_{d,D}^2$ which yielded a value of $L_{d,D} = 0.65$ nm.[7] A diffusion coefficient for Mg in ZnO of D = 2.8 x 10^{-19} cm^2/s was then calculated using the equation $L_d = \sqrt{Dt}$, where t was the diffusion time.

X-ray diffraction was also used to characterize the structural stability of multilayer films. A multilayer film consisting of 10 periods of 10 nm of ZnO and 5 nm of $Zn_{0.80}Mg_{0.20}O$:Al (6.5 at%) was grown and annealed at 500^{o}C for 4 hours in an

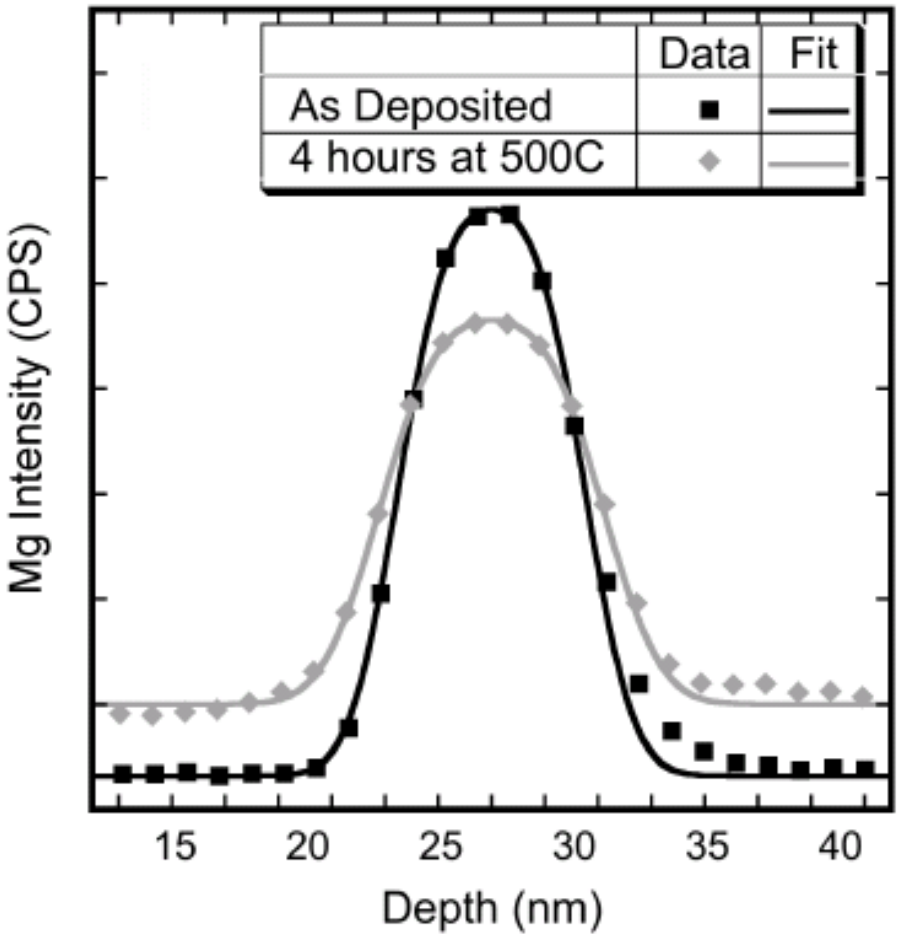

Figure 7-9 SIMS depth profile data for a ZnO/ZnMgO:Al multilayer as grown and after a thermal anneal. Mathematical fit of the data based on equation 7-1 is also shown in the figure.

atmosphere of 70% Ar and 30% H_2 at 70 SCCM. The high angle θ–2θ scans are shown in figure 7-10. The as deposited film showed clear satellite peaks indicative of a multilayer structure; however, the satellite peaks were no longer discernable after the anneal. Since the high angle reflections are influenced by crystal orientation, defect concentration as well as interface width changes alternate methods were sought to analyze the films using XRD. Low angle x-ray reflectivity was used to investigate the interface diffusion because the nature of the film crystal quality does not influence the reflectivity peaks, it is the contrast in the scattering density between the layers that causes the scattering and the resultant reflectivity peaks.[8] Figure 7-11 shows the low angle reflectivity scans for the sample as grown and annealed samples as well as a theoretical model based on Parratt's recursive method.[8] The superlattice reflections are clearly visible for both the as grown and the annealed sample. The reflection peaks agreed well with those predicted from Parratt's method using a ZnO thickness of 11 nm and a $Zn_{0.80}Mg_{0.20}O$:Al (6.5 at%) thickness of 5 nm.

A subsequent study was performed with an identical multilayer; however, the sample was annealed in ambient air rather than an Ar/H_2 atmosphere. Low angle reflectivity scans were performed after different annealing times, and the rate of change of the m=1 satellite peak intensity (I_m) was used to calculate the interdiffusion coefficient ($\tilde{D}$) using the relationship:[9,10]

$$\frac{d}{dt}(\ln I_m) = -2\tilde{D}\left(\frac{2\pi m}{\Lambda}\right)^2 \qquad \text{Equation 7-2}$$

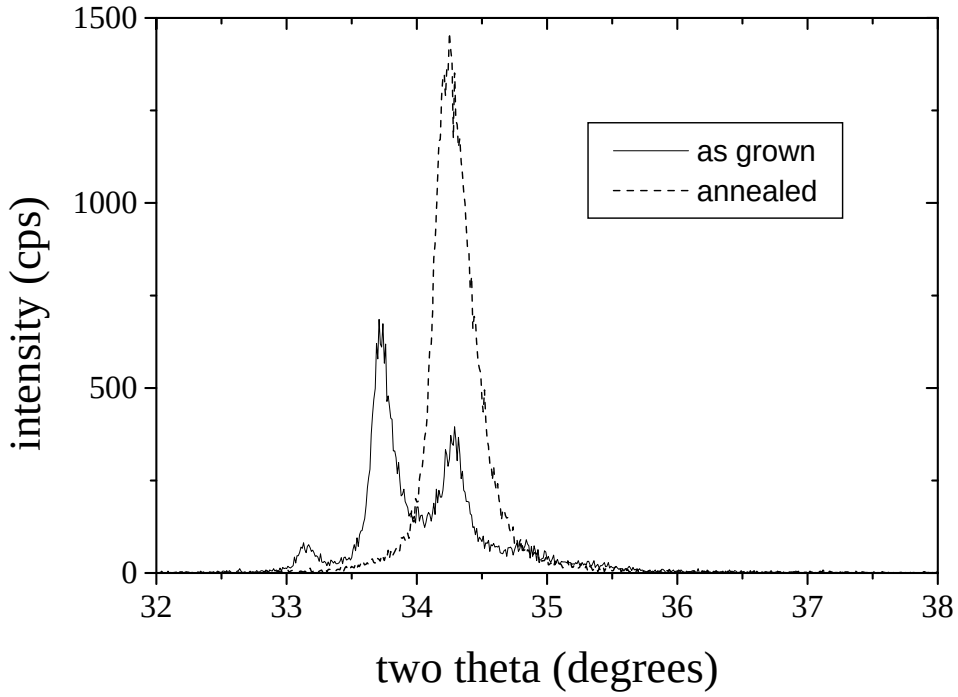

Figure 7-10 High angle x-ray diffraction data for a 10 period multilayer showing the loss of satellite peaks as a result of the post deposition anneal.

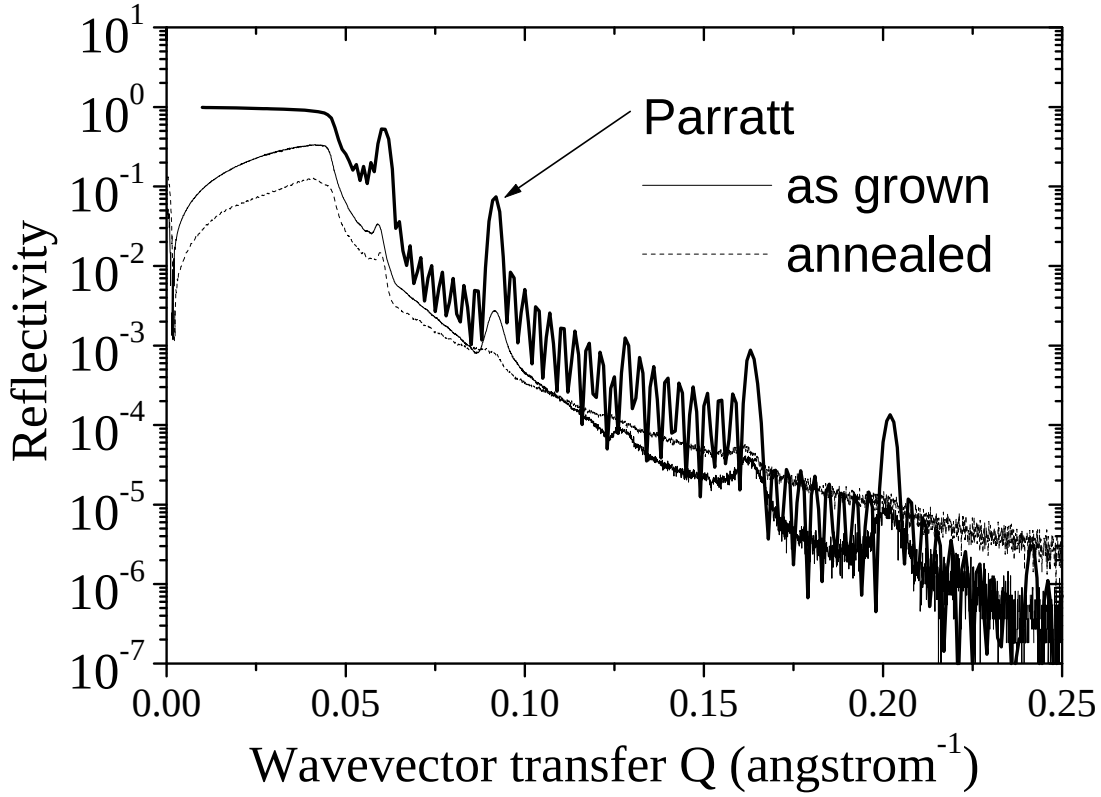

Figure 7-11 Comparison of the low angle x-ray reflectivity scans for a 10 period ZnO/ZnMgO:Al multilayer. A theoretical scan calculated using Parratt's recursive method is also shown.

In the equation, *t* is the annealing time, *m* is the satellite peak number, and Λis the period of the multilayer. Figure 7-12a shows the change in intensity of the m=1 satellite peak with increasing annealing time, and figure 7-12b shows the linearized plot used to calculate the diffusion coefficient of Mg in the multilayer films. The analysis of the data showed two distinct behaviors for the diffusion, an initial fast diffusion regime followed by a slower late stage diffusion regime. The average of the fast regime diffusion coefficient for three different samples was calculated to be 5.5×10^{-18} cm^2/sec, and the average diffusion coefficient for the slow regime was 1.7×10^{-19} cm^2/sec. The fast regime is attributed to defect enhanced diffusion, which is thought to be a byproduct of the dynamic nature of the reactive sputtering deposition method. Other researchers have suggested smaller diffusion coefficients for Mg in ZnO/ZnMgO multilayers grown by molecular beam epitaxy,[11,12] which may have been the result of lower defect densities.

Multilayer ZnO/ZnMgO:Al structure were successful grown and the modulated structure was confirmed using SIMS and TEM. Significant interfacial diffusions began at annealing temperatures above ~400^{o}C. Low angle XRD reflectivity peaks were used to calculate diffusion coefficients for an annealing temperature of 500 ^{o}C, and it was seen that two diffusion regimes existed for Mg in the multilayer samples; an initial fast diffusion regime followed by slower diffusion at longer times.

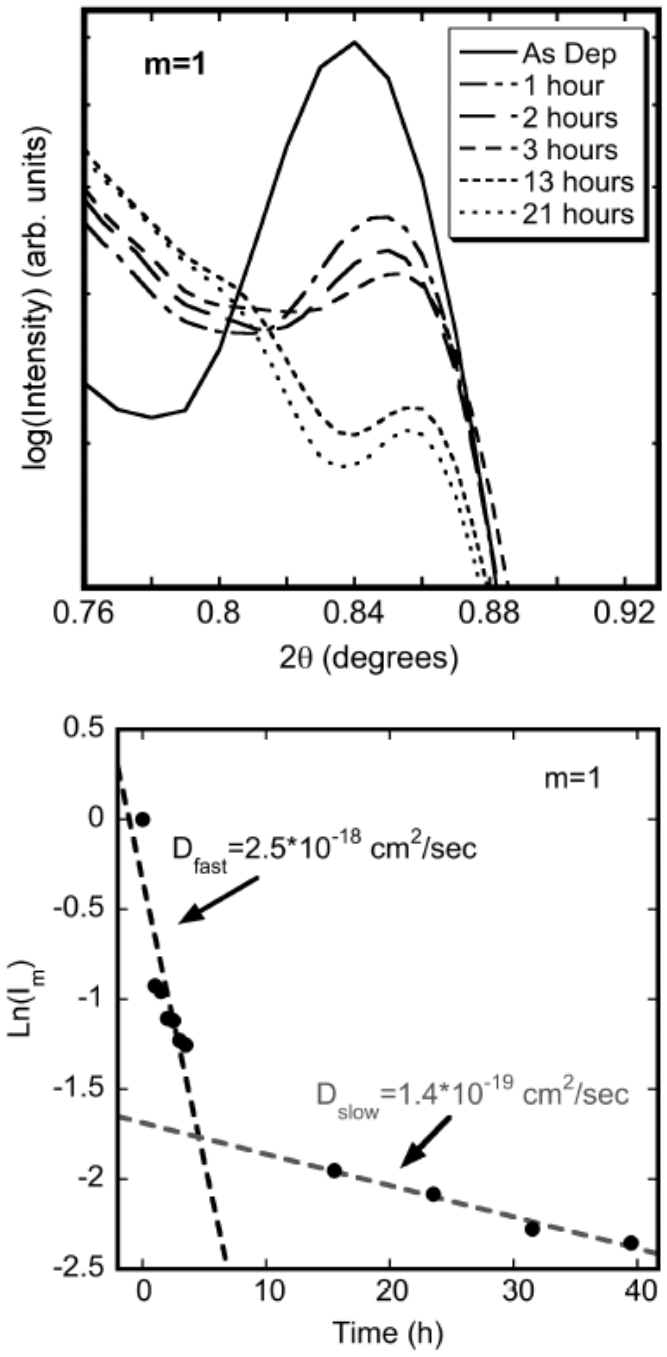

Figure 7-12 (a) m=1 satellite peak intensity change with increasing annealing time for a 10 period ZnO/ZnMgO:Al multilayer. (b) Linearized plots used to calculate the Mg diffusion coefficient in the multilayer film.

Chapter 8

Thesis Conclusions

8.1. Conclusions

The original inspiration for the work in this thesis was to take the proven technology of modulation doping from III-V semiconductors, and apply it to the unique filed of transparent conducting oxides. Although the concept was clear, there were many technological hurdles to overcome in an attempt to successfully produce multilayer TCOs. The work in this thesis advanced the state of knowledge concerning the fundamental material properties in the ZnO/ZnMgO:Al system, as well as tackling several important issues relevant to using these materials in multilayer structures. The following conclusions have been made based on the work in this thesis:

1. Experimental conditions were found to optimize the growth of ZnO based materials using reactive magnetron sputtering (~25% oxygen during growth). Crystal quality and surface morphology were tailored in order to grow films that are appropriate for multilayer structures.

2. Post deposition thermal annealing conditions were optimized to improve the electrical properties of ZnO based films (415^{o}C, for 4 hours, in 20 SCCM hydrogen and 50 SCCM argon). The structural and optical properties were also considered, as well as the effect of annealing of multilayer structures.

3. An extensive study of ZnMgO:Al was conducted. The ranges of electrical, optical, and structural properties achievable as a function of doping levels were reported (carrier concentrations of $1x10^{20}$ cm^{-3} were achieved). Insights into the relevant scattering mechanisms were made, and the usefulness of these films in multilayer structures was considered.

4. Theoretical simulations were performed to shed light on the possibility of using the technique of modulation doping for TCOs. Optimum layer thickness values (5 nm), and doping levels were suggested.

5. Multilayer films were grown and characterized based on their optical, electrical, and structural properties. The experimental results showed reasonable agreement with the theoretical simulations. The stability of the ZnO/ZnMgO:Al interface was investigated and a diffusion coefficient was calculated.

8.2. Suggestions for Future Work

The dynamic nature of reactive magnetron sputtering and the geometrical limitations of the growth chamber used in this work made it very difficult to achieve truly reproducible results. The use of a growth technique such as MBE for the multilayer films would greatly increase the ability to control layer thickness and doping levels. The

ability of MBE to produce atomically sharp interfaces may also make it possible to achieve electron confinement in multilayer films.

Understanding the capital investment required for MBE, there still remains room for the optimization of multilayer films grown by sputtering. The results presented in the current work suggest that interesting combinations of properties can be achieved in multilayer films by adjusting the film parameters.

The effect of post deposition annealing also requires more attention. Based on the significant influence of annealing in determining the electrical properties, different atmospheres, times, and temperatures should still be investigated.

The role TCOs promise to play in future technologies such as displays, transparent electronics, and renewable energy justifies further research into the optimization of their properties.

References

Chapter 1

[1] K. Badeker, Ann. Phys. **22,** 749 (1907).

[2] M. Ohring, *The Materials Science of Thin Films* (Academic Press, Boston, 1992).

[3] D. S. Ginley and C. Bright, *Transparent Conducting Oxides*, MRS Bull. **25,** 15-18 (2000).

[4] B. G. Lewis and D. C. Paine, *Applications and Processing of Transparent Conducting Oxides*, MRS Bulletin **25,** 22-27 (2000).

[5] H. Kawazoe, H. Yanagi, K. Ueda, and H. Hosono, *Transparent p-Type Conducting Oxides: Design and Fabrication of p-n Heterojunctions*, MRS Bulletin **25,** 28-36 (2000).

[6] T. Minami, *New n-type transparent conducting oxides*, MRS Bulletin **25,** 38-44 (2000).

[7] A. J. Freeman, K. R. Poeppelmeier, T.O. Mason, R. P. H. Chang, and T. J. Marks, *Chemical and Thin-Film Strategies for New Transparent Conducting Oxides*, MRS Bulletin **25,** 45-51 (2000).

[8] R. G. Gordon, *Criteria for Choosing Transparent Conductors*, MRS Bulletin **25,** 52-57 (2000).

[9] T. J. Coutts, D. L. Young, and X. Li, *Characterization of transparent conducting oxides*, MRS Bulletin **25,** 58-65 (2000).

[10] B. Rech and H. Wagner, *Potential of amorphous silicon for solar cells*, Applied Physics A: Materials Science & Processing **69,** 155-167 (1999).

[11] T. Minemoto, T. Negami, S.Nishiwaki, H. Takakura, and Y. Hamakawa, *Preparation of $Zn_{1-x}Mg_xO$ films by radio frequency magnetron sputtering*, Thin Solid Films **372,** 173-176 (2000).

[12] A. Ohtomo and M. Kawasaki, *Novel semiconductor technologies of ZnO films towards ultraviolet LEDs and invisible FETs*, IEICE Transactions on Electronics **E83C,** 1614-1617 (2000).

[13] J. F. Wager, *Transparent electronics*, Science **300,** 1245-1246 (2003).

[14] K. Nomura, H. Ohta, K. Ueda, T. Kamiya, M. Hirano, and H. Hosono, *Thin-film transistor fabricated in single-crystalline transparent oxide semiconductor*, Science **300,** 1269-1272 (2003).

[15] E. Fortunato, A. Pimentel, L. Pereira, A. Goncalves, G. Lavareda, H. Aguas, I. Ferreira, C. N. Carvalho, and R. Martins, *High field-effect mobility zinc oxide thin film transistors produced at room temperature*, Journal of Non-Crystalline Solids **338-40,** 806-809 (2004).

[16] H. L. Hartnagel, A. L. Dawar, A. K. Jain, and C. Jagadish, *Semiconducting Transparent Thin Films* (London, 1995).

[17] K. L. Chopra, S. Major, and D. K. Pandya, *Transparent Conductors-A Status Review*, Thin Solid Films **102,** 1-46 (1983).

[18] E. Burstein, *Anomalous optical absorption limit in InSb*, Physical Review **93,** 632-633 (1954).

[19] L. Solymar and D. Walsh, *Electrical Properties of Materials*, sixth ed. (Oxford University Press, Oxford, 1998).

[20] G. Parker, *Introductory Semiconductor Device Physics* (Institute of Physics Publishing, Bristol, 2004).

[21] N. Ashcroft and N. Mermin, *Solid State Physics* (Thomson Learning, Inc., 1976).

[22] S. Sindhu, K. N. Rao, S. Ahuja, A. Kumar, and E. S. R. Gopal, *Spectral and optical performance of electrochromic poly(3,4-ethylenedioxythiophene) (PEDOT) deposited on transparent conducting oxide coated glass and polymer substrates*, Materials Science and Engineering B-Solid State Materials for Advanced Technology **132,** 39-42 (2006).

[23] A. Wang, J. R. Babcock, N. L. Edleman, A. W. Metz, M. A. Lane, R. Asahi, V. P. Dravid, C. R. Kannewurf, A. J. Freeman, and T. J. Marks, *Indium-cadmium-oxide films having exceptional electrical conductivity and optical transparency: Clues for optimizing transparent conductors*, APPLIED PHYSICAL SCIENCES **98,** 7113-7116 (2001).

[24] G. Gordillo, M. Grizalez, L. C. Moreno, and F. Landazabal, *Influence of the optical window on the performance of TCO/CdS/CdTe solar cells*, Physica Status Solidi B-Basic Research **220,** 215-219 (2000).

[25] B. Rech, O. Kluth, T. Repmann, T. Roschek, J. Springer, J. Muller, F. Finger, H. Stiebig, and H. Wagner, *New materials and deposition techniques for highly efficient silicon thin film solar cells,* Solar Energy Materials and Solar Cells **74,** 439-447 (2002).

[26] J. Owen, M. S. Son, K. H. Yoo, B. D. Ahn, and S. Y. Lee, *Organic photovoltaic devices with Ga-doped ZnO electrode,* Applied Physics Letters **90** (2007).

[27] S. N. Alamri, *Effect of transparent conductive oxide stability on CdS/CdTe solar cell performance*, Japanese Journal of Applied Physics Part 2-Letters **41,** L1052-L1054 (2002).

[28] A. Ohtomo, M. Kawasaki, T. Koida, K. Masubuchi, H. Koinuma, Y. Sakurai, Y. Yoshida, T. Yasuda, and Y. Segawa, *$Mg_xZn_{1-x}O$ as a II-VI widegap semiconductor allloy,* Applied Physics Letters **72,** 2466-2468 (1998).

[29] T. Makino, Y. Segawa, M. Kawasaki, A. Ohtomo, R. Shiroki, K. Tamura, T. Yasuda, and H. Koinuma, *Band gap engineering based on MgxZn1-xO and CdyZn1-yO ternary alloy films,* Applied Physics Letters **78,** 1237-1239 (2001).

[30] D. S. Kim, S. J. Park, E. K. Jeong, H. K. Lee, and S. Y. Choi, *Optical and electrical properties of p-type transparent conducting CuAlO2 thin film,* Thin Solid Films **515,** 5103-5108 (2007).

[31] Y. X. Huang, Z. G. Ji, and C. Chen, *Preparation and characterization of p-type transparent conducting tin-gallium oxide films,* Applied Surface Science **253,** 4819-4822 (2007).

[32] H. D. Sun, T. Makino, N. T. Tuan, Y. Segawa, Z. K. Tang, G. K. L. Wong, M. Kawasaki, A. Ohtomo, K. Tamura, and H. Koinuma, *Stimulated emission induced by exciton-exciton scattering in ZnO/ZnMgO multiquantum wells up to room temperature,* Applied Physics Letters **77,** 4250-4252 (2000).

[33] T. Gruber, C. Kirchner, R. Kling, F. Reuss, and A. Waag, *ZnMgO epilayers and ZnO-ZnMgO quantum wells for optoelectronic applications in the blue and UV spectral region,* Appl. Phys. Lett. **84,** 5359-5361 (2004).

[34] V. A. Coleman and C. Jagadish, *Zinc Oxide Bulk, Thin Films and Nanostructures* (Elsevier, Amsterdam, 2006).

[35] C. Klingshirn, *ZnO: Material, physics and applications,* Chemphyschem **8,** 782-803 (2007).

[36] D. C. Look, in *Zinc Oxide Materials and Devices II*; *Vol. 6474*, edited by F. H. Teherani and C. W. Litton (2007).

[37] S. Uthanna, T. K. Subramanyam, B. S. Naidu, and G. M. Rao, *Structure-composition-property dependence in reactive magnetron sputtered ZnO thin films*, Optical Materials **19,** 461-469 (2002).

[38] S. Bloom and Ortenbur.I, *Pseudopotential Band-Structure of Zno*, Physica Status Solidi B-Basic Research **58,** 561-566 (1973).

[39] J. R. Chelikowsky, *Oxygen Pseudopotential - Application to Electronic-Structure of Zno*, Solid State Communications **22,** 351-354 (1977).

[40] A. Kobayashi, O. F. Sankey, S. M. Volz, and J. D. Dow, *Semiempirical Tight-Binding Band Structures of Wurtzite Semiconductors - Aln, Cds, Cdse, Zns, and Zno*, Physical Review B **28,** 935-945 (1983).

[41] C. K. Yang and K. S. Dy, *Band-Structure of Zno Using the Lmto Method*, Solid State Communications **88,** 491-494 (1993).

[42] O. K. Andersen, *Linear Methods in Band Theory*, Physical Review B **12,** 3060-3083 (1975).

[43] M. Usuda, N. Hamada, T. Kotani, and M. van Schilfgaarde, *All-electron GW calculation based on the LAPW method: Application to wurtzite ZnO*, Physical Review B **66** (2002).

[44] D. Vogel, P. Kruger, and J. Pollmann, *Ab-Initio Electronic-Structure Calculations for Ii-Vi Semiconductors Using Self-Interaction-Corrected Pseudopotentials*, Physical Review B **52,** 14316-14319 (1995).

[45] P. Erhart, K. Albe, and A. Klein, *First-principles study of intrinsic point defects in ZnO: Role of band structure, volume relaxation, and finite-size effects*, Physical Review B **73** (2006).

[46] Q. B. Ma, Z. Z. Ye, H. P. He, L. P. Zhu, J. R. Wang, and B. H. Zhao, *Influence of Ar/O-2 ratio on the properties of transparent conductive ZnO: Ga films prepared by DC reactive magnetron sputtering*, Materials Letters **61,** 2460-2463 (2007).

[47] M. K. Puchert, P. Y. Timbrell, and R. N. Lamb, *Postdeposition annealing of radio frequency magnetron sputtered ZnO films*, Journal of Vacuum Science and Technology A **14,** 2220-2230 (1996).

[48] E. Mirica, G. Kowach, P. Evans, and H. Du, *Morphological evolution of ZnO thin films deposited by reactive sputtering*, Crystal Growth & Design **4,** 147-156 (2004).

[49] J. Mass, P. Bhattacharya, and R. S. Katiyar, *Effect of high substrate temperature on Al-doped ZnO thin films grown by pulsed laser deposition*, Materials Science and Engineering B-Solid State Materials for Advanced Technology **103,** 9-15 (2003).

[50] V. Craciun, J. Perriere, N. Bassim, R. K. Singh, D. Craciun, and J. Spear, *Low-temperature growth of epitaxial ZnO films on (001) sapphire by ultraviolet-assisted pulsed laser deposition*, Applied Physics A **69,** S531-S533 (1999).

[51] D. Gerthsen, D. Litvinov, T. Gruber, C. Kirchner, and A. Waag, *Origin and consequences of a high stacking fault density in epitaxial ZnO layers*, Applied Physics Letters **81,** 3972-3974 (2002).

[52] J. L. vanHeerden and R. Swanepoel, *XRD analysis of ZnO thin films prepared by spray pyrolysis*, Thin Solid Films **299,** 72-77 (1997).

[53] M. A. L. Johnson, S. Fujita, W. H. Rowland, W. C. Hughes, J. W. Cook, and J. F. Schetzina, *MBE growth and properties of ZnO on sapphire and SiC substrates*, Journal of Electronic Materials **25,** 855-862 (1996).

[54] P. Fons, K. Iwata, S. Niki, A. Yamada, and K. Matsubara, *Growth of high-quality epitaxial ZnO films on alpha-Al2O3*, Journal of Crystal Growth **202,** 627-632 (1999).

[55] R. Ondo-Ndong, F. Pascal-Delannoy, A. Boyer, A. Giani, and A. Foucaran, *Structural properties of zinc oxide thin films prepared by r.f. magnetron sputtering*, Materials Science and Engineering B **97,** 68-73 (2003).

[56] S. Yamauchi, H. Handa, A. Nagayama, and T. Hariu, *Low temperature epitaxial growth of ZnO layer by plasma-assisted epitaxy*, Thin Solid Films **345,** 12-17 (1999).

[57] Y. Igasaki and H. Saito, *The effects of deposition rate on the structural and electrical properties of ZnO:All films deposited on (11-20) oriented sapphire substrates*, Journal of Applied Physics **70,** 3613-3619 (1991).

[58] I. S. Kim, S. H. Jeong, and B. T. Lee, *Growth and characterization of high quality homoepitaxial ZnO films by RF magnetron sputtering*, Semiconductor Science and Technology **22,** 683-686 (2007).

[59] R. J. Hong, K. Helming, X. Jiang, and B. Szyszka, *Texture analysis of Al-doped ZnO thin films prepared by in-line reactive MF magnetron sputtering*, Applied Surface Science **226,** 378-386 (2004).

[60] J. Narayan, K. Dovidenko, A. K. Sharma, and S. Oktyabrsky, *Defects and interfaces in epitaxial ZnO/ a-Al2O3 and AlN/ZnO/ a-Al2O3 heterostructures*, JOURNAL OF APPLIED PHYSICS **84,** 2597-2601 (1998).

[61] J. Narayan and B. C. Larson, *Domain epitaxy: A unified paradigm for thin film growth*, Journal of Applied Physics **93,** 278-285 (2003).

[62] F. Vigue, C. Deparis, P. Vennegues, S. Vezian, M. Laugt, P. Lorenzini, C. Morhain, F. Raymond, J. Guion, and J. P. Faurie, *2D versus 3D growth mode in ZnO layers grown by plasma-enhanced molecular beam epitaxy on (0001) sapphire*, Physica Status Solidi B-Basic Research **229,** 931-934 (2002).

[63] H. B. Kang, K. Nakamura, S. H. Lim, and D. Shindo, *Epitaxial growth of ZnO films on (0001) sapphire at low temperatures by electron cyclotron resonance-assisted molecular beam epitaxy and their microstructural characterizations*, Japanese Journal of Applied Physics Part 1-Regular Papers Short Notes & Review Papers **37,** 781-785 (1998).

[64] I. Ohkubo, A. Ohtomo, T. Ohnishi, Y. Mastumoto, H. Koinuma, and M. Kawasaki, *In-plane and polar orientations of ZnO thin films grown on atomically flat sapphire*, Surface Science **443,** L1043-L1048 (1999).

[65] S. I. Park, T. S. Cho, S. J. Doh, J. L. Lee, and J. H. Je, *Structural evolution of ZnO/sapphire(001) heteroepitaxy studied by real time synchrotron x-ray scattering*, Applied Physics Letters **77,** 349-351 (2000).

[66] V. Srikant, V. Sergo, and D. R. Clarke, *Epitaxial Aluminum-Doped Zinc-Oxide Thin-Films on Sapphire .1. Effect of Substrate Orientation*, Journal of the American Ceramic Society **78,** 1931-1934 (1995).

[67] J.-H. Jou, M.-Y. Han, and D.-J. Cheng, *Substrate dependent internal stress in sputtered zinc oxide thin films*, Journal of Applied Physics **71,** 4333-4336 (1992).

[68] T. Nakamura, H. Minoura, and H. Muto, *Fabrication of ZnO(0001) epitaxial films on the cubic(111) substrate with C_6 symmetery by pulsed laser ablation*, Thin Solid Films **405,** 109-116 (2002).

[69] E. Bellingeri, D. MarrÃ©, I. Pallecchi, L. Pellegrino, and A. S. Siri, *High mobility in ZnO thin films deposited on perovskite substrates with a low temperature nucleation layer.*, Applied Physics Letters **86,** N.PAG (2005).

[70] J. A. Thornton, *High-Rate Thick-Film Growth*, Annual Review of Materials Science **7,** 239-260 (1977).

[71] J. A. Thornton, *The Microstructure of Sputter-Deposited Coatings*, Journal of Vacuum Science & Technology a-Vacuum Surfaces and Films **4,** 3059-3065 (1986).

[72] E. Mirica, G. Kowach, and H. Du, *Modified Structure Zone Model to describe the morphological evolution of ZnO thin films deposited by reactive sputtering*, Crystal Growth & Design **4,** 157-159 (2004).

[73] D. M. Mattox, *Particle Bombardment Effects on Thin-Film Deposition - a Review*, Journal of Vacuum Science & Technology A **7,** 1105-1114 (1989).

[74] K. Nakahara, T. Tanabe, H. Takasu, P. Fons, K. Iwata, A. Yamada, K. Matsubara, R. Hunger, and S. Niki, *Growth of undoped ZnO films with improved electrical properties by radical source molecular beam epitaxy*, Japanese Journal of Applied Physics Part 1-Regular Papers Short Notes & Review Papers **40,** 250-254 (2001).

[75] M. Chen, Z. L. Pei, X. Wang, C. Sun, and L. S. Wen, *Structural, electrical, and optical properties of transparent conductive oxide ZnO:Al films prepared by dc magnetron reactive sputtering*, Journal of Vacuum Science and Technology A **19,** 963-970 (2001).

[76] A. Sarkar, S. Ghosh, S. Chaudhuri, and A. K. Pal, *Studies on Electron-Transport Properties and the Burstein-Moss Shift in Indium-Doped Zno Films*, Thin Solid Films **204,** 255-264 (1991).

[77] P. Nunes, E. Fortunato, P. Tonello, F. B. Fernandes, P. Vilarinho, and R. Martins, *Effect of different dopant elements on the properties of ZnO thin films*, Vacuum **64,** 281-285 (2002).

[78] A. Sanchez-Juarez, A. Tiburcio-Silver, A. Ortiz, E. P. Zironi, and J. Rickards, *Electrical and optical properties of fluorine-doped ZnO thin films prepared by spray pyrolysis*, Thin Solid Films **333,** 196-202 (1998).

[79] D. Chattopadhyay and H. J. Queisser, *Electron-Scattering by Ionized Impurities in Semiconductors*, Reviews of Modern Physics **53,** 745-768 (1981).

[80] K. Ellmer, *Resistivity of polycrystalline zinc oxide films: current status and physical limit*, J. Phys. D **34,** 3097-3108 (2001).

[81] V. Srikant, V. Sergo, and D. R. Clarke, *Epitaxial Aluminum-Doped Zinc-Oxide Thin-Films on Sapphire .2. Defect Equilibria and Electrical-Properties*, Journal of the American Ceramic Society **78,** 1935-1939 (1995).

[82] R. B. H. Tahar and N. B. H. Tahar, *Mechanism of carrier transport in aluminum-doped zinc oxide*, JOURNAL OF APPLIED PHYSICS **92,** 4498-4501 (2002).

[83] D. H. Zhang and H. L. Ma, *Scattering mechanisms of charge carriers in transparent conducting oxide films*, Applied Physics a-Materials Science & Processing **62,** 487-492 (1996).

[84] T. Makino, Y. Segawa, A. Tsukazaki, A. Ohtomo, and M. Kawasaki, *Majority-carrier mobilities in undoped and n-type doped ZnO epitaxial layers*, Phys. Stat. Sol. (c) **3,** 956-959 (2006).

[85] P. Wagner and R. Helbig, *Hall-Effect and Anisotropy of Electron-Mobility in Zno*, Journal of Physics and Chemistry of Solids **35,** 327-335 (1974).

[86] T. Makino, Y. Segawa, A. Tsukazaki, A. Ohtomo, and M. Kawasaki, *Electron transport in ZnO thin films*, Applied Physics Letters **87** (2005).

[87] T. Ohgaki, N. Ohashi, H. Kakemoto, S. Wada, Y. Adachi, H. Haneda, and T. Tsurumi, *Growth condition dependence of morphology and electric properties of ZnO films on sapphire substrates prepared by molecular beam epitaxy*, JOURNAL OF APPLIED PHYSICS **93,** 1961-1965 (2003).

[88] A. Janotti and C. G. Van de Walle, *New insights into the role of native point defects in ZnO*, Journal of Crystal Growth **287,** 58-65 (2006).

[89] C. G. V. d. Walle, *Hydrogen as a Cause of Doping in Zinc Oxide*, Physical Review Letters **85,** 1012-1015 (2000).

[90] C. G. Van de Walle, *Hydrogen as a shallow center in semiconductors and oxides*, Physica Status Solidi B-Basic Research **235,** 89-95 (2003).

[91] S. F. J. Cox, E. A. Davis, S. P. Cottrell, P. J. C. King, J. S. Lord, J. M. Gil, H. V. Alberto, R. C. Vilão, J. P. Duarte, N. A. d. Campos, A. Weidinger, R. L. Lichti, and S. J. C. Irvine, *Experimental Confirmation of the Predicted Shallow Donor Hydrogen State in Zinc Oxide*, PHYSICAL REVIEW LETTERS **86,** 2601-2604 (2001).

[92] G. A. Shi, M. Saboktakin, M. Stavola, and S. J. Pearton, *"Hidden hydrogen" in as-grown ZnO*, Applied Physics Letters **85,** 5601-5603 (2004).

[93] C. A. Wolden, T. M. Barnes, J. B. Baxter, and E. S. Aydil, *Infrared detection of hydrogen-generated free carriers in polycrystalline ZnO thin films*, Journal of Applied Physics **97** (2005).

[94] A. Janotti and C. G. V. d. Walle, *Defect Physics in ZnO*, Mater. Res. Soc. Symp. Proc. **Fall MRS** (2006).

[95] K. Minegishi, Y. Koiwai, Y. Kikuchi, K. Yano, M. Kasuga, and A. Shimizu, *Growth of p-type zinc oxide films by chemical vapor deposition*, Japanese Journal of Applied Physics Part 2-Letters **36,** L1453-L1455 (1997).

[96] X. Li, S. E. Asher, B. M. Keyes, H. R. Moutinho, J. Luther, and T. J. Coutts, *p-TYPE ZnO THIN FILMS GROWN BY MOCVD*, 31st IEEE Photovoltaics Specialists Conference and Exhibition (2005).

[97] D. C. Look, G. M. Renlund, R. H. Burgener, and J. R. Sizelove, *As-doped p-type ZnO produced by an evaporation/sputtering process*, Applied Physics Letters **85,** 5269-5271 (2004).

[98] L. L. Yang, Z. Z. Ye, L. P. Zhu, Y. J. Zeng, Y. F. Lu, and B. H. Zhao, *Fabrication of p-type ZnO thin films via DC reactive magnetron sputtering by using Na as the dopant source*, Journal of Electronic Materials **36,** 498-501 (2007).

[99] C. Y. Zhang, X. M. Li, J. M. Bian, W. D. Yu, and X. D. Gao, *Structural and electrical properties of nitrogen and aluminum codoped p-type ZnO films*, Solid State Communications **132,** 75-78 (2004).

[100] M. Pan, J. Nause, V. Rengarajan, R. Rondon, E. H. Park, and I. T. Ferguson, *Epitaxial growth and characterization of p-type ZnO*, Journal of Electronic Materials **36,** 457-461 (2007).

[101] V. Srikant and D. R. Clarke, *On the optical band gap of zinc oxide*, JOURNAL OF APPLIED PHYSICS **83,** 5447-5451 (1998).

[102] B. E. Sernelius, K. F. Berggren, Z. C. Jin, I. Hamberg, and C. G. Granqvist, *Band-Gap Tailoring of Zno by Means of Heavy Al Doping*, Physical Review B **37,** 10244-10248 (1988).

[103] W. S. Shi, O. Agyeman, and C. N. Xu, *Enhancement of the light emissions from zinc oxide films by controlling the post-treatment ambient*, Journal of Applied Physics **91,** 5640-5644 (2002).

[104] M. Wu, A. Azuma, T. Shiosaki, and A. Kawabata, *Low-loss epitaxial ZnO optical waveguides on sapphire by rf magnetron sputtering*, Journal of Applied Physics **62,** 2482-2484 (1987).

[105] Z. C. Jin, I. Hamberg, and C. G. Granqvist, *Optical-Properties of Sputter-Deposited Zno-Al Thin-Films*, Journal of Applied Physics **64,** 5117-5131 (1988).

[106] I. Takeuchi, W. Yang, K.-S. Chang, M. A. Aronova, T. Venkatesan, R. D. Vispute, and L. A. Bendersky, *Monolithic multichannel ultraviolet detector arrays and continuous phase evolution in MgxZn1À xO composition spreads*, Journal of Applied Physics **94,** 7336-7340 (2003).

[107] K. Koike, K. Hama, I. Nakashima, G. Takada, K. Ogata, S. Sasa, M. Inoue, and M. Yano, *Molecular beam epitaxial growth of wide bandgap ZnMgO alloy films on (111)-oriented Si substrate toward UV-detector applications*, Journal of Crystal Growth **278,** 288-292 (2005).

[108] C. H. Choi and S. H. Kim, *Effects of post-annealing temperature on structural, optical, and electrical properties of ZnO and Znl-xMgxO films by reactive RF magnetron sputtering*, Journal of Crystal Growth **283,** 170-179 (2005).

[109] K. Koike, K. Hama, I. Nakashima, S. Sasa, M. Inoue, and M. Yano, *Molecular beam epitaxial growth of Al-doped ZnMgO alloy films for modulation-doped ZnO/ZnMgO heterostructures*, Japanese Journal of Applied Physics Part 1-Regular Papers Short Notes & Review Papers **44,** 3822-3827 (2005).

[110] Z. Q. Chen, G. J. Fang, C. Li, S. Sheng, and X. Z. Zhao, *Fabrication and properties of pulsed laser deposited wide band-gap Zn0.9Mg0.1O : Ga conducting films*, Journal of Inorganic Materials **21,** 707-712 (2006).

[111] M. X. Qiu, Z. Z. Ye, H. P. He, Y. Z. Zhang, X. Q. Gu, L. P. Zhu, and B. H. Zhao, *Effect of Mg content on structural, electrical, and optical properties of Li-doped Zn1-xMgxO thin films,* Applied Physics Letters **90** (2007).

[112] R. Dingle, H. L. Störmer, A. C. Gossard, and W. Wiegmann, *Electron mobilities in modulation-doped semiconductor heterojunction superlattices,* Applied Physics Letters **33,** 665-667 (1978).

[113] M. R. Melloch, *Molecular-Beam Epitaxy for High-Electron-Mobility Modulation-Doped 2-Dimensional Electron Gases,* Thin Solid Films **231,** 74-85 (1993).

[114] H. Kroemer, *Nobel Lecture: Quasielectric fields and band offsets: teaching electrons new tricks,* Reviews of Modern Physics **73,** 783-793 (2001).

[115] A. C. Gossard and A. Pinczuk, in *Synthetic Modulated Structures,* edited by L. L. Chang and B. C. Giessen (Academic Press, Inc., Orlando, 1985).

[116] A. Peczalski, G. H. Duh, A. Vanderziel, and X. C. Zhu, *Low-Frequency Noise in Algaas-Gaas Modfet and Its Implication for Device Performance,* Ieee Transactions on Electron Devices **30,** 1568-1568 (1983).

[117] H. L. Stormer, *Electron Mobilities in Modulation-Doped Gaas-(Alga)as Heterostructures,* Surface Science **132,** 519-526 (1983).

[118] T. J. Drummond, W. Kopp, M. Keever, H. Morkoc, and A. Y. Cho, *Electron-Mobility in Single and Multiple Period Modulation-Doped (Al,Ga)as/Gaas Heterostructures,* Journal of Applied Physics **53,** 1023-1028 (1982).

[119] H. L. Stormer, A. C. Gossard, W. Wiegmann, and K. Baldwin, *Dependence of electron mobility in modulaiton-doped GaAs-(Al,Ga)As heterojuction interfaces on electron density and Al concentration,* Applied Physics Letters **39,** 912-914 (1981).

[120] F. Y. Qu and P. C. Morais, *The 2-D-3-D crossover in modulation-doped GaAs-Ga1-xAlxAs quantum wells,* Ieee Journal of Quantum Electronics **33,** 1492-1497 (1997).

[121] V. T. Dolgopolov, E. V. Deviatov, A. A. Shashkin, U. Wieser, U. Kunze, G. Abstreiter, and K. Brunner, *Remote-doping scattering and the local field corrections in the 2D electron system in a modulation-doped Si/SiGe quantum well,* Superlattices and Microstructures **33,** 271-278 (2003).

[122] W. M. Chen, A. V. Buyanov, I. A. Buyanova, T. Lundstrom, W. G. Bi, Y. P. Zeng, and C. W. Tu, *Transport properties of intrinsically and extrinsically modulation doped InP/InGaAs heterostructures*, Physica Scripta **T79,** 103-105 (1999).

[123] R. Knobel, I. P. Smorchkova, and N. Samarth, *Fabrication and characterization of a two-dimensional electron gas in modulation doped ZnTe/Cd1-xMnxSe quantum wells*, Journal of Vacuum Science & Technology B **17,** 1147-1150 (1999).

[124] O. Aktas, Z. F. Fan, S. N. Mohammad, A. E. Botchkarev, and H. Morkoc, *High temperature characteristics of AlGaN/GaN modulation doped field-effect transistors*, Applied Physics Letters **69,** 3872-3874 (1996).

[125] K. Ellmer, *Resistivity of polycrystalline zinc oxide films: current status and physical limit*, Journal of Physics D: Applied Physics **34,** 3097-3108 (2001).

[126] H. Ryoken, Y. Adachi, I. Sakaguchi, N. Ohashi, H. Haneda, and T. Takenaka, in *Electroceramics in Japan VI*; *Vol. 248* (2003), p. 103-106.

[127] I. A. Rauf, *Low-Resistivity and High-Mobility Tin-Doped Indium Oxide-Films*, Materials Letters **18,** 123-127 (1993).

[128] W. R. L. Lambrecht, S. Limpijumnong, and B. Segall, *Theoretical studies of ZnO and related MgxZn1-xO alloy band structures*, Mrs Internet Journal of Nitride Semiconductor Research **4,** art. no.-G6.8 (1999).

[129] A. Ohtomo, M. Kawasaki, I. Ohkubo, H. Koinuma, T. Yasuda, and Y. Segawa, *Structure and optical properties of ZnO/Mg0.2Zn0.8O superlattices*, Applied Physics Letters **75,** 980-982 (1999).

[130] K. Ellmer and G. Vollweiler, *Electrical transport parameters of heavily-doped zinc oxide and zinc magnesium oxide single and multilayer films heteroepitaxially grown on oxide single crystals*, Thin Solid Films **496,** 104-111 (2006).

[131] J. J. Robbins and C. A. Wolden, *High mobility oxides: Engineered structures to overcome intrinsic performance limitations of transparent conducting oxides*, Applied Physics Letters **83,** 3933-3935 (2003).

[132] H. D. Sun, T. Makino, Y. Segawa, M. Kawasaki, A. Ohtomo, K. Tamura, and H. Koinuma, *Enhancement of exciton binding energies in ZnO/ZnMgO multiquantum wells*, J. Appl. Phys. **91,** 1993-1997 (2002).

[133] W. I. Park, G. Yi, M. Kim, and S. J. Pennycook, *Quantum confinement observed in ZnO/ZnMgO nanorod heterostructures*, Advanced materials **15,** 526-529 (2003).

[134] S. Heitsch, G. Benndorf, G. Zimmermann, C. Schulz, D. Spemann, H. Hochmuth, H. Schmidt, T. Nobis, M. Lorenz, and M. Grundmann, *Optical and structural properties of MgZnO/ZnO hetero- and double heterostructures grown by pulsed laser deposition*, Applied Physics a-Materials Science & Processing **88,** 99-104 (2007).

[135] M. Yano, K. Hashimoto, K. Fujimoto, K. Koike, S. Sasa, M. Inoue, Y. Uetsuji, T. Ohnishi, and K. Inaba, *Polarization-induced two-dimensional electron gas at Zn1-xMgxO/ZnO heterointerface*, Journal of Crystal Growth **301,** 353-357 (2007).

[136] H. Tampo, K. Matsubara, A. Yamada, H. Shibata, P. Fons, M. Yamagata, H. Kanie, and S. Niki, *High electron mobility Zn polar ZnMgO/ZnO heterostructures grown by molecular beam epitaxy*, Journal of Crystal Growth **301,** 358-361 (2007).

[137] G. Thomas, *Materials science - Invisible circuits*, Nature **389,** 907-908 (1997).

[138] Y. R. Ryu, W. J. Kim, and H. W. White, *Fabrication of homostructural ZnO p-n junctions*, Journal of Crystal Growth **219,** 419-422 (2000).

[139] S. Tuzemen, G. Xiong, J. Wilkinson, B. Mischuck, K. B. Ucer, and R. T. Williams, *Production and properties of p-n junctions in reactively sputtered ZnO*, Physica B-Condensed Matter **308,** 1197-1200 (2001).

[140] R. L. Hoffman, B. J. Norris, and J. F. Wager, *ZnO-based transparent thin-film transistors*, Applied Physics Letters **82,** 733-735 (2003).

[141] C. J. Kao, Y. W. Kwon, Y. W. Heo, D. P. Norton, S. J. Pearton, F. Ren, and G. C. Chi, *Comparison of ZnO metal-oxide-semiconductor field effect transistor and metal-semiconductor field effect transistor structures grown on sapphire by pulsed laser deposition*, Journal of Vacuum Science & Technology B **23,** 1024-1028 (2005).

[142] B. Y. Oh, M. C. Jeong, M. H. Ham, and J. M. Myoung, *Effects of the channel thickness on the structural and electrical characteristics of room-temperature fabricated ZnO thin-film transistors*, Semiconductor Science and Technology **22,** 608-612 (2007).

[143] S. Y. Ju, A. Facchetti, Y. Xuan, J. Liu, F. Ishikawa, P. D. Ye, C. W. Zhou, T. J. Marks, and D. B. Janes, *Fabrication of fully transparent nanowire transistors for transparent and flexible electronics*, Nature Nanotechnology **2,** 378-384 (2007).

Chapter 2

[1] P. B. Mirkarimi, M. Shinn, and S. A. Barnett, *AN ULTRAHIGH-VACUUM, MAGNETRON SPUTTERING SYSTEM FOR THE GROWTH AND ANALYSIS OF NITRIDE SUPERLATTICES*, Journal of Vacuum Science & Technology A-Vacuum Surfaces and Films 10, 75-87 (1992).

[2] K. H. Kim, K. C. Park, and D. Y. Ma, *Structural, electrical and optical properties of aluminum doped zinc oxide films prepared by radio frequency magnetron sputtering*, Journal of Applied Physics 81, 7764-7772 (1997).

[3] R. Swanepoel, *Determination of the thickness and optical constants of amorphous silicon*, Journal of Physics E: Scientific Insturments 16, 1214-1222 (1983).

[4] J. Als-Nielsen and D. McMorrow, *Elements of Modern X-ray Physics* (John Wiley and Sons, Ltd, New York, 2001).

[5] T. Kitatani, M. Kondow, T. Kikawa, Y. Yazawa, M. Okai, and K. Uomi, *Analysis of band offset in GaNAs/GaAs by X-ray photoelectron spectroscopy*, Japanese Journal of Applied Physics Part 1-Regular Papers Short Notes & Review Papers 38, 5003-5006 (1999).

[6] P. Boieriu, R. Sporken, and S. Sivananthan, *Valence band offset at the CdS/CdTe interface*, J. Vac. Sci. Technol. B 20, 1777-1780 (2002).

[7] S. A. Ding, S. R. Barman, K. Horn, H. Yang, B. Yang, O. Brandt, and K. Ploog, *Valence band discontinuity at a cubic GaN/GaAs heterojunction measured by synchrotron-radiation photoemission spectroscopy*, Applied Physics Letters 70, 2407-2409 (1997).

Chapter 3

[1] P. B. Mirkarimi, M. Shinn, and S. A. Barnett, *An Ultrahigh-Vacuum, Magnetron Sputtering System for the Growth and Analysis of Nitride Superlattices*, Journal of Vacuum Science & Technology A 10, 75-81 (1992).

[2] K. C. Ruthe and S. A. Barnett, *Glancing-angle ion-assisted deposition of ZnO thin films*, Surface Science 538, L460-L464 (2003).

[3] J. Hinze and K. Ellmer, *In situmeasurement of mechanical stress in polycrystalline zinc-oxide thin films prepared by magnetron sputtering*, Journal of Applied Physics 88, 2443-2450 (2000).

[4] I. C. Noyan and J. B. Cohen, *Residual stress: measurement by diffraction and interpretation* (Springer-Verlag, New York, NY, 1987).

[5] F. Boulc'h, M. Schouler, P. Donnadieu, J. Chaix, and E. Djurado, *DOMAIN SIZE DISTRIBUTION OF Y-TZP NANO-PARTICLES USING XRD AND HRTEM*, Image Anal. Stereol. 20, 157-161 (2001).

[6] H. Kang, K. Nakamura, S. Lim, and D. Shindo, *Epitaxial growth of ZnO films on (0001) sapphire at low temperatures by electron cyclotron resonance-assisted molecular beam epitaxy and their microstructural characterizations*, Japanese Journal of Applied Physics 37, 781-785 (1998).

[7] J. A. Thornton, *High Rate Thick Film Growth*, Annual Review of Materials Science 7, 239 (1977).

[8] M. Ohring, *The Material Science of Thin Films* (Academic Press, San Diego, 1992).

[9] K. C. Ruthe, D. J. Cohen, and S. A. Barnett, *Low temperature epitaxy of reactively sputtered ZnO on sapphire*, Journal of Vacuum Science & Technology A 22, 2446-2452 (2004).

[10] B. E. Sernelius, K. F. Berggren, Z. C. Jin, I. Hamberg, and C. G. Granqvist, *Band-Gap Tailoring of Zno by Means of Heavy Al Doping*, Physical Review B 37, 10244-10248 (1988).

[11] M. D. McCluskey, S. J. Jokela, K. K. Zhuravlev, P. J. Simpson, and K. G. Lynn, *Infrared spectroscopy of hydrogen in ZnO*, APPLIED PHYSICS LETTERS 81, 3807-3809 (2002).

[12] W. S. Shi, O. Agyeman, and C. N. Xu, *Enhancement of the light emissions from zinc oxide films by controlling the post-treatment ambient*, Journal of Applied Physics 91, 5640-5644 (2002).

[13] C. G. V. d. Walle, *Hydrogen as a Cause of Doping in Zinc Oxide*, Physical Review Letters 85, 1012-1015 (2000).

[14] E. Burstein, *Anomalous optical absorption limit in InSb*, Physical Review 93, 632-633 (1954).

[15] L. Solymar and D. Walsh, *Electrical Properties of Materials*, sixth ed. (Oxford University Press, Oxford, 1998).

[16] T. J. Coutts, D. L. Young, and X. Li, *Characterization of transparent conducting oxides*, MRS Bulletin 25, 58-65 (2000).

[17] V. A. Coleman and C. Jagadish, *Zinc Oxide Bulk, Thin Films and Nanostructures* (Elsevier, Amsterdam, 2006).

[18] B. E. Sernelius, *Self-Energy Shifts in Heavily Doped, Polar Semiconductors*, Physical Review B 36, 4878-4887 (1987).

[19] I. Hamberg, C. G. Granqvist, K. F. Berggren, B. E. Sernelius, and L. Engstrom, *Band-Gap Widening in Heavily Sn-Doped In2o3*, Physical Review B 30, 3240-3249 (1984).

[20] H. Ryoken, I. Sakaguchi, N. Ohashi, T. Sekiguchi, S. Hishita, and H. Haneda, *Non-equilibrium defects in aluminum-doped zinc oxide thin films grown with a pulsed laser deposition method*, Journal of Materials Research 20, 2866-2872 (2005).

Chapter 4

[1] M. K. Puchert, P. Y. Timbrell, and R. N. Lamb, *Postdeposition annealing of radio frequency magnetron sputtered ZnO films*, Journal of Vacuum Science and Technology A **14,** 2220-2230 (1996).

[2] K. C. Ruthe and S. A. Barnett, *Glancing-angle ion-assisted deposition of ZnO thin films*, Surface Science **538,** L460-L464 (2003).

[3] H. Ryoken, I. Sakaguchi, N. Ohashi, T. Sekiguchi, S. Hishita, and H. Haneda, *Non-equilibrium defects in aluminum-doped zinc oxide thin films grown with a pulsed laser deposition method*, Journal of Materials Research **20,** 2866-2872 (2005).

[4] Y. Ma, G. T. Du, T. P. Yang, D. L. Qiu, X. Zhang, H. J. Yang, Y. T. Zhang, B. J. Zhao, X. T. Yang, and D. L. Liu, *Effect of the oxygen partial pressure on the properties of ZnO thin films grown by metalorganic vapor phase epitaxy*, Journal of Crystal Growth **255,** 303-307 (2003).

[5] C. G. Van de Walle, *Hydrogen as a shallow center in semiconductors and oxides*, Physica Status Solidi B-Basic Research **235,** 89-95 (2003).

[6] C. A. Wolden, T. M. Barnes, J. B. Baxter, and E. S. Aydil, *Infrared detection of hydrogen-generated free carriers in polycrystalline ZnO thin films*, Journal of Applied Physics **97** (2005).

[7] T. Minami, *New n-type transparent conducting oxides*, MRS Bulletin **25,** 38-44 (2000).

[8] P. Nunes, E. Fortunato, and R. Martins, *Influence of the post-treatment on the properties of ZnO thin films*, Thin Solid Films **383,** 277-280 (2001).

[9] C. G. V. d. Walle, *Hydrogen as a Cause of Doping in Zinc Oxide*, Physical Review Letters **85,** 1012-1015 (2000).

Chapter 5

[1] D. S. Ginley and C. Bright, *Transparent Conducting Oxides*, MRS Bull. **25,** 15-18 (2000).

[2] S. H. Jeong, J. W. Lee, S. B. Lee, and J. H. Boo, *Deposition of aluminum-doped zincoxide films by RF magnetron sputtering and study of their structural, electrical and optical properties*, Thin Solid Films **435,** 78-82 (2003).

[3] E. Burstein, *Anomalous optical absorption limit in InSb*, Physical Review **93,** 632-633 (1954).

[4] B. Rech and H. Wagner, *Potential of amorphous silicon for solar cells*, Applied Physics A: Materials Science & Processing **69,** 155-167 (1999).

[5] T. Minemoto, T. Negami, S.Nishiwaki, H. Takakura, and Y. Hamakawa, *Preparation of $Zn_{1-x}Mg_xO$ films by radio frequency magnetron sputtering*, Thin Solid Films **372,** 173-176 (2000).

[6] K. Ellmer, *Resistivity of polycrystalline zinc oxide films: current status and physical limit*, Journal of Physics D: Applied Physics **34,** 3097-3108 (2001).

[7] J. J. Robbins and C. A. Wolden, *High mobility oxides: Engineered structures to overcome intrinsic performance limitations of transparent conducting oxides*, Applied Physics Letters **83,** 3933-3935 (2003).

[8] A. Ohtomo, M. Kawasaki, T. Koida, K. Masubuchi, H. Koinuma, Y. Sakurai, Y. Yoshida, T. Yasuda, and Y. Segawa, *$Mg_xZn_{1-x}O$ as a II-VI widegap semiconductor alloy*, Applied Physics Letters **72,** 2466-2468 (1998).

[9] H. Ryoken, Y. Adachi, I. Sakaguchi, N. Ohashi, H. Haneda, and T. Takenaka, *Basic examination for nodulation-doped (Zn,Mg,Al)O/ZnO*, Key Engineering Materials Electrocermaics In Japan VI **248,** 103-106 (2003).

[10] P. B. Mirkarimi, M. Shinn, and S. A. Barnett, *AN ULTRAHIGH-VACUUM, MAGNETRON SPUTTERING SYSTEM FOR THE GROWTH AND ANALYSIS OF NITRIDE SUPERLATTICES*, Journal of Vacuum Science & Technology A-Vacuum Surfaces and Films **10,** 75-87 (1992).

[11] R. Swanepoel, *Determination of the thickness and optical constants of amorphous silicon*, Journal of Physics E: Scientific Insturments **16,** 1214-1222 (1983).

[12] L. J. v. d. Pauw, *A method of measuring specific resistivity and hall effect of discs of arbitrary shape*, Philips Research Reports **13,** 1-9 (1958).

[13] K. Ellmer, *Magnetron sputtering of transparent conductive zinc oxide: relation between the sputtering parameters and the electronic properties*, Journal of Physics D: Applied Physics **33,** R17-R32 (2000).

[14] H. Kang, K. Nakamura, S. Lim, and D. Shindo, *Epitaxial growth of ZnO films on (0001) sapphire at low temperatures by electron cyclotron resonance-assisted molecular beam epitaxy and their microstructural characterizations*, Japanese Journal of Applied Physics **37,** 781-785 (1998).

[15] J. Narayan and B. C. Larson, *Domain epitaxy: A unified paradigm for thin film growth*, Journal of Applied Physics **93,** 278-285 (2003).

[16] K. C. Ruthe and S. A. Barnett, *Glancing-angle ion-assisted deposition of ZnO thin films*, Surface Science **538,** L460-L464 (2003).

[17] M. K. Puchert, P. Y. Timbrell, and R. N. Lamb, *Postdeposition annealing of radio frequency magnetron sputtered ZnO films*, Journal of Vacuum Science and Technology A **14,** 2220-2230 (1996).

[18] E. Bauer, *Single-Crystal Films* (The MacMillan Company, New York, 1964).

[19] H. Kim, J. S. Horwitz, S. B. Qadri, and D. B. Chrisey, *Epitaxial growth of Al-doped ZnO thin films grown by pulsed laser deposition*, Thin Solid Films **420-421,** 107-111 (2002).

[20] R. Ondo-Ndong, F. Pascal-Delannoy, A. Boyer, A. Giani, and A. Foucaran, *Structural properties of zinc oxide thin films prepared by r.f. magnetron sputtering*, Materials Science and Engineering B **97,** 68-73 (2003).

[21] M. Chen, Z. L. Pei, X. Wang, C. Sun, and L. S. Wen, *Structural, electrical, and optical properties of transparent conductive oxide ZnO:Al films prepared by dc magnetron reactive sputtering*, Journal of Vacuum Science and Technology A **19,** 963-970 (2001).

[22] F. Boulc'h, M. Schouler, P. Donnadieu, J. Chaix, and E. Djurado, *DOMAIN SIZE DISTRIBUTION OF Y-TZP NANO-PARTICLES USING XRD AND HRTEM*, Image Anal. Stereol. **20,** 157-161 (2001).

[23] P. Nunes, E. Fortunato, P. Tonello, F. B. Fernandes, P. Vilarinho, and R. Martins, *Effect of different dopant elements on the properties of ZnO thin films*, Vacuum **64,** 281-285 (2002).

[24] P. Nunes, E. Fortunato, and R. Martins, *Influence of the post-treatment on the properties of ZnO thin films*, Thin Solid Films **383,** 277-280 (2001).

[25] C. G. V. d. Walle, *Hydrogen as a Cause of Doping in Zinc Oxide*, Physical Review Letters **85,** 1012-1015 (2000).

[26] T. J. Coutts, D. L. Young, and X. Li, *Characterization of transparent conducting oxides*, MRS Bulletin **25,** 58-65 (2000).

[27] V. Gupta and A. Mansingh, *Influence of postdeposition annealing on the structural and optical properties of sputtered zinc oxide film*, Journal of Applied Physics **80,** 1063-1073 (1996).

[28] T. Minami, *New n-type transparent conducting oxides*, MRS Bulletin **25,** 38-44 (2000).

[29] M. Ohring, *The Material Science of Thin Films* (Academic Press, San Diego, 1992).

[30] K. H. Kim, K. C. Park, and D. Y. Ma, *Structural, electrical and optical properties of aluminum doped zinc oxide films prepared by radio frequency magnetron sputtering*, Journal of Applied Physics **81,** 7764-7772 (1997).

[31] W. Hirschwald, P. Bonasewicz, L. Ernst, M. Grade, D. Hofmann, S. Krebs, R. Littbarski, and G. Neumann, *Zinc Oxide: Properties and Behavior of the Bulk, the Solid/Vacuum and Solid/Gas Interface*, Current Topics in Materials Science **7,** 148-482 (1981).

[32] E. V. Lavrov, J. Weber, F. Borrnert, C. G. V. d. Walle, and R. Helbig, *Hydrogen-related defects in ZnO studied by infrared absorption spectroscopy*, Physical Review B **66,** 165205 (2002).

[33] C. G. Van de Walle, *Universal alignment of hydrogen levels in semiconductors and insulators*, Physica B: Condensed Matter
Proceedings of the 23rd International Conference on Defects in Semiconductors **376-377,** 1-6 (2006).

[34] J. Charles F. Windisch, G. J. Exarhos, C. Yao, and L.-Q. Wang, *Raman study of the influence of hydrogen on defects in ZnO*, Journal of Applied Physics **101,** 123711 (2007).

[35] H. L. Hartnagel, A. L. Dawar, A. K. Jain, and C. Jagadish, *Semiconducting Transparent Thin Films* (London, 1995).

[36] J. G. Lu, S. Fujita, T. Kawaharamura, H. Nishinaka, Y. Kamada, and T. Ohshima, *Carrier concentration induced band-gap shift in Al-doped Zn_{1-x}Mg_xO thin films.*, Applied Physics Letters **89,** N.PAG (2006).

[37] Y. Chiang, D. P. Birnie, and W. D. Kingery, *Physical Ceramics: Principles of ceramic science and engineering* (John Wiley & Sons, Inc., New York, 1997).

[38] E. Shanthi, A. Banerjee, V. Dutta, and K. L. Chopra, *Electrical and optical properties of tin oxide films doped with F and (Sb+F)*, Journal of Applied Physics **53,** 1615 (1982).

[39] R. Y. Korotkov, J. M. Gregie, and B. W. Wessels, *Codoping of wide gap epitaxial III-nitride semiconductors*, OPTO-ELECTRONICS REVIEW **10,** 243 (2002).

[40] L. Makowski and M. Glickman, *Disorder Scattering in Solid Solutions of III-V Semiconducting Compounds*, Journal of Physics and Chemistry of Solids **34,** 487-492 (1973).

[41] I. Takeuchi, W. Yang, K.-S. Chang, M. A. Aronova, T. Venkatesan, R. D. Vispute, and L. A. Bendersky, *Monolithic multichannel ultraviolet detector arrays and continuous phase evolution in MgxZn1À xO composition spreads*, Journal of Applied Physics **94,** 7336-7340 (2003).

[42] R. G. Gordon, *Criteria for Choosing Transparent Conductors*, MRS Bulletin **25,** 52-57 (2000).

[43] X.-L. Xu, L. Lu, Y. Wang, and C.-S. Shi, *Photoluminescence and structure properties of $Zn_{1-x}Mg_xO$ films grown by RF magnetron sputtering*, Journal of Physics: Condensed Matter **4,** 1189 (2006).

[44] X. Gu, L. Zhu, Z. Ye, Q. Ma, H. He, Y. Zhang, and B. Zhao, *Highly transparent and conductive Zn0.85Mg0.15O:Al thin films prepared by pulsed laser deposition*, Solar Energy Materials and Solar Cells **92,** 343-347 (2008).

Chapter 6

[1] T. Minami, T. Miyata, and T. Yamamoto, *Work function of transparent conducting multicomponent oxide thin films prepared by magnetron sputtering*, Surface & Coatings Technology **109,** 583-587 (1998).

[2] B. Rech, O. Kluth, T. Repmann, T. Roschek, J. Springer, J. Muller, F. Finger, H. Stiebig, and H. Wagner, *New materials and deposition techniques for highly efficient silicon thin film solar cells*, Solar Energy Materials and Solar Cells **74,** 439-447 (2002).

[3] K. Nomura, H. Ohta, K. Ueda, T. Kamiya, M. Hirano, and H. Hosono, *Thin-film transistor fabricated in single-crystalline transparent oxide semiconductor*, Science **300,** 1269-1272 (2003).

[4] J. F. Wager, *Transparent electronics*, Science **300,** 1245-1246 (2003).

[5] S. Kim, B. S. Kang, F. Ren, Y. W. Heo, K. Ip, D. P. Norton, and S. J. Pearton, *Characteristics of thin-film p-ZnMgO/n-ITO heterojunctions on glass substrates*, Electrochemical and Solid State Letters **7,** G145-G147 (2004).

[6] T. Minami, *New n-type transparent conducting oxides*, MRS Bulletin **25,** 38-44 (2000).

[7] T. J. Coutts, D. L. Young, and X. Li, *Characterization of transparent conducting oxides*, MRS Bulletin **25,** 58-65 (2000).

[8] A. J. Freeman, K. R. Poeppelmeier, T.O. Mason, R. P. H. Chang, and T. J. Marks, *Chemical and Thin-Film Strategies for New Transparent Conducting Oxides*, MRS Bulletin **25,** 45-51 (2000).

[9] T. J. Coutts, D. L. Young, X. Li, W. P. Mulligan, and X. Wu, *Search for improved transparent conducting oxides: A fundamental investigation of CdO, Cd2SnO4, and Zn2SnO4*, J. Vac. Sci. Technol. A **18,** 2646-2660 (2000).

[10] M. Yan, M. Lane, C. R. Kannewurf, and R. P. H. Chang, *Highly conductive epitaxial CdO thin films prepared by pulsed laser deposition*, Appl. Phys. Lett. **78,** 2342-2344 (2001).

[11] B. J. Norris, J. Anderson, J. F. Wager, and D. A. Keszler, *Spin-coated zinc oxide transparent transistors*, J. Phys. D **36,** L105-L107 (2003).

[12] I. A. Rauf, *Low-Resistivity and High-Mobility Tin-Doped Indium Oxide-Films*, Materials Letters **18,** 123-127 (1993).

[13] K. Ellmer, *Magnetron sputtering of transparent conductive zinc oxide: relation between the sputtering parameters and the electronic properties*, J. Phys. D **33,** R17-R32 (2000).

[14] R. Dingle, H. L. Stormer, A. C. Gossard, and W. Wiegmann, *Electron Mobilities in Modulation-Doped Semiconductor Heterojunction Super-Lattices*, Appl. Phys. Lett. **33,** 665-667 (1978).

[15] T. J. Drummond, H. Morkoc, K. Hess, and A. Y. Cho, *Experimental and Theoretical Electron-Mobility of Modulation Doped Alxga1-Xas-Gaas Heterostructures Grown by Molecular-Beam Epitaxy*, J. Appl. Phys. **52,** 5231-5234 (1981).

[16] S. Gokden, *Mobility of two-dimensional electrons in an AlGaN/GaN modulation-doped heterostructure*, Phys. Status Solidi A **200,** 369-377 (2003).

[17] C. H. Mueller, E. T. Croke, and S. A. Alterovitz, *High electron mobility in SiGe/Si n-MODFET structures on sapphire substrates*, Electron. Lett. **39,** 1353-1354 (2003).

[18] J. J. Robbins and C. A. Wolden, *High mobility oxides: Engineered structures to overcome intrinsic performance limitations of transparent conducting oxides*, Appl. Phys. Lett. **83,** 3933-3935 (2003).

[19] D. J. Cohen, K. C. Ruthe, and S. A. Barnett, *Transparent conducting Zn1-xMgxO :(Al,In) thin films*, J. Appl. Phys. **96,** 459-467 (2004).

[20] G. L. Snider, *Free Ware program available at http://www.nd.edu/~gsnider/*, Free Ware program available at http://www.nd.edu/~gsnider/.

[21] I. H. Tan, G. L. Snider, L. D. Chang, and E. L. Hu, *A Self-Consistent Solution of Schrodinger-Poisson Equations Using a Nonuniform Mesh*, J. Appl. Phys. **68,** 4071-4076 (1990).

[22] A. Ohtomo, M. Kawasaki, T. Koida, K. Masubuchi, H. Koinuma, Y. Sakurai, Y. Yoshida, T. Yasuda, and Y. Segawa, *MgxZn1-xO as a II-VI widegap semiconductor alloy*, Appl. Phys. Lett. **72,** 2466-2468 (1998).

[23] H. Ryoken, Y. Adachi, I. Sakaguchi, N. Ohashi, H. Haneda, and T. Takenaka, in *Electroceramics in Japan VI*; *Vol. 248* (2003), p. 103-106.

[24] W. R. L. Lambrecht, S. Limpijumnong, and B. Segall, *Theoretical studies of ZnO and related MgxZn1-xO alloy band structures*, Mrs Internet Journal of Nitride Semiconductor Research **4,** art. no.-G6.8 (1999).

[25] P. Boieriu, R. Sporken, and S. Sivananthan, *Valence band offset at the CdS/CdTe interface*, J. Vac. Sci. Technol. B **20,** 1777-1780 (2002).

[26] K. Ellmer, *Resistivity of polycrystalline zinc oxide films: current status and physical limit*, J. Phys. D **34,** 3097-3108 (2001).

[27] K. Matsubara, H. Tampo, H. Shibata, A. Yamada, P. Fons, K. Iwata, and S. Niki, *Band-gap modified Al-doped Zn1-xMgxO transparent conducting films deposited by pulsed laser deposition*, Applied Physics Letters **85,** 1374-1376 (2004).

[28] S. D. Lazarev, E. Z. Meilikhov, and B. A. Aronzon, in *Handbook of Physical Quantities*, edited by I. S. Grigoriev, E. Z. Meilikhov, and A. A. Radzig (CRC Press, Inc., New York, 1997).

[29] T. J. Drummond, H. Morkoc, and A. Y. Cho, *Dependence of Electron-Mobility on Spatial Separation of Electrons and Donors in Alxga1-Xas-Gaas Heterostructures*, J. Appl. Phys. **52,** 1380-1386 (1981).

[30] P. J. Price, *Electron-Transport in Polar Heterolayers*, Surf. Sci. **113,** 199-210 (1982).

[31] A. C. Gossard and A. Pinczuk, in *Synthetic Modulated Structures*, edited by L. L. Chang and B. C. Giessen (Academic Press, Inc., Orlando, 1985).

[32] V. V. Mitin, V. A. Kochelap, and M. A. Stroscio, *Quantum Heterostructures: Microelectronics and Optoelectronics*, first ed. (Cambridge University Press, Cambridge, 1999).

[33] P. T. Coleridge, *Intersubband Scattering in a 2d Electron-Gas*, Semiconductor Science and Technology **5,** 961-966 (1990).

[34] D. G. Schlom, J. H. Haeni, J. Lettieri, C. D. Theis, W. Tian, J. C. Jiang, and X. Q. Pan, *Oxide nano-engineering using MBE*, Materials Science and Engineering B-Solid State Materials for Advanced Technology **87,** 282-291 (2001).

[35] H. D. Sun, T. Makino, Y. Segawa, M. Kawasaki, A. Ohtomo, K. Tamura, and H. Koinuma, *Enhancement of exciton binding energies in ZnO/ZnMgO multiquantum wells*, J. Appl. Phys. **91,** 1993-1997 (2002).

[36] T. Gruber, C. Kirchner, R. Kling, F. Reuss, and A. Waag, *ZnMgO epilayers and ZnO-ZnMgO quantum wells for optoelectronic applications in the blue and UV spectral region*, Appl. Phys. Lett. **84,** 5359-5361 (2004).

[37] L. J. Meng and M. P. Dossantos, *Characterization of Zno Films Prepared by De Reactive Magnetron Sputtering at Different Oxygen Partial Pressures*, Vacuum **46,** 1001-1004 (1995).

[38] K. Koike, K. Hama, I. Nakashima, S. Sasa, M. Inoue, and M. Yano, *Molecular beam epitaxial growth of Al-doped ZnMgO alloy films for modulation-doped ZnO/ZnMgO heterostructures*, Japanese Journal of Applied Physics Part 1-Regular Papers Short Notes & Review Papers **44,** 3822-3827 (2005).

[39] M. Yano, K. Hashimoto, K. Fujimoto, K. Koike, S. Sasa, M. Inoue, Y. Uetsuji, T. Ohnishi, and K. Inaba, *Polarization-induced two-dimensional electron gas at Zn1-xMgxO/ZnO heterointerface*, Journal of Crystal Growth **301,** 353-357 (2007).

[40] H. Tampo, K. Matsubara, A. Yamada, H. Shibata, P. Fons, M. Yamagata, H. Kanie, and S. Niki, *High electron mobility Zn polar ZnMgO/ZnO heterostructures grown by molecular beam epitaxy*, Journal of Crystal Growth **301,** 358-361 (2007).

[41] H. Tampo, H. Shibata, K. Matsubara, A. Yamada, P. Fons, S. Niki, M. Yamagata, and H. Kanie, *Two-dimensional electron gas in Zn polar ZnMgO/ZnO heterostructures grown by radical source molecular beam epitaxy.*, Applied Physics Letters **89,** N.PAG (2006).

Chapter 7

[1] T. J. Coutts, D. L. Young, and X. Li, *Characterization of transparent conducting oxides*, MRS Bulletin **25,** 58-65 (2000).

[2] L. J. Meng and M. P. Dossantos, *Characterization of Zno Films Prepared by De Reactive Magnetron Sputtering at Different Oxygen Partial Pressures*, Vacuum **46,** 1001-1004 (1995).

[3] K. T. Roro, G. H. Kassier, J. K. Dangbegnon, S. Sivaraya, J. E. Westraadt, J. H. Neethling, A. W. R. Leitch, and J. R. Botha, *Temperature-dependent Hall effect studies of ZnO thin films grown by metalorganic chemical vapour deposition*, Semiconductor Science and Technology **23,** 055021 (2008).

[4] L. Sagalowicz and G. R. Fox, *Planar defects in ZnO thin films deposited on optical fibers and flat substrates*, Journal of Materials Research **14,** 1876-1885 (1999).

[5] V. A. Coleman, M. Buda, H. H. Tan, C. Jagadish, M. R. Phillips, K. Koike, S. Sasa, M. Inoue, and M. Yano, *Observation of blue shifts in ZnO/ZnMgO multiple quantum well structures by ion-implantation induced intermixing*, Semiconductor Science and Technology **21,** L25-L28 (2006).

[6] J. Crank, *The Mathematics of Diffusion* (Oxford University Press, London, 1956).

[7] S. Hofmann and J. M. Sanz, in *Thin Film and Depth Profile Analysis*; *Vol. 37*, edited by H. Oechsner (Springer-Verlag, Berlin, 1984), p. 205.

[8] J. Als-Nielsen and D. McMorrow, *Elements of Modern X-ray Physics* (John Wiley and Sons, Ltd, New York, 2001).

[9] C. Engstrom, J. Birch, L. Hultman, C. Lavoie, C. Cabral, J. L. Jordan-Sweet, and J. R. A. Carlsson, *Interdiffusion studies of single crystal TiN/NbN superlattice thin films*, Journal of Vacuum Science & Technology A: Vacuum, Surfaces, and Films **17,** 2920-2927 (1999).

[10] A. L. Greer and F. Spaepen, in *Synthetic Modulated Structures* (Academic Press, New York, 1985).

[11] A. Ohtomo, R. Shiroki, I. Ohkubo, H. Koinuma, and M. Kawasaki, *Thermal stability of supersaturated MgxZn12 xO alloy films and MgxZn12 xO/ZnO heterointerfaces*, Applied Physics Letters **75,** 4088-4090 (1999).

[12] K. Koike, G.-y. Takada, K. Fujimoto, S. Sasa, M. Inoue, and M. Yano, *Characterization of [ZnO]m[ZnMgO]n multiple quantum wells grown by molecular beam epitaxy*, Physica E: Low-dimensional Systems and Nanostructures Proceedings of the 12th International Conference on Modulated Semiconductor Structures **32,** 191-194 (2006).